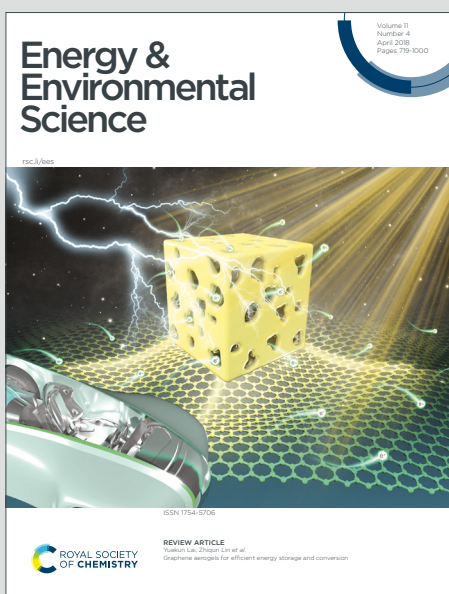


Energy & Environmental Science

Accepted Manuscript

This article can be cited before page numbers have been issued, to do this please use: S. Xie, W. Ma, X. Wu, H. Zhang, Q. Zhang, Y. Wang and Y. Wang, *Energy Environ. Sci.*, 2020, DOI: 10.1039/D0EE01860K.



This is an Accepted Manuscript, which has been through the Royal Society of Chemistry peer review process and has been accepted for publication.

Accepted Manuscripts are published online shortly after acceptance, before technical editing, formatting and proof reading. Using this free service, authors can make their results available to the community, in citable form, before we publish the edited article. We will replace this Accepted Manuscript with the edited and formatted Advance Article as soon as it is available.

You can find more information about Accepted Manuscripts in the [Information for Authors](#).

Please note that technical editing may introduce minor changes to the text and/or graphics, which may alter content. The journal's standard [Terms & Conditions](#) and the [Ethical guidelines](#) still apply. In no event shall the Royal Society of Chemistry be held responsible for any errors or omissions in this Accepted Manuscript or any consequences arising from the use of any information it contains.

Energy & Environmental Science**REVIEW****Photocatalytic and electrocatalytic transformations of C1 molecules involving C–C coupling**

Received 00th January 20xx,
Accepted 00th January 20xx

DOI: 10.1039/x0xx00000x

Selective transformation of one-carbon (C1) molecules, which are abundant or easily available and inexpensive carbon feedstocks, into value-added multi-carbon (C_{2+}) compounds is a very attractive but highly challenging research target. Photocatalysis and electrocatalysis have offered great opportunities for the activation and controllable C–C coupling of C1 molecules under mild and environmental-benign conditions. This article provides a critical review on recent advances in photocatalytic and electrocatalytic conversions of major C1 molecules, including CO, CO_2 , CH_4 , CH_3OH and HCHO, into C_{2+} compounds, such as C_2H_4 , C_3H_6 , ethanol and ethylene glycol, which plays essential roles in the current chemical or energy industry. Besides the photocatalysts and electrocatalysts reported for these conversions, the structure-performance relationships and the key factors that control the activity and product selectivity are analysed to provide insights for the rational design of more efficient catalysts for the synthesis of C_{2+} compounds from C1 feedstocks. The active species, reaction intermediates and reaction or catalyst-functioning mechanism are discussed to deepen the understanding of the chemistry for the activation and selective C–C coupling of C1 molecules in the presence of solar energy or electrical energy.

Broader context

Under the current background of looking for alternative carbon resources to replace crude oil for the production of chemicals and liquid fuels, the transformation of C1 molecules, which are typically either abundant in nature or can be readily produced from non-petroleum carbon resources, into important C_{2+} compounds such as ethylene, propylene, ethanol and ethylene glycol, has attracted much recent attention. The activation of stable C1 molecules (e.g., CH_4 and CO_2) and the controllable C–C coupling are two of the most challenging research goals in chemistry. As compared to thermocatalysis, which is usually performed at harsh conditions and has difficulty in controlling product selectivity, photocatalysis and electrocatalysis hold great potential to activate and selectively convert C1 molecules to C_{2+} compounds under mild conditions with solar or electrical energy. This article highlights the state-of-the-art advances in photocatalytic/electrocatalytic transformations of C1 molecules into important C_{2+} compounds. The challenges and opportunities in this field will be analysed. The present article can stimulate further research effort to develop efficient photocatalytic/electrocatalytic systems for C1 chemistry and to deepen the understanding of mechanisms for activation and selective C–C coupling of C1 molecules in the presence of solar or electrical energy.

1. Introduction

C1 chemistry, i.e., the chemistry for the transformation of C1 molecules into value-added products, is experiencing a renaissance because of the rapidly growing demand for the harvest of carbon-based energy and chemicals from alternative resources other than petroleum, such as the emerging shale gas in the US, coal in China, renewable biomass and CO_2 .^{1–4} Traditional homogeneous and heterogeneous catalysis has played crucial roles in C1 chemistry by transforming C1 molecules such as CO, CO_2 , CH_4 and CH_3OH into liquid fuels (e.g.,

gasoline, diesel and jet fuel) or building-block chemicals (e.g., C_2H_4 , C_3H_6 , aromatics and ethanol).^{5–26} Several C1-chemistry-based commercial processes such as the carbonylation of methanol to acetic acid,⁴ the conversion of natural gas to liquid fuels (GTL) or the conversion of coal to liquid fuels (CTL) via synthesis gas (CO/H_2) by Fischer-Tropsch synthesis,⁷ and the conversion of methanol to gasoline (MTG) or the conversion of methanol to lower olefins (MTO)^{23–26} have contributed largely to the chemical and energy industries. Most of these reactions are performed under harsh conditions such as high temperatures and/or high pressures, and the selectivity of products, in particular a specific C_{2+} compound, is difficult to control. Some developments based on the design of homogeneous and heterogeneous catalysts have been achieved for selective conversions of C1 molecules into C_{2+} compounds. For example, the design of bi(multi)functional catalysts or catalytic systems that work in tandem have shown a great potential to synthesize of C_2 – C_4 olefins, aromatics and C_{2+} oxygenates by hydrogenation of CO and CO_2 .^{8,13–15,27–38}

^a State Key Laboratory of Physical Chemistry of Solid Surfaces, Collaborative Innovation Center of Chemistry for Energy Materials, National Engineering Laboratory for Green Chemical Productions of Alcohols, Ethers and Esters, College of Chemistry and Chemical Engineering, Xiamen University, Xiamen 361005, China.
E-mail: zhangqh@xmu.edu.cn, wangye@xmu.edu.cn

^b State Key Laboratory of Green Chemical Engineering and Industrial Catalysis, Shanghai Research Institute of Petrochemical Technology, SINOPEC Corp., Shanghai 201208, China.
E-mail: wangyd.sshy@sinopec.com

REVIEW

Energy & Environmental Science

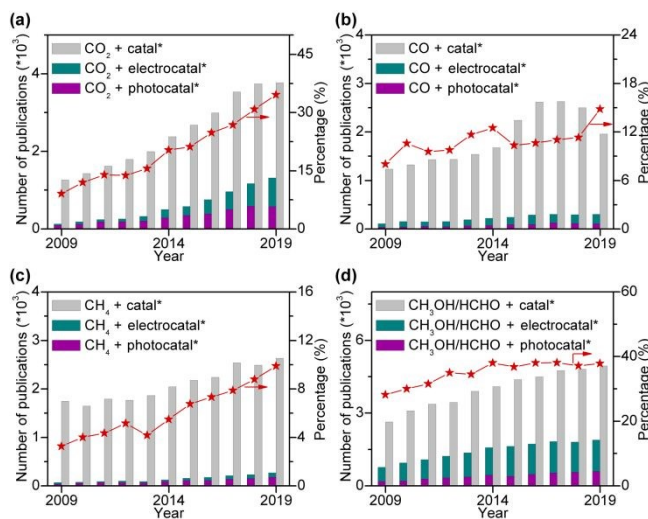


Fig. 1 Numbers of annual publications and percentages of electrocatalysis and photocatalysis for different C1 molecules based on Web of Science with keywords of C1 molecules plus “catal*”, “electrocatal*” and “photocatal*”. (a) CO₂. (b) CO. (c) CH₄. (d) CH₃OH and HCHO.

Nevertheless, the activation of stable C1 molecules (e.g., CO₂ and CH₄) under mild conditions and the precise C–C coupling of C1 molecules remain two of the most challenging research targets in chemistry.

Photocatalysis and electrocatalysis have been emerging as promising tools for the activation and selective conversion of C1 molecule into various types of products under mild conditions.^{39–42} The transformation of C1 molecules by photocatalysis/electrocatalysis has become a booming research field, and the number of academic publications in the field has increased enormously over the past decade (Fig. 1). At the same time, many review articles have been published on either photocatalytic or electrocatalytic conversions of a single C1 molecule, in particular CO₂.^{43–56} However, to the best of our knowledge, so far few critical reviews have been contributed to photocatalytic/electrocatalytic conversions of multiple C1 molecules with a focus on C–C coupling.

The present article is devoted to reviewing recent advances in the photocatalytic/electrocatalytic conversions of typical C1 molecules including CO₂, CO, CH₄, CH₃OH and HCHO into C₂₊ compounds involving C–C coupling (Fig. 2). The products include both C₂₊ hydrocarbons (e.g., C₂H₄, C₃H₆ and C₂₊ alkanes) and C₂₊ oxygenates (e.g., ethanol, acetate, *n*-propanol and ethylene glycol), which are important building blocks/synthetic intermediates in the current chemical industry or fuel additives/alternative fuels. The photocatalytic/electrocatalytic systems that are capable of catalysing the formation of C₂₊ compounds from C1 molecules and the active catalyst structures are summarized and analysed to provide insights for design of efficient catalysts. The mechanistic insights such as reactive species, reaction intermediates and reaction pathways are discussed to offer in-depth understanding of the chemistry for the activation of C1 molecules and selective C–C coupling with solar or electrical energy. The challenges, opportunities and future trends in photocatalytic/electrocatalytic

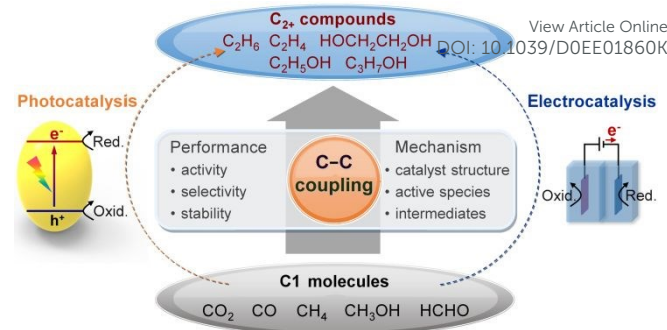


Fig. 2 Major topics of the present article.

transformations of typical C1 molecules are further described to advancing the emerging research area of solar energy- or electrical energy-driven C–C coupling of abundant C1 feedstocks to form high-value C₂₊ compounds.

2. Fundamental aspects of photocatalysis and electrocatalysis

The essence of chemical reactions is the rearrangement of chemical bonds, i.e., the breaking of some chemical bonds in reactants and the formation of new bonds in products. This process usually needs to overcome an activation barrier. Thus, a sufficiently high temperature is required to overcome the activation energy without supply of external energy. For traditional thermocatalysis, the activation energy can be decreased by addition of a catalyst, which can chemically interact with the reactants, and thus can activate the reactants and change the reaction path. On the other hand, for photocatalysis and electrocatalysis, the supplied photo or electrical energy can be applied to reactants via the photocatalyst/electrocatalyst and the reactants are then excited, and thus the reaction can proceed without the need to overcome a high activation energy. Further, photocatalysis and electrocatalysis can also drive the thermodynamically unfavourable reactions that are impossible for thermocatalysis. Therefore, photocatalysis and electrocatalysis hold great potential to bring about breakthroughs toward new reactions or more efficient catalytic processes.

The matching of the energy-band position in semiconductor photocatalysis or the electrode potential in electrocatalysis with the redox potentials of reactants is the key to accomplishing photocatalytic or electrocatalytic reaction due to the thermodynamic requirement. For a semiconductor-based photocatalytic reaction, the conduction-band edge should be higher (more negative) than the reduction potential of the reactant for the reduction half reaction, while the valence-band edge should be lower (more positive) than the oxidation potential of the reactant for the oxidation-half reaction (Fig. 3a). Similarly, for an electrocatalytic reaction, the cathode potential should be higher than the reduction potential and the anode potential should be lower than the oxidation potential of the reactants for the reduction- and oxidation-half reactions,

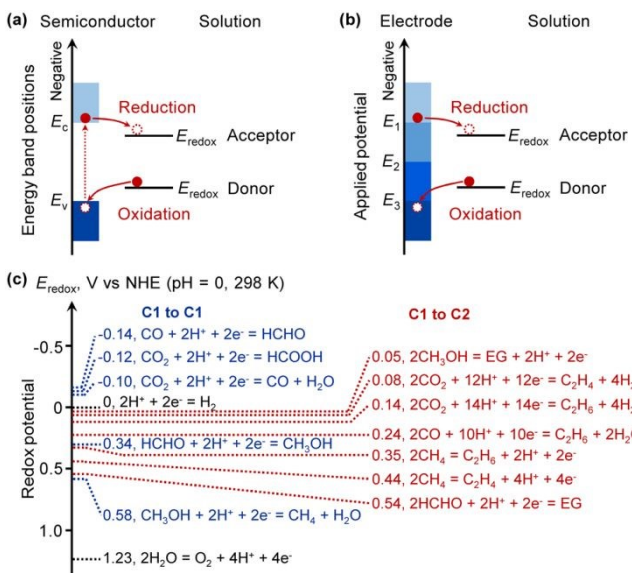


Fig. 3 (a) Positions of semiconductor energy-band edges (E_c, E_v) and substrate redox potentials (E_{redox}), and the thermodynamics of electron transfer between semiconductor and substrate. (b) Positions of electrode applied potentials (E_1, E_2, E_3) and substrate redox potentials (E_{redox}), and the thermodynamics of electron transfer between electrode and substrate. (c) The redox potentials of some reactions related to the conversion of C1 molecules to other C1 or C2 products. The redox potentials are obtained from the thermochemical software "HSC Chemistry".

respectively (Fig. 3b). The energy-band position of the semiconductor or the electrode potential can be tuned by choosing a suitable semiconductor or changing the applied potential. The redox potentials of some possible reactions related to the conversions of typical C1 molecules to some C1 and C₂ compounds are displayed in Fig. 3c. They are all located in the range of -0.2 to 0.6 V versus normal hydrogen electrode (NHE) at 298 K and can be easily matched by controlling the energy-band structure of the semiconductor catalyst or the electrode potential. However, the selectivity control would be difficult from the thermodynamic consideration, because the redox potentials for different products are very close. Therefore, it can be expected that the kinetic control by designing proper photocatalysts/electrocatalysts is crucial to accomplish high selective synthesis of specific C₂₊ compounds.

3. Photocatalytic conversions of CO₂ and CO

3.1. Photocatalytic conversion of CO₂

CO₂ is one of the most stable molecules and also the most probable terminal state of carbon after full utilization of carbon resources. The natural photosynthesis using solar energy to convert CO₂ and H₂O to biomass is the principal step for the carbon cycle in nature.⁴⁴ Many approaches have been proposed and developed for establishing anthropogenic chemical recycle of CO₂ to make the carbon cycle more controllable.⁴⁴ However, the chemical transformation of CO₂ is very challenging due to the thermodynamic stability and kinetic inertness of CO₂. Photocatalytic reduction of CO₂ with H₂O to organic compounds, also known as artificial photosynthesis, is an ideal route for the transformation of CO₂ and the storage of solar energy in chemical bonds.⁴⁵⁻⁵⁰

Since the pioneering work reported by Fujishima, Honda and their co-workers in 1979,⁵⁷ a lot of semiconductors, such as TiO₂,⁵⁸ C₃N₄, Bi₂VO₄, Bi₂WO₆, CdS, SrNb₂O₆, NaTaO₃, Zn₂GeO₄ and Zn₂GaO₄, have been reported for photocatalytic reduction of CO₂ with H₂O.⁴⁵⁻⁵⁰ The products in these systems are often C1 compounds, such as CO, HCOOH, CH₃OH and CH₄. The direct photocatalytic reduction of CO₂ to longer carbon-chain products involving C–C coupling is more challenging not only due to the multi-electron/multi-proton transfer but also because of the requirement of C–C coupling active sites.⁵⁸⁻⁶¹ Nevertheless, some advances have been achieved for the synthesis of C₂₊ compounds such as C₂H₄, C₂H₆ and C₂H₅OH by photocatalytic reduction of CO₂. Some semiconductors, such as TiO₂,⁶² g-C₃N₄,⁶³ BiVO₄,⁶⁴ Bi₂WO₆,⁶⁵ InTaO₄,⁶⁶ CdS,⁶⁷ have been reported to be capable of catalysing the formation of C₂₊ compounds, and some factors are known to play key roles in determining the catalytic performances. Here, we will analyse the effects of doping and co-catalysts, hybridisation of different semiconductors, hybridisation of semiconductors and carbon materials and the presence of plasmonic components on photocatalytic reduction of CO₂ with H₂O to C₂₊ compounds. Some typical photocatalysts and performances are summarized in Table 1.^{62-64, 66-87}

3.1.1. Effects of semiconductor types and doping. TiO₂ is the most intensively studied semiconductor for photocatalytic reduction of CO₂ to C₂₊ compounds, but the yield of C₂₊ products (e.g., C₂H₄, C₂H₆ and C₂H₅OH) was usually lower than that of C1 products (e.g., CO, CH₄ and CH₃OH).⁵⁸⁻⁶¹ An early work showed that the increase in CO₂ pressure and the presence of alkali medium in aqueous solution favoured the formation of C₂₊ products in the pure TiO₂-catalysed CO₂ reduction under UV-light irradiation.⁶² Despite low yields, C₂H₅OH and CH₃CHO were claimed to be formed as major products at a CO₂ pressure of 2.5 MPa in the presence of 0.2 M NaOH.

Visible-light responsive semiconductors have also been investigated for photocatalytic reduction of CO₂ to C₂₊ compounds.⁶³⁻⁶⁷ For example, g-C₃N₄ was reported to catalyse the formation of C₂H₅OH together with CH₃OH during the reduction of CO₂ in 1.0 M NaOH solution under visible-light ($\lambda \geq 420$ nm) irradiation.⁶³ The yield of C₂H₅OH increased proportionally to the irradiation time together with those of CH₃OH and O₂ (Fig. 4). The morphology of g-C₃N₄ was found to influence the catalytic performance; a mesoporous flake-like g-C₃N₄ (denoted as u-g-C₃N₄) showed higher activity than a non-porous flaky g-C₃N₄ (denoted as m-g-C₃N₄). After 12 h reaction, the yields of C₂H₅OH, CH₃OH and O₂ with u-g-C₃N₄ were 10.8, 15.1 and 51.2 μmol, respectively, whereas the yields of C₂H₅OH and O₂ over m-g-C₃N₄ were 8.7 and 24.6 μmol, respectively. The mesoporous structure and large surface area of u-g-C₃N₄ might lead to higher charge separation ability and photocatalytic activity than m-g-C₃N₄. It is surprising that CH₃OH and C₂H₅OH were both formed on u-g-C₃N₄, whereas only C₂H₅OH was observed on m-g-C₃N₄. It is speculated that that H⁺-deficient feature of the system, in particular m-g-C₃N₄, might favour the CO₂ reduction and dimerization to form C₂H₅OH as mentioned in an early work.⁸⁸ Considering that the formations of one mole of CH₃OH and C₂H₅OH require 6 and 12 moles of electrons, respectively, and the formation of 1 mole of O₂ from H₂O requires 4 moles of holes, the ratio of the consumed electrons

REVIEW

Energy & Environmental Science

to holes in the photoredox reactions is nearly 1. This evaluation implies that the

[View Article Online](#)
DOI: 10.1039/D0EE01860K

Table 1 Typical photocatalytic systems for reduction of CO₂ to C₂₊ compounds

Photocatalyst	Formation rate ($\mu\text{mol g}^{-1} \text{h}^{-1}$)	Light source, reaction mode	Ref.
Effects of semiconductor types and doping			
TiO ₂ (effect of electrolytes)	NaOH: CH ₄ , 0.23; CH ₃ OH, 2.5; HCOOH, 0.23; C ₂ H ₅ OH, 11; CH ₃ CHO, 29 H ₂ O: CH ₄ , 0.32; CH ₃ OH, 0.04; HCOOH, 1.7; C ₂ H ₄ , 0.06	Xe lamp, Solid-liquid	62
Mesoporous flake-like g-C ₃ N ₄ (u-g-C ₃ N ₄)	u-g-C ₃ N ₄ : CH ₃ OH, 6.3; C ₂ H ₅ OH, 4.5; O ₂ , 21	Xe lamp (> 420 nm), Solid-liquid	63
Non-porous flaky g-C ₃ N ₄ (m-g-C ₃ N ₄)	m-g-C ₃ N ₄ : C ₂ H ₅ OH, 3.6; O ₂ , 10	Solid-liquid	
BiVO ₄	monoclinic: C ₂ H ₅ OH, 101 tetragonal: C ₂ H ₅ OH, 5.6	Xe lamp (> 400 nm), Solid-liquid	64
1 wt% Co-doped TiO ₂	H ₂ , 63; CH ₃ OH, 26; C ₂ H ₅ OH, 18; CH ₃ CHO, 19	Halogen lamp (> 380 nm), Solid-vapour	68
Cu ²⁺ -doped TiO ₂	CH ₃ OH, 24; C ₂ H ₅ OH, 47	365 nm LED lamp, Solid-vapour	69
TiO ₂	CH ₃ OH, 6.7; C ₂ H ₅ OH, 6.3	Solid-vapour	
Hybridisation of semiconductors and a semiconductor with a nanocarbon material			
4 nm PbS QD–Cu/TiO ₂	CH ₄ , 0.58; CO, 0.82; C ₂ H ₆ , 0.31	Xe lamp (> 420 nm), Solid-vapour	70
AgBr–TiO ₂	CH ₄ , 26; CH ₃ OH, 16; CO, 6; C ₂ H ₅ OH, 2.7	Xe lamp (> 420 nm), Solid-liquid	71
AgBr–NG–g-C ₃ N ₄	CH ₃ OH, 21; C ₂ H ₅ OH, 51	Xe lamp (> 420 nm), Solid-liquid	72
CNT–TiO ₂	CH ₄ , 12; HCOOH, 19; C ₂ H ₅ OH, 30	UV lamp (365 nm), Solid-vapour	73
GO–TiO ₂	CH ₃ OH, 12; C ₂ H ₅ OH, 145	Hg lamp, Solid-liquid	74
2%G–TiO ₂	CH ₄ , 8.0; C ₂ H ₆ , 16.8	Xe lamp, Solid-vapour	75
0.5G–TiO _{2-x}	CH ₄ , 7.4; C ₂ H ₆ , 1.2	Solar simulator (AM 1.5), Solid-vapour	76
1%Pt–0.5G–TiO _{2-x}	CH ₄ , 37; C ₂ H ₆ , 11	Solid-vapour	
carbon-coated Cu ₂ O nanorods	CH ₄ , 0.014; C ₂ H ₄ , 0.019; O ₂ , 0.15 $\mu\text{mol h}^{-1}$	Xe lamp (> 420 nm), Solid-liquid	77
Effect of co-catalyst			
1%Pd/TiO ₂	CH ₄ , 0.37; CO, 0.033; C ₂ H ₆ , 0.067	Hg lamp, Solid-liquid	78
Nafion-modified Pd/TiO ₂	CH ₄ , 2.2; C ₂ H ₆ , 1.0 $\mu\text{mol h}^{-1}$	UV lamp (> 300 nm), Solid-liquid	79
Pd/TiO ₂	CH ₄ , 2.1; C ₂ H ₆ , 0.47 $\mu\text{mol h}^{-1}$	Solid-liquid	
Rh nanowires/TiO ₂	H ₂ , 11; CH ₄ , 4.5; CO, 14; C ₂ H ₅ OH, 12	Xe lamp (< 400 nm), Solid-vapour	80
2.6%NiO/InTaO ₄	CH ₃ CHO, 0.3	Xe lamp (AM 1.5), Solid-vapour	66
NiO/Na _{1-x} La _x TaO _{3+x}	H ₂ , 0.2; CH ₄ , 0.02; CH ₃ OH, 60; C ₂ H ₆ , 0.01; C ₂ H ₄ , 0.14; C ₂ H ₅ OH, 19; CH ₃ CHO, 2.2; C ₃ H ₆ , 0.4	Hg lamp (300–700 nm), Solid-liquid	81
CdS/(Cu-Na _{1.5} H _{0.5} Ti ₃ O ₇)	CH ₄ , 28; C ₂ H ₆ , 17; C ₂ H ₄ , 0.1; C ₃ H ₈ , 9.7; C ₃ H ₆ , 0.8 $\mu\text{L g}^{-1} \text{h}^{-1}$	Xe lamp (> 420 nm), Solid-liquid	67
5%Cu/TiO ₂	CH ₄ , 0.29; C ₂ H ₆ , 0.02; C ₂ H ₄ , 0.54 $\mu\text{L g}^{-1} \text{h}^{-1}$	Xe lamp, Solid-liquid	82
Cu–Pt/nitrogen-doped TiO ₂ nanotube array	H ₂ , 160; CH ₄ , 75; other alkanes, 25; olefin, 8.5; Branched paraffin, 2.5 ppm $\text{cm}^{-2} \text{h}^{-1}$	Outdoor sunlight (AM 1.5), Solid-vapour	83
Cu _{0.33} Pt _{0.67} /PMTiNT	CH ₄ , 2.6; C ₂ H ₆ , 0.47; C ₂ H ₄ , 0.24 mL $\text{g}^{-1} \text{h}^{-1}$	Solar simulator (AM 1.5), Solid-vapour	84
Cu(0.5 wt%)-Fe(0.5 wt%)/TiO ₂	glass plate: CH ₄ , 0.06; C ₂ H ₄ , 0.05 optical fiber: CH ₄ , 0.91; C ₂ H ₄ , 0.58	Hg lamp (320–580 nm), Solid-vapour	85
Plasmonic effect			
Au/TiO ₂	CH ₄ , 231; CH ₃ OH, 87; HCHO, 135; C ₂ H ₆ , 162 $\mu\text{mol m}^{-2}$	Hg lamp (254 nm), Solid-vapour	86
Au nanoparticle in 5%EMIM-BF ₄ aqueous solution	TOF: CH ₄ , 4.5; C ₂ H ₆ , 0.99; C ₂ H ₄ , 1.1; C ₃ H ₈ , 0.56; C ₃ H ₆ , 0.93 $\text{NP}^{-1} \text{h}^{-1}$	532 nm laser, Solid-liquid	87

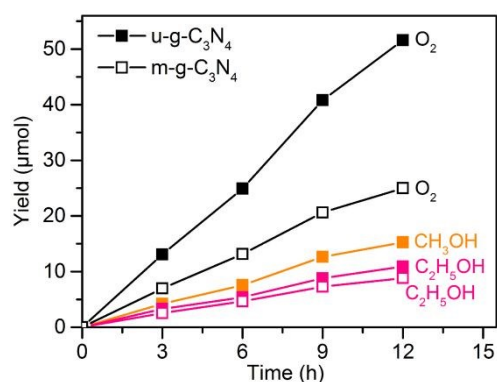


Fig. 4 Photocatalytic conversion CO_2 with H_2O to CH_3OH , $\text{C}_2\text{H}_5\text{OH}$ and O_2 over $\text{u-g-C}_3\text{N}_4$ and $\text{m-g-C}_3\text{N}_4$ under visible-light irradiation.⁶³

results may be reliable. Nevertheless, the confirmation of the source of products by using for example $^{13}\text{CO}_2$ as the reactant is necessary for the carbon-containing photocatalysts or photocatalytic systems.

The doping of a metal or non-metal element is a useful strategy to tune the energy-band structure of semiconductors for CO_2 photoreduction.^{48,49} Generally, the metal doping can create intra-band states below the conduction band, whereas the non-metal doping is capable of forming intra-band states above the valence band. Both may narrow the bandgap and extend light absorption range. Moreover, the metal or non-metal doping may also generate surface vacancies or new active sites, thus affecting the CO_2 activation and reduction. In this case, the metal dopant may also function like as a co-catalyst.

Some studies have investigated the effect of metal or metal cation dopants, such as Cu, Fe, V, Cr, Co and Rh, in TiO_2 on the photocatalytic reduction of CO_2 to C_2 compounds.^{68,69} As compared to the UV-light responsive TiO_2 , the cationic V-, Cr- and Co-doped TiO_2 catalysts extended the absorption spectrum into visible-light region, thus enabling the photocatalytic reduction of CO_2 under visible-light irradiation.⁶⁸ It was found that the Co^{2+} -doped TiO_2 showed higher photocatalytic activity than the other metal cation-doped catalysts, but the product selectivities for the V-, Cr- and Co-doped TiO_2 were similar, the major reduction products were H_2 , CH_3OH , $\text{C}_2\text{H}_5\text{OH}$ and CH_3CHO .⁶⁸ The performance was also strongly dependent on the doping amount of Co^{2+} , and the formation rates of H_2 , CH_3OH , $\text{C}_2\text{H}_5\text{OH}$ and CH_3CHO over the 1 wt% Co-doped TiO_2 reached 63, 26, 18 and 19 $\mu\text{mol g}^{-1} \text{h}^{-1}$, respectively.⁶⁸ A Cu^{2+} -doped TiO_2 nanorod thin film catalyst was also claimed to be efficient for the gas-phase reduction of CO_2 with H_2O vapour to CH_3OH and $\text{C}_2\text{H}_5\text{OH}$ under UV-light irradiation.⁶⁹ The reaction was carried out in a flow-type optofluidic planar microreactor, and the formation rates of CH_3OH and $\text{C}_2\text{H}_5\text{OH}$ with Cu^{2+} -doped TiO_2 reached 24 and 47 $\mu\text{mol g}^{-1} \text{h}^{-1}$, respectively at a CO_2 flow rate of 2 mL min^{-1} and 60 °C, whereas they were only 6.7 and 6.3 $\mu\text{mol g}^{-1} \text{h}^{-1}$, respectively, with TiO_2 alone. The increase in temperature to 80 °C could further increase the formation rates of CH_3OH and $\text{C}_2\text{H}_5\text{OH}$ to 36 and 79 $\mu\text{mol g}^{-1} \text{h}^{-1}$, respectively.⁶⁹ Besides the decreased band-gap energy and the extended light absorption, the doped Cu^{2+} ions was supposed to serve as active sites of electron traps and suppress the electron-hole

recombination. Thus, the doped metal cation centre may also play a role as a co-catalyst, which will be discussed later.

3.1.2. Hybridisation of semiconductors and a semiconductor with a nanocarbon material. The combination of two different semiconductors can form heterojunctions at the interface of the two semiconductors. The construction of a hybrid photocatalyst may not only enhance the light absorption and charge separation but also drive the transfer of photogenerated electrons and holes between the two semiconductors, thus affecting the catalytic activity and selectivity.⁴⁶ The charge transfer between different semiconductors proceeds through three main kinds of mechanisms including sensitisation, p-n junction and Z-scheme mechanisms. As for photocatalytic reduction of CO_2 with H_2O , a semiconductor may either have high ability for O_2 evolution with photogenerated holes or be good at the reduction of CO_2 to C_{2+} compounds with the photogenerated electrons. The hybridisation of the O_2 -evolution semiconductor A with the CO_2 reduction semiconductor B through p-n junction or Z-scheme can drive the transfer of photogenerated electrons to semiconductor B for reducing CO_2 and photogenerated holes to semiconductor A for oxidizing H_2O (Fig. 5).

Some hybrid photocatalysts were reported for the photocatalytic reduction of CO_2 to products including C_{2+} products such as $\text{C}_2\text{H}_5\text{OH}$ and C_2H_6 together with C1 compounds.^{70,71,89} For example, the combination of PdS quantum dots (QDs) with TiO_2 could increase the rate of CO_2 photocatalytic reduction by a factor of 5 because of the sensitisation effect of PbS QDs, which made the utilisation of visible and near-infrared light possible.⁷⁰ CO , CH_4 and C_2H_6 were the major products over the PbS-TiO_2 nanocomposite. Similarly, AgBr-TiO_2 could catalyse the reduction of CO_2 to CH_4 , CH_3OH , CO and $\text{C}_2\text{H}_5\text{OH}$ under visible-light irradiation because of the sensitisation effect of AgBr .⁷¹ The light-harvesting complex II (LHCII), which was extracted from spinach and functioned as a sensitizer, was combined with Rh-doped TiO_2 for photocatalytic reduction of CO_2 in aqueous solution under visible-light irradiation, offering acetaldehyde, CO and methyl formate as major products.⁸⁹ The formation rates of CO , acetaldehyde and methyl formate were 0.57, 3.2 and 0.26 $\mu\text{mol g}^{-1} \text{h}^{-1}$. Han, Niu and their co-workers loaded AgBr nanoparticles onto g- C_3N_4 -decorated N-doped graphene (NG) and found that this nanocomposite showed excellent performance for the photocatalytic reduction of CO_2 to $\text{C}_2\text{H}_5\text{OH}$ under visible-light irradiation.⁷² The reaction was proposed to proceed by the scheme of Fig. 5a and the

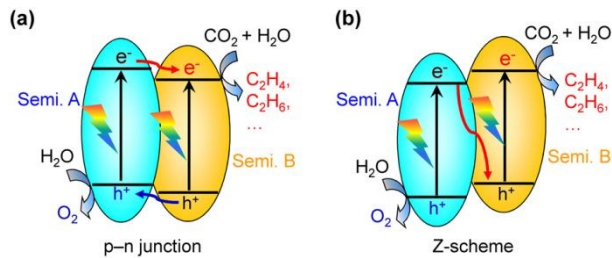


Fig. 5 Schematic illustrations of hybridisation of two different semiconductors for photocatalytic CO_2 reduction to C_{2+} compounds. (a) p-n junction. (b) Z-scheme.

REVIEW

Energy & Environmental Science

reduction of CO_2 took place on AgBr nanoparticles. The rate of $\text{C}_2\text{H}_5\text{OH}$ formation reached $51 \mu\text{mol g}^{-1} \text{h}^{-1}$, 2.4 times of that of CH_3OH over the ternary composite.⁷²

Nanocarbon materials, such as graphene (G), graphene oxide (GO) and carbon nanotubes (CNTs), have been widely used to fabricate hybrid photocatalysts, owing to their high conductivity, good electron mobility, favourable Fermi levels and large surface areas.¹⁷ The nanocarbon can serve as an electron collector or transporter to enhance the charge separation, an active surface to facilitate the adsorption of reactants or a protector to inhibit semiconductor photo-corrosion. Some nanocarbon-semiconductor hybrid photocatalysts, such as CNT-TiO₂, GO-TiO₂, G-TiO₂, G-TiO_{2-x} and carbon-Cu₂O, could offer C_{2+} compounds during photocatalytic reduction of CO_2 .⁷³⁻⁷⁷

A CNT-TiO₂ nanocomposite was reported to provide CH_4 , HCOOH and $\text{C}_2\text{H}_5\text{OH}$ as the major products during the reduction of CO_2 with H_2O vapour under UV-light ($\lambda = 365 \text{ nm}$) irradiation, and the formation rate of $\text{C}_2\text{H}_5\text{OH}$ reached $\sim 30 \mu\text{mol g}^{-1} \text{h}^{-1}$, higher than those of CH_4 ($12 \mu\text{mol g}^{-1} \text{h}^{-1}$) and HCOOH ($19 \mu\text{mol g}^{-1} \text{h}^{-1}$).⁷³ A GO-TiO₂ hybrid suspended in aqueous medium was also claimed to offer $\text{C}_2\text{H}_5\text{OH}$ together with CH_3OH during the reduction of CO_2 under UV-vis-light irradiation.⁷⁴ It was found that the pH value of the aqueous solution influenced the products; CH_3OH was the major product at a lower pH value, whereas $\text{C}_2\text{H}_5\text{OH}$ became the major product at a higher pH value. The formation rate of $\text{C}_2\text{H}_5\text{OH}$ reached $\sim 145 \mu\text{mol g}^{-1} \text{h}^{-1}$ at a pH of 11.⁷⁴ It was speculated that the pH value of the aqueous solution might affect the point of zero charge of catalyst surface and thus the interaction between carbonate species and the surface.⁷⁴ It is, however, surprising that $\text{C}_2\text{H}_5\text{OH}$ was also reported to be the major product with a formation rate of $\sim 110 \mu\text{mol g}^{-1} \text{h}^{-1}$ over TiO₂ (P25) alone. Such a high $\text{C}_2\text{H}_5\text{OH}$ formation rate for TiO₂ alone has not been reported by other groups.

On the other hand, Zou and co-workers showed that a G-TiO₂ hybrid photocatalyst with 2D sandwich-like nanosheet morphology could function for the reduction of CO_2 with H_2O vapour to C_2H_6 along with CH_4 under UV-light irradiation.⁷⁵ The G-TiO₂ nanocomposite was fabricated by a simultaneous reduction-hydrolysis strategy in ethylenediamine/ H_2O solvent, by which the reduction of GO to graphene by ethylenediamine and the hydrolysis of Ti^{4+} to TiO₂ took place simultaneously. The pure TiO₂ synthesized by the same procedure showed a better performance for CO_2 reduction than P25 probably owing to the abundant Ti^{3+} sites on TiO₂, and the formation rates of CH_4 and C_2H_6 were 10 and $7.2 \mu\text{mol g}^{-1} \text{h}^{-1}$, respectively. Upon increasing the content of graphene in G-TiO₂ from 0 to 2 wt\% , the formation rate of CH_4 somewhat decreased but that of C_2H_6 increased significantly (Fig. 6a).⁷⁵ Although a further increase in the content of graphene decreased the formation rate of total products, the molar ratio of C_2H_6 to CH_4 increased monotonically with the content of graphene to 5 wt\% , suggesting that the introduction of graphene favoured the formation of C_2H_6 . The 2% G-TiO₂ offered the highest total product formation rate, and the formation rates of CH_4 and C_2H_6 reached 8.0 and $16.8 \mu\text{mol g}^{-1} \text{h}^{-1}$, respectively. Both Ti^{3+} sites on TiO₂ surfaces and the presence of graphene are proposed to play key roles in photosynthesis of C_2H_6 from CO_2 . It is speculated that the abundant surface Ti^{3+} sites can work for trapping photogenerated electrons and the electrons may be further

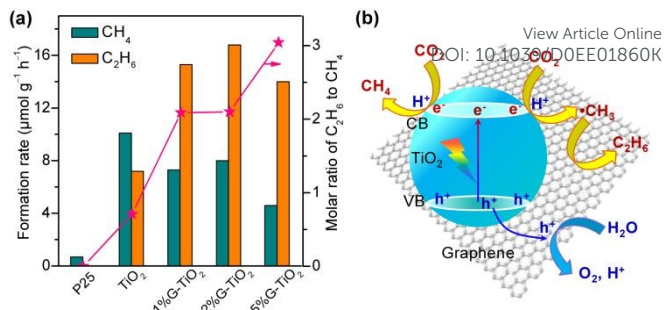


Fig. 6 (a) Photocatalytic reduction of CO_2 to CH_4 and C_2H_6 over graphene-TiO₂ hybrid under UV-light irradiation.⁷⁵ (b) Schematic illustration of photocatalytic reduction of CO_2 over a graphene-TiO₂ hybrid.⁷⁶

accumulated on graphene, both favouring the multi-electron reduction of CO_2 to CH_3^{\bullet} . The electron-rich graphene may also be beneficial to stabilising CH_3^{\bullet} , the reaction intermediate, and thus limit the combination of CH_3^{\bullet} with H^+ and e⁻ into CH_4 . At the same time, the accumulation of CH_3^{\bullet} on graphene may contribute to increasing the probability of coupling of CH_3^{\bullet} to form C_2H_6 .⁷⁵

In and co-workers fabricated a graphene-wrapped reduced blue titania (G-TiO_{2-x}) loaded with a small amount of Pt nanoparticles and found that this nanocomposite showed a high formation rate of C_2H_6 and CH_4 in the photocatalytic reduction of CO_2 in a continuous flow-through (CO_2 , H_2O) photo-reactor under one sun AM1.5G illumination.⁷⁶ P25 was inactive under such circumstance and the TiO_{2-x} catalysed the formation of CH_4 with a rate of $1.0 \mu\text{mol g}^{-1} \text{h}^{-1}$. The presence of graphene not only enhanced the formation of CH_4 but also induced the formation of C_2H_6 , and the loading to a small amount of Pt could further accelerate the formations of both CH_4 and C_2H_6 . The formation rates of CH_4 and C_2H_6 could reach 37 and $11 \mu\text{mol g}^{-1} \text{h}^{-1}$, corresponding to CH_4 and C_2H_6 selectivities of 77% and 23% , respectively.⁷⁶ This work provided solid evidence for the formation of CH_4 and C_2H_6 from CO_2 by $^{13}\text{CO}_2$ isotopic control experiments. CH_3^{\bullet} radical was proposed to be the intermediate for the formations of both CH_4 and C_2H_6 . In other words, CH_4 is formed by the reaction of CH_3^{\bullet} with H^+ and e⁻, whereas the coupling of two CH_3^{\bullet} radicals gives C_2H_6 . However, different from Zou and co-workers,⁷⁷ In and co-workers proposed through transient absorption spectroscopy studies that photogenerated holes rather electrons migrate to graphene, where the oxidation of H_2O occurs, whereas the reduction of CO_2 takes place on TiO_{2-x} surfaces, where the electrons accumulate.⁷⁶ Nevertheless, In and co-workers also speculate that graphene might stabilise CH_3^{\bullet} radicals, enabling the increased probability for C_2H_6 formation (Fig. 6b).

Yu et al. reported that the coating of a carbon layer onto mesoporous Cu₂O nanorods deposited on Cu foils could also enhance the photocatalytic reduction of CO_2 , but they observed the formation of CH_4 and C_2H_4 .⁷⁷ The photocatalytic reaction was carried out in KHCO₃ aqueous solution under visible-light irradiation. Cu₂O nanorods on Cu foils alone could offer CH_4 and C_2H_4 with almost the same amount, but the amounts of CH_4 and C_2H_4 did not increase with time after $\sim 6 \text{ h}$ of reaction because of the photo-corrosion of Cu₂O. The coating of carbon layer enhanced the formation of C_2H_4 , the amount of which became ~ 1.3 times of that of CH_4 , and the amounts of C_2H_4 and CH_4 kept increasing with time at least in 12 h over the carbon-coated Cu₂O nanorods. The total amounts of C_2H_4 and CH_4

was 0.037 μmol after 12 h of reaction. The carbon layer was proposed to work as a protective layer to quench the photo-corrosion of Cu_2O and to extract photogenerated electrons, thus accelerating the separation of electron-hole pairs and the transfer of multitude of electrons for the formation of C_2H_4 . Although the formation rates of C_2H_4 and CH_4 reported in this work were quite low, it is noteworthy to point out that the ^{13}C -labelling isotopic experiment using $^{13}\text{CO}_2$ and the measurement of the evolved O_2 provided solid evidence that C_2H_4 and CH_4 were produced by the reduction of CO_2 in such a carbon-containing catalyst system.⁷⁷

3.1.3. Effect of co-catalyst. The design of a proper co-catalyst is one of the most important strategies to improve the efficiency of a photocatalytic reaction.^{49,90,91} The co-catalyst can provide trapping sites for photogenerated charges and promote their separation, thus enhancing photocatalytic activity. The fabrication of suitable co-catalysts on semiconductors can also offer active sites/reaction sites and facilitate oxidation and reduction reactions by lowering the activation energy. Because of the inertness of CO_2 molecule and various possible products, the co-catalyst plays crucial roles not only in improving the activity through promoting the charge separation and the adsorption/activation of CO_2 but also in tuning the product selectivity. In this section, we will focus on the role of co-catalysts in the semiconductor-based photocatalytic reduction of CO_2 and will demonstrate the effects of co-catalysts on promoting the activity for CO_2 reduction and improving the selectivity toward C–C coupling products.

Noble and coinage metals (such as Pt, Pd, Rh, Au, Ag and Cu) have been used as co-catalysts for TiO_2 -based photocatalytic reduction of CO_2 with H_2O .^{49,92} Among the noble and coinage metal co-catalysts, Pt is known to be the most efficient in extracting electrons from a semiconductor and in promoting CO_2 reduction, but the reduction of H_2O to H_2 is also enhanced at the same time because of the fast recombination of H atoms on Pt. The co-catalyst that can efficiently extract conduction-band electrons but has lower ability of H atom recombination to H_2 is beneficial to CO_2 reduction.

Pd is a good candidate of such a co-catalyst because of the retarded recombination of H atoms on Pd surfaces. Ishitani and co-workers found that the photocatalytic reduction of CO_2 in aqueous solution with TiO_2 suspended provided CO as the major product and the loading of Pd onto TiO_2 remarkably enhanced the formation of CH_4 (Fig. 7a).⁷⁸ It is noteworthy that the formation of C_2H_6 was

observed over the Pd/TiO_2 , although rate of C_2H_6 formation was about 6 times lower than that of CH_4 (Fig. 7a).⁷⁸ The acidic/base property of the support, which was used to load the semiconductor, was found to influence the selectivity of photocatalytic reduction of CO_2 to C1 or C₂₊ products.⁹³ The result implied that the introduction of an acidic support favoured the formation of C1 products, whereas the basic support such as MgO or basic promoter (e.g., Li^+) was beneficial to the formation of C₂₊ products such as C_2H_6 , which were supposed to be formed by dimerization of radical intermediates (e.g., $\text{CH}_3\bullet$).⁹³ On the other hand, Choi and co-workers demonstrated that the introduction of a thin layer of acidic Nafion (perfluorinated polymer with sulfonated groups) onto Pd/TiO_2 could significantly enhance the photocatalytic reduction of CO_2 in aqueous solution with different pH values not only to CH_4 but also to C_2H_6 (Fig. 7b).⁷⁹ In particular, the effect of Nafion was still remarkable for the formation of C_2H_6 even at a pH value of 1, whereas the enhancement in CH_4 formation due to the Nafion layer was insignificant at such a low pH value. A small amount of C_3H_8 was detected over the Nafion-modified Pd/TiO_2 but not over the Pd/TiO_2 . The formation of C_2H_6 and C_3H_8 requires more protons and electrons than that of CH_4 . Choi and co-workers strengthened the crucial role of proton-coupled multi-electron transfer in the formation of C_2H_6 and C_3H_8 . It is speculated that at a lower pH value ($\text{pH} = 1$), protons may be sufficient at the surface active site for the formation of CH_4 without the need of Nafion.⁷⁹ The presence of Nafion layer accelerated the formation of C_2H_6 and C_3H_8 even at an acidic environment ($\text{pH} = 1$) because the Nafion layer might enhance the local proton activity to facilitate the proton-coupled multi-electron transfer processes. The Nafion layer might also stabilise the intermediates (probably radicals) involving in the formation of C_2H_6 and C_3H_8 .

The morphology of co-catalyst may affect the interface between co-catalyst and semiconductor, and thus influencing the photocatalytic reduction of CO_2 . Rh and Pd nanowires loaded onto TiO_2 nanosheets were found to be more efficient co-catalysts than the corresponding nanoparticles for photocatalytic reduction of CO_2 with H_2O under UV-light irradiation.⁸⁰ The use of nanowire co-catalysts reduced the H_2 evolution and enhanced the reduction of CO_2 . The larger density of grain boundaries between co-catalyst and TiO_2 in the nanowire-based photocatalyst was proposed to be the key. CO, CH_4 and $\text{C}_2\text{H}_5\text{OH}$ were the major products, and the rates of CO, CH_4 and $\text{C}_2\text{H}_5\text{OH}$ reached 4.5, 14 and 12 $\mu\text{mol g}^{-1} \text{h}^{-1}$ over the Rh-nanowire-loaded TiO_2 nanosheet catalyst.⁸⁰ The molar ratios of CO, CH_4 and $\text{C}_2\text{H}_5\text{OH}$ were comparable between Rh nanowire- and Rh nanoparticle-based catalysts.

NiO was reported to be an efficient co-catalyst for photocatalytic reduction of CO_2 in a few studies.^{66,81} NiO/InTaO₄ photocatalysts with different NiO contents were investigated for photocatalytic reduction of CO_2 with H_2O vapour in a monolith reactor with optical fibres inserted inside, i.e., an internally illuminated monolith reactor.⁶⁶ It is of interest that acetaldehyde was formed with a considerable amount under UV-light or simulated-sunlight irradiation. The formation rate of acetaldehyde increased with the content of NiO and reached 0.21 $\mu\text{mol g}^{-1} \text{h}^{-1}$ over the 2.6 wt% NiO/InTaO₄ catalyst at 30 °C under AM1.5G irradiation.⁶⁶ The increase in temperature to 70 °C slightly increased the formation rate of acetaldehyde to 0.30 $\mu\text{mol g}^{-1} \text{h}^{-1}$. A NiO/Na_{1-x}La_xTaO_{3+x} catalyst was reported to offer CH_3OH and $\text{C}_2\text{H}_5\text{OH}$ during photocatalytic

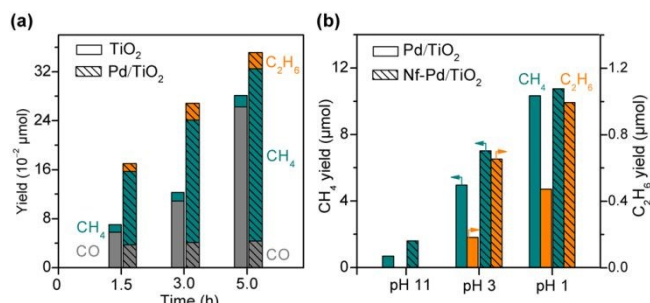


Fig. 7 (a) Photocatalytic reduction of CO_2 over TiO_2 and 1%Pd/ TiO_2 .⁷⁸ (b) Effect of Nafion (Nf) layer deposited on Pd/ TiO_2 on photocatalytic reduction of CO_2 .⁷⁹

REVIEW

Energy & Environmental Science

reduction of CO_2 in 0.2 M NaOH aqueous solution under UV-light irradiation.⁸¹ The rates of CH_3OH and $\text{C}_2\text{H}_5\text{OH}$ reached 59.6 and 18.8 $\mu\text{mol g}^{-1} \text{ h}^{-1}$, respectively over the $\text{NiO}/\text{Na}_{1-x}\text{La}_x\text{TaO}_{3+x}$ catalyst, whereas they were 35.0 and 6.4 $\mu\text{mol g}^{-1} \text{ h}^{-1}$, respectively in the absence of NiO. Thus, NiO might play a crucial role in accelerating the formation of C_2 oxygenates by increasing the charge separation and C_2 oxygenate selectivity.

Among noble or coinage metals, Cu is a very attractive co-catalyst that can accelerate the formation of C_{2+} hydrocarbons.^{58,67,94} An early study showed that the Cu-loaded TiO_2 powders suspended in aqueous solution, which was pressurised CO_2 (2.8 MPa), could catalyse the reduction of CO_2 into CH_4 , C_2H_4 and C_2H_6 with yields of 21.8, 26.2 and 2.7 $\mu\text{L g}^{-1}$ under optimised conditions.⁸² A Cu^{2+} -doped TiO_2 nanorod thin film catalyst was recently reported to offer CH_3OH and $\text{C}_2\text{H}_5\text{OH}$ as the major products during the gas-phase reduction of CO_2 with H_2O vapour under UV-light irradiation in a flow-type optofluidic planar microreactor.⁶⁹ The formation rates of CH_3OH and $\text{C}_2\text{H}_5\text{OH}$ reached 24 and 47 $\mu\text{mol g}^{-1} \text{ h}^{-1}$, respectively. For a nitrogen-doped TiO_2 nanotube array, the presence of Cu as a co-catalyst enhanced the formation of hydrocarbons including CH_4 and $\text{C}_2\text{--C}_6$ paraffins as well as minor olefins during the photocatalytic reduction of CO_2 with H_2O vapour under outdoor sunlight.⁸³ On the other hand, the employment of Pt co-catalyst mainly enhanced the formation of H_2 by accelerating the reduction of H_2O under the same reaction circumstance.

Hoffmann and co-workers reported an interesting $\text{CdS}/\text{Cu-TNTs}$ photocatalyst fabricated by coating CdS QDs on Cu-deposited sodium trititanate nanotubes (TNTs, $\text{Na}_x\text{H}_{2-x}\text{Ti}_3\text{O}_7$) and found that this ternary photocatalyst was capable of working for photocatalytic reduction of CO_2 in aqueous solution to $\text{C}_1\text{--C}_3$ hydrocarbons under visible-light ($\lambda \geq 420$ nm) irradiation.⁶⁷ Over the ternary catalyst, photogenerated electrons can transfer from CdS QDs to Cu particle surface through the titanate nanotube framework and the reduction of CO_2 to $\text{C}_1\text{--C}_3$ hydrocarbons may mainly proceed on the Cu surfaces. The formation rates of CH_4 , C_2H_6 and C_3H_8 were 28, 17 and 9.7 $\mu\text{L g}^{-1} \text{ h}^{-1}$, and minor amounts of C_2H_4 (0.1 $\mu\text{L g}^{-1} \text{ h}^{-1}$) and C_3H_6 (0.8 $\mu\text{L g}^{-1} \text{ h}^{-1}$) were also formed. The isotopic labelling experiments using $^{13}\text{CO}_2$ confirmed that most of the hydrocarbons were formed by the reduction of CO_2 , and a part of CH_4 may be formed by organic compound contamination.⁶⁷ Cu was found to be crucial in the formation of C_2 and C_3 hydrocarbons. Hoffmann and co-workers performed a mechanistic study using the $\text{CdS}/\text{Cu-TNTs}$ catalyst. The formation of $\text{CH}_3\bullet$ was confirmed through the EPR characterization of the formed radicals using DMPO as a spin trapping reagent. It is speculated that CO_2 reduction is initiated most likely by a one-electron reduction to $\text{CO}_2^{\bullet-}$, which then reacts with $\text{H}\bullet$ to produce hydrocarbons through $\text{CH}_3\bullet$ radicals (Fig. 8).⁶⁷ The Fischer-Tropsch

route for the formation of hydrocarbons may not occur in the present system because no evolution of H_2 and CO was observed at the low temperature. Lower-intensity of signals ascribed to $\text{CH}_3\bullet$ was observed in the absence of Cu, suggesting that Cu played a key role in accelerating the formation of $\text{CH}_3\bullet$.

As compared to a single metal co-catalyst, a bimetallic or alloy co-catalyst may have a potential to further improve the catalytic activity and/or selectivity of a semiconductor photocatalyst. Grimes and co-workers co-loaded Cu and Pt nanoparticles on nitrogen-doped titania nanotube arrays (NT), and conducted photocatalytic reduction of CO_2 under outdoor sunlight irradiation.^{58,83} The formation rates of H_2 and hydrocarbons were 61 and 104 ppm $\text{cm}^{-2} \text{ h}^{-1}$ over the Cu/NT, respectively, whereas they were 190 and 82 ppm $\text{cm}^{-2} \text{ h}^{-1}$ over the Pt/NT.⁸³ The formation rate of hydrocarbons over the Cu-Pt/NT was 111 ppm $\text{cm}^{-2} \text{ h}^{-1}$, which was close to that over Cu/NT, while the formation rate of H_2 was 160 ppm $\text{cm}^{-2} \text{ h}^{-1}$ over the bimetallic catalyst, close to that of Pt/NT. The co-loading of Cu and Pt nanoparticles did not show significant synergistic effect on tuning the selectivity of C_{2+} hydrocarbons. The fabrication of core-shell structured Pt@Cu co-catalyst with Pt as the core and Cu as the shell to cover Pt could promote both the extraction of photogenerated electrons by Pt and the reduction of CO_2 to CH_4 .⁹⁵ Shankar and co-workers synthesized CuPt alloy co-catalysts with different Cu/Pt molar ratios on a periodically modulated double-walled TiO_2 nanotube (PMTiNT) array and found that the $\text{Cu}_{0.33}\text{Pt}_{0.67}/\text{PMTiNT}$ showed the highest performance for photocatalytic reduction of CO_2 to CH_4 , C_2H_4 , and C_2H_6 under simulated one-sun AM1.5 illumination.⁸⁴ It is of interest that the present system could work for the reduction of not only concentrated CO_2 (99.9%) but also diluted CO_2 (0.998%). The formation rates of CH_4 , C_2H_4 and C_2H_6 over $\text{Cu}_{0.33}\text{Pt}_{0.67}/\text{PMTiNT}$ reached 2.60, 0.24 and 0.47 $\text{mL g}^{-1} \text{ h}^{-1}$, respectively.⁸⁴ In contrast, the formation rates of hydrocarbons over the Cu/PMTiNT and Pt/PMTiNT were both quite lower (0.61 and 0.20 $\text{mL g}^{-1} \text{ h}^{-1}$, respectively), further suggesting the role of CuPt alloy co-catalyst in photocatalytic reduction of CO_2 . A recent work by In and co-workers further adopted the bimetallic Cu-Pt nanoparticles as co-catalysts of blue titania (BT) for photocatalytic reduction of CO_2 with H_2O vapour in a flow-through reactor under AM1.5 illumination.⁹⁶ It was found that the configuration of bimetallic nanoparticles had a significant effect on catalytic performance; the deposition of Cu atop Pt particles directly attached on blue titania was optimal. Photogenerated electrons were believed to be extracted from blue titania to Pt, due to the interfacial charge transfer phenomenon, which was confirmed by photoluminescence spectroscopy. All extracted photogenerated electrons were then transferred to Cu, resulting in an enriched electron density within Cu, and CO_2 was activated and reduced on Cu surfaces. Over a 6 h period, the $\text{Cu}_{1.00\%}\text{--Pt}_{0.35\%}\text{-BT}$ catalyst offered CH_4 and C_2H_6 with yields of 3.0 and 0.15 mmol g^{-1} , respectively, and the sunlight to fuel (CH_4 and C_2H_6) photoconversion efficiency reached 1% with an apparent quantum yield of 86%.⁹⁶ This sunlight to fuel (CH_4 and C_2H_6) photoconversion efficiency is significantly higher than those reported before (~0.03%).⁵⁸

In addition, a Cu and Fe co-doped TiO_2 photocatalyst was studied for photocatalytic reduction of CO_2 with H_2O vapour under UV-light irradiation.⁸⁵ The photocatalyst was intriguingly coated on optical

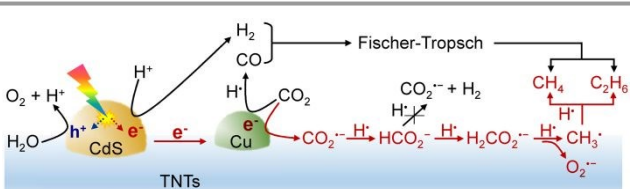


Fig. 8 Proposed reaction pathways for photocatalytic reduction of CO_2 to hydrocarbons over the $\text{CdS}/\text{Cu-TNTs}$ catalyst.⁶⁷

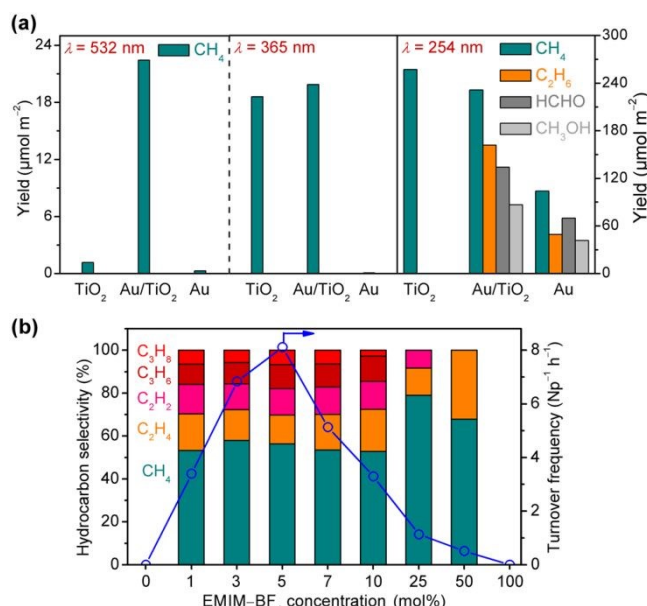


Fig. 9 (a) Photocatalytic reduction of CO₂ over TiO₂, Au/TiO₂ and Au under light irradiation with different wavelengths.⁸⁶ (b) Hydrocarbon selectivity and total hydrocarbon turnover frequency in photocatalytic reduction of CO₂ over plasmonic Au nanoparticle photocatalyst in aqueous solutions with different concentrations of EMIM-BF₄.⁸⁷

fibres, which were assembled into a flow reactor. This configuration of reactor showed significant advantages in improving the CO₂ reduction activity. The presence of Fe together with Cu was found to suppress the formation of CH₄ but enhanced that of C₂H₄, and the Cu(0.5 wt%)-Fe(0.5 wt%)/TiO₂ catalyst offered a C₂H₄ formation rate of 0.58 μmol g⁻¹ h⁻¹.

3.1.4. Plasmonic effect. The Au and Ag nanoparticles have superior surface plasmon resonance (SPR) or localised surface plasmon resonance (LSPR) effect, and thus can work as alternative sensitizers to promote the visible-light absorption of photocatalysts. Some studies have demonstrated that Au- and Ag-containing photocatalysts could work for photocatalytic reduction of CO₂ to C₁ and C₂₊ compounds.^{86,87,97-101} Cronin and co-workers prepared a Au/TiO₂ photocatalyst, and found that the wavelength of light source could significantly affect the activity and selectivity of the catalyst (Fig. 9a).⁸⁶ Under 532 nm-light irradiation, only Au nanoparticles could be excited because of the SPR effect. Au/TiO₂ has remarkably higher activity than TiO₂ and Au alone, and CH₄ was the only product. Under irradiation of 365 nm light, only TiO₂ could be excited, and the products over TiO₂ and Au/TiO₂ were CH₄. Under 254 nm-light irradiation, the photon energy is high enough to excite d band electronic transition in Au nanoparticle. Besides CH₄, C₂H₆, CH₃OH and HCHO were formed over Au/TiO₂ and Au nanoparticles. However, over TiO₂, only CH₄ was produced, indicating that C₂H₆, CH₃OH and HCHO were formed on Au nanoparticle surfaces. Several other studies also reported the formation of C₂₊ products during photocatalytic reduction of CO₂ using plasmonic Au nanoparticles-based catalysts. For example, a structured montmorillonite (MMT)-dispersed Au/TiO₂ catalyst was claimed to catalyse the reduction of CO₂ by H₂ under not only UV-visible but also simulated sunlight irradiation, offering CO, CH₄ and C₂H₆.⁹⁷ The LSPR effect of Au

nanoarticles significantly enhanced the formation of CO and hydrocarbons. The formation rates of CO, CH₄ and C₂H₆ were 199, 199, and 2.1 μmol g⁻¹ h⁻¹ under simulated one-sun irradiation at 100 °C.

The alloying effect such as the loading of Au-Cu or Au-Pd alloy onto a semiconductor could further accelerate the photocatalytic reduction of CO₂.^{98,99} For example, Kuang and co-workers found that the Au nanoparticles loaded on {101} facets of well-defined truncated bipyramidal TiO₂ nanocrystals offered mainly CO during the photocatalytic reduction of CO₂ with H₂O vapour.⁹⁹ The use of Au-Pd alloy instead of Au significantly decreased the selectivity of CO and increased that of hydrocarbons. Over the Au₆Pd₁/TiO₂ {101} catalyst, the selectivities of CH₄ and C₂ hydrocarbons (C₂H₆ and C₂H₄) were 71% and 14%, respectively. It was argued that selectivity depended on the synergistic functions of several parameters including: (i) the LSPR effect of Au, (ii) the hydrogenation performance of Pd and (iii) the adsorption-desorption behaviour of the reaction intermediate (CO_{ads}) on the Au and Pd sites.⁹⁹ These parameters enable the optimisation of activity and selectivity by tuning the elemental composition of the alloy co-catalyst.

Jain and co-workers reported the use of semiconductor- or support-free colloidal Au nanoparticles with diameters of ~12 nm and a characteristic LSPR band centred at 520 nm for photocatalytic reduction of CO₂ under visible-light irradiation in aqueous solution.¹⁰⁰ In the presence of isopropanol, which acted as a sacrificial reagent to scavenge holes, the reduction of CO₂ by the photo-excited electrons generated on the oxide- or support-free Au nanoparticles could offer CH₄ and C₂H₆ as major products. The formation rates of CH₄ and C₂H₆ were 0.68 and 0.56 NP(nanoparticle)⁻¹ h⁻¹. Both the photon energy and the light intensity play crucial roles in C-C coupling. No C₂H₆ was observed using 532 nm-light irradiation, and under 488 nm-light irradiation, there existed an onset of C₂H₆ generation at a light intensity of 300 mW cm⁻², above which the formation rate of C₂H₆ increased with an increase in light intensity.¹⁰⁰ CO₂•⁻ or its hydrogenated form is proposed to be the intermediate, which undergoes a series of hot-electron- and proton-transfer steps to form products. The C-C coupling was proposed to occur between the two CO₂•⁻ pair. The occurrence of C-C coupling requires simultaneous harvesting of two electrons, and thus higher rate of hot electron transfer and higher light intensity.

Considering that an ionic liquid, i.e., 1-ethyl-3-methylimidazolium tetra-fluoroborate (EMIM-BF₄) could stabilise the high-energy CO₂•⁻ intermediate, Yu and Jain further adopted aqueous solution for photocatalytic reduction of CO₂ using the plasmonic Au nanoparticle under green light (532 nm) irradiation.⁸⁷ As shown in Fig. 9b, the activity and selectivity of CO₂ reduction depended on the concentration of EMIM-BF₄.⁸⁷ The activity was very low in pure water or EMIM-BF₄. The presence of EMIM-BF₄ in water significantly accelerated the photocatalytic reduction of CO₂ and the highest activity was found in 5 mol% EMIM-BF₄ solution. Besides CH₄, C₂ (C₂H₄ and C₂H₂) and C₃ (C₃H₈ and C₃H₆) were also formed with considerable amounts. The EMIM-BF₄ concentration affected the selectivity of C-C coupling products. The selectivity of C₂₊ hydrocarbons was ~50% in 1-10 mol% EMIM-BF₄ solutions, and it decreased to ~20% in 25 mol% EMIM-BF₄ solution. The ¹³C isotope labelling experiment and the fluorogenic test confirmed that the hydrocarbons were generated from CO₂ and that the

REVIEW

Energy & Environmental Science

photogenerated holes oxidized H₂O to H₂O₂ instead of O₂. The studies further showed that EMIM-BF₄⁻ enhanced the activation of CO₂ and promoted the electron transfer from Au nanoparticle to CO₂, thus improving the performance for CO₂ reduction. Moreover, the CO₂•⁻ intermediate formed at the Au nanoparticle/solution interface may be stabilized due to the complexation by EMIM⁺ ([EMIM⁺-CO₂]) and the higher concentration of the activated [EMIM⁺-CO₂] complex would lead to higher probability of C-C coupling. The drops in activity and selectivity at higher EMIM-BF₄⁻ concentrations might arise from that the adsorption of BF₄⁻ on Au nanoparticles inhibited the adsorption of CO₂ and the transfer of electrons to CO₂.

3.1.5. Mechanism for C-C coupling in photocatalytic reduction of CO₂ to C₂₊ compounds. The mechanism for photocatalytic reduction of CO₂ to C₂₊ compounds, which involves CO₂ activation and multi-electron/multi-proton transfer, is quite complicated. The addition of the first electron to activate a free CO₂ molecule is difficult, because the potential for reduction of CO₂ to anion radical CO₂•⁻ is highly negative (-1.4 V vs NHE, pH = 0).¹⁰² The surface adsorption of CO₂ can lower the barrier for accepting electron by changing the geometry of CO₂ molecule.^{103,104} Take the most widely studied TiO₂ as an example. The possible surface structures of adsorbed CO₂ on TiO₂ surfaces are displayed in Fig. 10a.¹⁰⁵ These structures can be grouped into: (i) CO₂ with linear structure (L) and bent structure (B); (ii) monodentate carbonates (MC) that include a carbonate coordinated to a surface Ti centre and a carbonate with one of the oxygen fixed at the lattice position; (iii) bidentate carbonates (BC) that include bridging BC bound to two adjacent Ti centres and chelating BC bound to a single Ti centre; (iv) monodentate and bidentate bicarbonates (MB and BB) derived from the corresponding carbonate structures. The activation of CO₂ is strongly dependent on the adsorption structure of CO₂ on surfaces, which can lead to different reaction intermediates and pathways to different products. For instance, a bridging bidentate configuration of CO₂ favours the attachment of a hydrogen atom to the carbon atom, leading to the formation of a bidentate formate anion intermediate and the formation of HCOOH.¹⁰⁶

After CO₂ activation, a series of elementary steps may take place including the transfer of electrons and protons, formation of intermediates, the cleavage of C-O bond, and the creation of C-H and C-C bonds, resulting in C₂₊ products. Many studies have been devoted to studying the mechanism for CO₂ photocatalytic reduction, but the effort focusing on C-C coupling to C₂₊ compounds is limited. Most studies reported to date have proposed that the adsorbed CO₂ first accepts an electron to form surface CO₂•⁻. Several possible routes have been proposed for the subsequent conversion of CO₂•⁻ and C-C coupling. These routes include oxalic acid pathway, glyoxal pathway and methyl radical pathway (Fig. 10b). In the oxalic acid pathway, the C-C coupling is proposed to occur between the CO₂•⁻ pair to oxalate (C₂O₄²⁻), and oxalic acid is a primary C₂ product, which can further be reduced to other C₂₊ compounds.^{59,100,107,108} Eggin and co-workers found the formation of C₂O₄²⁻ as the major product together with glyoxylate, glycolate and tartrate during the photocatalytic reduction of CO₂ on ZnS in the present of

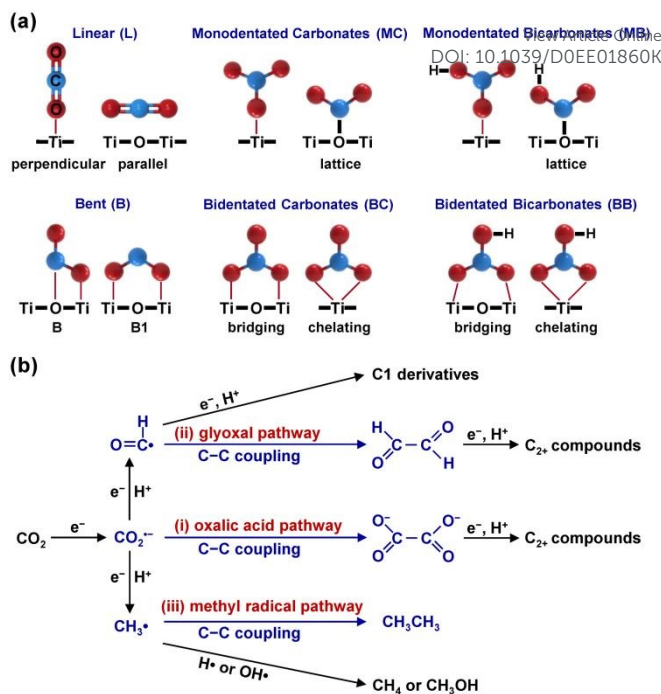


Fig. 10 (a) Possible adsorption structures of CO₂ on TiO₂ surfaces.¹⁰⁶ (b) Proposed mechanisms for photocatalytic CO₂ reduction involving C-C coupling.

tetramethylammonium chloride, providing evidence for oxalic acid pathway.^{107,108} In the glyoxal pathway, CO₂•⁻ is converted to formyl radical (•CHO), which can not only be reduced to C₁ derivatives but can also be dimerized into glyoxal, followed by further reduction to other C₂₊ compounds. Shkrob and co-workers investigated the intermediates on TiO₂ for CO₂ photocatalytic reduction by ESR spectroscopy and the result suggested that •CHO is the intermediate of glyoxal.¹⁰⁹ Glyoxal can be reduced to glycolaldehyde and acetaldehyde, which may undergo oxidation and decarbonylation to CH₃•, the intermediate of CH₄ or C₂H₆. CH₃• radicals may also be generated through other paths,^{45,104} and the formation of CH₃• has been confirmed through the ESR characterization.⁶⁷ CH₃• has been proposed as the key intermediate for C-C coupling to form C₂H₆ in many studies, although it may also react with H⁺ or •OH to yield CH₄ or CH₃OH (Fig. 10b).

3.2. Photocatalytic conversion of CO

CO can be transformed into C₂₊ chemicals and fuels by thermocatalysis via hydrogenation.⁶⁻⁸ Fischer-Tropsch synthesis is the most intensively studied heterogeneous reaction for hydrogenation of CO to C₂₊ hydrocarbons, but the reaction should be performed at high temperatures and pressures, and suffers from the limited selectivity of a specific C₂₊ hydrocarbon.⁷ The most accepted scenario for C₂₊ formation on Fischer-Tropsch catalyst surfaces is schematically illustrated in Fig. 11. In brief, the adsorption and dissociation of CO and H₂ on catalyst surfaces lead to the generation of CH_x (x = 1-3) species, which undergo C-C coupling to form surface C_nH_m intermediates (n ≥ 2), followed by the dehydrogenation or hydrogenation to olefins or paraffins, respectively.⁷ The uncontrollable C-C coupling of CH_x species on Fischer-Tropsch

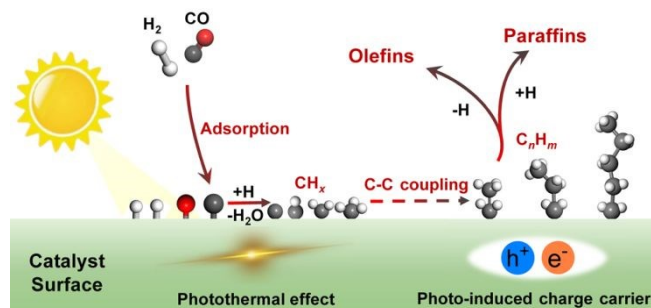


Fig. 11 Simplified reaction mechanism for photo-driven CO hydrogenation.

catalysts causes a wide distribution of hydrocarbon products.⁷ To develop novel methods or new catalytic systems with enhanced activity and selectivity for the transformation of syngas to C₂₊ products has drawn great research interests.⁶⁻⁸

Solar energy-driven hydrogenation of CO or Fischer-Tropsch synthesis has recently attracted research attention.⁴² The solar light can either trigger photo-thermal effect or induce free charge carriers on a catalyst, which may have potentials to enhance the adsorption/activation of CO and H₂ to increase the activity or to regulate the growth of C-C bonds and the termination of reactions to control the selectivity (Fig. 11). Co, Fe and Ru, which are typical Fischer-Tropsch catalysts owing to their balanced capacities for CO/H₂ activation and C-C coupling,⁷ have mainly been studied for the hydrogenation of CO under light irradiation (Table 2).¹¹⁰⁻¹¹⁵

Zhang and co-workers reported that under UV-vis-light irradiation without external heating, a Co-based catalyst, Co-Co₃O₄/ZnO-Al₂O₃, which was fabricated by H₂ reduction of ZnCoAl-layered double-hydroxide (LDH) nanosheets at 450 °C, showed a CO conversion of 15.4% and C₂-C₄ olefin selectivity of 36.0% (ratio of olefins to paraffins, 6.1).¹¹⁰ This Co-based catalyst was found to exhibit strong light adsorption ability across the UV-vis region, and the temperature of the catalyst bed could increase rapidly from 25 to 195 °C by irradiating the catalyst under UV-vis light irradiation without external heating. It is proposed that the solar-driven CO hydrogenation with the present Co catalyst involves photo-thermal

rather than photocatalytic pathway.¹¹⁰ Control experiments for thermocatalytic hydrogenation of CO at 195 °C without light irradiation showed a similar conversion of CO and distribution of hydrocarbon products, confirming that the photo-thermal effect contributed to the CO hydrogenation. The catalytic performance depended on the temperature adopted for H₂ reduction, and it was clarified that the co-existence of Co₃O₄ and Co played a crucial role in hydrogenation of CO to lower olefins. The oxide-decorated metallic Co nanoparticle heterostructure was proposed to weaken the hydrogenation capability of metallic Co, leading to formation of lower olefins over Co-based catalysts.

Using a similar strategy, Zhang and co-workers further fabricated a Fe-based catalyst, denoted as Fe-Fe₃O₄/ZnO-Al₂O₃, by H₂ reduction of ZnFeAl-LDH nanosheets at 500 °C for photo-thermal catalytic hydrogenation of CO.¹¹¹ This catalyst, which was composed of Fe⁰ and FeO_x nanoparticles, showed a CO conversion of 21% and C₂-C₄ olefin selectivity of 42% at a syngas pressure of 0.18 MPa under UV-vis irradiation without external heating. The reaction could also be performed under visible-light irradiation, offering a CO conversion of 11% and C₂-C₄ olefin selectivity of 41%. It is of interest that the selectivity towards CO₂ using this system is quite low (11% under UV-vis light irradiation) as compared with the traditional thermocatalysis. The heterostructure of Fe⁰ and FeO_x may also play a crucial role in the hydrogenation. The temperature of the catalyst bed for Fe-Fe₃O₄/ZnO-Al₂O₃ increased to 230 °C under UV-vis light irradiation. The control experiments with external heating and without light irradiation showed a lower CO conversion (9.9 %) compared to the light-driven hydrogenation of CO (21 %).¹¹¹ Furthermore, the selectivity of C₂-C₄ olefins was 37.2% under thermocatalytic reaction, lower than that obtained in solar-driven reaction, while the selectivity of CO₂ was 60.8%, much higher than that under light-driven CO hydrogenation (Fig. 12a). DFT calculations revealed that the catalyst was in excited state under light irradiation and had different ability for CO₂ formation and adsorption/hydrogenation of olefin compared to the ground state under thermocatalytic conditions (Fig. 12b). Thus, the Fe-based system may involve photocatalytic mechanism.

Table 2 Photocatalytic systems for the transformations of CO into C₂₊ chemicals

Catalyst	External heating (°C)	Light wavelength (nm)	CO conv. (%)	CO ₂ selectivity (%)	Selectivity without CO ₂ (%)				Ref.
					CH ₄	C ₂₋₄ =	C ₂₋₄ ⁰	C ₅₊	
Co-Co ₃ O ₄ /ZnO-Al ₂ O ₃	No	200-800	15.4	47.6	47.6	36.0	5.9	10.1	110
Fe-Fe ₃ O ₄ /ZnO-Al ₂ O ₃	No	200-800	20.9	11.4	28.6	42.4	9.0	8.6	111
Fe ₅ C ₂	No	200-1100	49.5	18.9	33.1	55.5	5.1	6.3	112
Ru/graphene	150	400-800	1.44	-	2.6	-	15.7	83.9	113
20% Co/TNT	220	UV	63.9	17.3	34.6	0.3	22.4	42.7	114
Ni-based catalyst	No	200-800	27.7	2.7	38.4	-	21.7	39.9	115
Ni-based catalyst	No	400-800	20.9	2.0	31.5	-	23.3	45.2	115

REVIEW

Energy & Environmental Science

Ma and co-workers further employed Fe_5C_2 for photo-thermal hydrogenation of CO at atmospheric pressure under UV-vis light irradiation in the absence of external heating.¹¹² The conversion of CO and the selectivity of $\text{C}_2\text{-}\text{C}_4$ olefins were 49.5% and 55.5%, respectively. This photo-thermal catalytic system was particularly favourable for the production of olefins and the ratio of $\text{C}_2\text{-}\text{C}_4$ olefins to paraffins reached 10.9. At the same time, the selectivity of CO_2 was 18.9%, relatively lower than that reported in the conventional FTO process. This performance is quite surprising because usually heavy modification of Fe_5C_2 is required to gain considerable selectivity of lower olefins in the conventional thermocatalytic reaction operated under a high pressure. Fe_5C_2 was found to exhibit a remarkable photo-thermal effect, which might result from excitation of the surface plasmon band and the consequential fast thermal relaxation of the excitation, and the catalyst bed could reach 490 °C under UV-vis-light irradiation. The control experiments for thermocatalytic hydrogenation of CO over Fe_5C_2 at 300–500 °C showed that the CO conversion was low at a low temperature, and upon raising the temperature gradually to 500 °C, CO conversion reached 80.5%, but CH_4 was the predominant product with a CO_2 selectivity of 36% and no $\text{C}_2\text{-}\text{C}_4$ olefins were formed (Fig. 12a).¹¹² It was clarified that the Fe_5C_2 surface was oxidized to oxides at the high temperature under traditional thermal catalytic reaction conditions. On the other hand, the characterisations indicated that the surface of the Fe_5C_2 catalyst was partially decorated by O atoms under light irradiation. The DFT calculations further revealed that O-decorated Fe_5C_2 surface could accelerate the desorption of olefin molecules, thus increasing the selectivity of $\text{C}_2\text{-}\text{C}_4$ olefins.

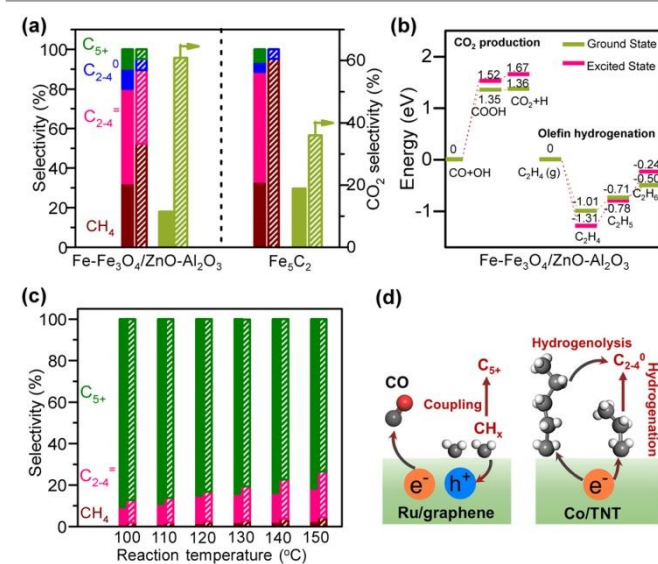


Fig. 12 (a) Product distributions in photo-driven CO hydrogenation over $\text{Fe}-\text{Fe}_3\text{O}_4/\text{ZnO}-\text{Al}_2\text{O}_3$ and Fe_5C_2 . The filled bars are for the reaction performed under light irradiation, while the bars with slashes are for the reaction without light irradiation but with external heating.^{111,112} (b) The potential energy profile for CO_2 production and olefin hydrogenation over ground-state and excited-state $\text{Fe}-\text{Fe}_3\text{O}_4/\text{ZnO}-\text{Al}_2\text{O}_3$.¹¹¹ (c) Distributions of hydrocarbon products over Ru/graphene with or without light irradiation at different temperatures. The filled bars and bars with slashes are for the reactions performed under light irradiation and without light irradiation, respectively.¹¹³ (d) Proposed roles of photogenerated electrons in tuning the selectivity of photo-driven CO hydrogenation over Ru/graphene and Co/TNT.^{113,114}

Photo-irradiation of a Ru/graphene catalyst was found to accelerate the hydrogenation of CO to C_{5+} hydrocarbons.¹¹³ The nanostructured worm-like Ru dispersed on graphene sheets could catalyse the hydrogenation of CO under visible-light irradiation under relatively mild reaction conditions (150 °C, 2.0 MPa CO and 1.0 MPa H₂), and catalytic activity reached 14.4 mol_{CO} mol_{Ru}⁻¹ h⁻¹, significantly higher than that in the absence of photo-irradiation (7.8 mol_{CO} mol_{Ru}⁻¹ h⁻¹).¹¹³ The reaction rate was found to be dependent on the light intensity or the light wavelength, confirming that light irradiation played a key role in the enhancement of CO conversion activity. Furthermore, at the same temperature, the selectivity of the C_{5+} hydrocarbons was higher under irradiation than that without irradiation (Fig. 12c). It was claimed that the enhancement in CO conversion to C_{5+} hydrocarbons mainly resulted from the light-excited hot electrons in Ru nanoparticles. The injecting of photo-excited hot electrons into the $2\pi^*$ orbital of CO molecules can accelerate the activation of CO molecules, thus increasing the rate of CO dissociation. Further, it is speculated that the excited electrons under light irradiation may increase the unsaturation of the d-band of Ru metal, which results in the donation of electrons from surface CH_x species to the metal centre and decreases the Pauli repulsion between the CH_x species and C_nH_m intermediates (Fig. 12d).¹¹³ The decrease in the Pauli repulsion may increase the chance of chain growth, resulting in the high selectivity of C_{5+} product.

TiO₂ nanotube (TNT)-supported Co catalysts were examined for the hydrogenation of CO under UV-light illumination at 220 °C and syngas pressure of 2.0 MPa.¹¹⁴ Under such conditions, the thermocatalytic conversion of syngas could also occur, but the UV-light illumination was found to enhance the CO conversion. For example, the CO conversion was increased from 9.2% to 64%, while the C_{5+} selectivity was kept at 42–43%, when 20 wt% Co/TNT was illuminated under UV light.¹¹⁴ The selectivity of CH_4 was enhanced from 25% to 35% and the ratio of $\text{C}_2\text{-}\text{C}_4$ olefins to paraffins decreased from 11 to 1.4 at the same time. It was speculated that the transfer of photogenerated electrons from TNTs to Co sites might occur, thus promoting the adsorption and activation of CO molecules to enhance activity and inducing the hydrogenation of olefin to paraffins or hydrogenolysis of heavier hydrocarbons to shorter-chain paraffins (Fig. 12d).¹¹⁴

Ni-based catalysts showed an unexpected activity in the hydrogenation of CO to C_{2+} hydrocarbons under photo-irradiation without external heating. The traditional thermocatalytic conversion of syngas usually leads to the formation of CH_4 . Zhang, Ma and their co-workers found that the irradiation of a Ni-based catalyst, which was synthesized by H₂ reduction of NiAl-LDH nanosheets at 525 °C, under UV-vis illumination could convert syngas (0.8 MPa, H₂/CO = 3/1) into $\text{C}_2\text{-}\text{C}_7$ hydrocarbons with a selectivity of 60% at a CO conversion of 27.7%.¹¹⁵ The temperature of the catalyst bed increased to 150 °C under UV-vis illumination. The control experiment carried out at 150 °C without photo-irradiation only afford a CO conversion of 6% with CO_2 as a predominant product. The catalyst could also work for the formation of $\text{C}_2\text{-}\text{C}_7$ hydrocarbons under visible-light ($\lambda \geq 400$ nm) irradiation; the selectivity of $\text{C}_2\text{-}\text{C}_7$ hydrocarbons was 67% at a CO conversion of 21%. Under visible-light illumination, the temperature of the

catalyst bed only rose to around 81 °C. It is proposed that the CO hydrogenation to C₂₊ hydrocarbons is photo-activated rather than a photo-thermal process. The characterisation suggested that the catalyst was composed of Ni and NiO_x. The DFT calculations indicated that the modification of metallic Ni by surface oxides changed the reaction path of the surface CH_x species by increasing the barrier for CH₄ formation and decreasing that for C–C coupling.¹¹⁵ This is similar to the phenomena observed for the Co- and Fe-based catalysts,^{110–112} forming a concept that the oxide-decorated surfaces modulate the product selectivity in these photo-enhanced CO hydrogenation systems.

Photo-driven Fischer-Tropsch reaction enables the production of C₂₊ hydrocarbons through hydrogenation of CO in the absence of external heat source. Photo-thermal effect induces temperature increment at the catalyst bed, thus providing energy required for CO/H₂ activation and C–C coupling. Photo-excited charge carriers may modify the oxidation state and electronic structure of the active site on catalyst surfaces, thus regulating the product selectivity and making the product distribution different from that in thermocatalysis. High yields of C₂–C₄ olefins have been obtained over oxide-decorated Co- and Fe-based catalysts under light irradiation.^{110–112} Decoration with corresponding oxides can change the hydrogenation ability of the metal centre^{110,111} or accelerate the desorption of olefins from the surface,¹¹² thus contributing to the high selectivity of lower olefins. C₅₊ hydrocarbons could be formed as major products using Ru/graphene¹¹³ or Co/TNT¹¹⁴. Photo-generated electrons have been proposed to play a key role in the activation of CO/H₂ and the favourable production of these C₅₊ paraffins. A Ni-based catalyst, which usually catalyses the formation of CH₄ in thermocatalysis, has shown an unexpectedly high selectivity of C₂–C₇ hydrocarbons in the photo-driven hydrogenation of CO.¹¹⁵ The modification of Ni by NiO_x is proposed to contribute to the selectivity switching by changing the energy barriers for CH₄ formation and C–C coupling.

4. Electrocatalytic conversions of CO₂ and CO

Electrocatalytic conversions of CO₂ and CO to C₂₊ products such as olefins and alcohols have become one of the most promising routes to utilize the abundant CO₂ and CO feedstocks under ambient conditions, owing to recent progress in generating electricity from renewable energy sources, such as solar, wind and hydropower.^{40,116–118} An analysis comparing the electrocatalytic, biocatalytic and fossil fuel-derived chemical-production routes has shown that the electrocatalytic route has a great potential to yield the greatest reduction in CO₂ emission, provided that a steady supply of clean electricity is available.⁴⁰ Different from photocatalytic reactions, in which the reduction and oxidation reactions usually take place in the same cell, the electrocatalytic reaction typically separates reduction and oxidation half reactions into two cells, and thus is capable of avoiding the re-oxidation of reduction products. The activity and selectivity of electrocatalytic reactions can be modulated and optimised by regulating the applied potential. Furthermore, the use

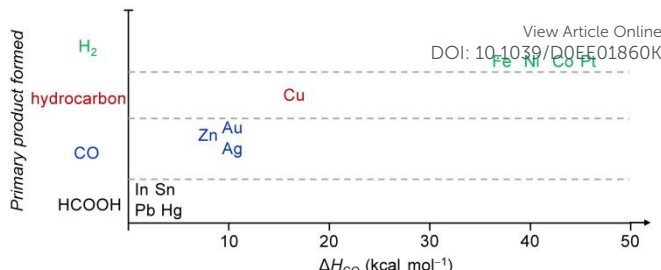


Fig. 13 General relationship between the primary product formed and ΔH_{CO} over different metals for electrocatalytic CO₂RR.¹²² Reproduced from ref. 122, with permission of Wiley-VCH Verlag GmbH&Co. KGaA, copyright 2017.

of gas diffusion electrode in a flow cell has technically pushed the current densities to industrially relevant levels ($> 200 \text{ mA cm}^{-2}$).^{119–121} Thus, electrocatalytic reductions of CO₂ and CO into high-value C₂₊ compounds have become a very promising and appealing research area in chemistry.

Metal catalysts have been typically employed in electrocatalytic CO₂ reduction reaction (CO₂RR) with high activity and selectivity. It is generally accepted that the metal-CO binding strength, expressed by ΔH_{CO} , plays an important role in determining the selectivity of a metal catalyst for electrocatalytic CO₂RR (Fig. 13).^{122,123} This is known as the Sabatier principle in electrocatalytic CO₂RR.¹²³ In brief, metals with too weak CO binding energy, such as In, Sn, Pb and Hg, tend to be beneficial to the formation of formate,^{116,123,124,125} while those with relatively weak CO binding energy, such as Zn, Au, and Ag, offer CO as the main product.^{116,122,126} The metals with too strong CO adsorption (such as Fe, Ni, Co, and Pt) can cause the poisoning of electrocatalysts, and thus usually favours H₂ evolution.¹²⁶ In the single-metal electrocatalysts, only Cu with moderate CO binding energy is able to catalyse the formation of C₂₊ products with considerable efficiency.^{53,117,118,127}

For the synthesis of C₂₊ products, it is generally believed that CO is the key reaction intermediate in electrocatalytic CO₂RR.^{53,118,127,128} The study of electrocatalytic CO reduction reaction (CORR) would be beneficial to developing more efficient electrocatalysts for CO₂RR to C₂₊ products and understanding the C–C coupling mechanism.^{127,128} Further, because better selectivity to C₂₊ products and improved stability may be expected for electrocatalytic CORR than for direct CO₂RR, electrocatalytic CORR would be useful for implementing a tandem strategy to synthesize C₂₊ products from CO₂ via CO.^{43,129,130} An analysis demonstrated that a two-step tandem electrocatalytic reactor, in which the first reactor converts CO₂ to CO or formate and second reactor converts CO or formate to C₂H₅OH or C₂H₄ may offer higher optimal solar-to-fuel conversion efficiencies.¹³¹

Here, we highlight recent advances in developing Cu-based catalysts for the synthesis of four C₂₊ products, i.e., ethylene, ethanol, acetate and *n*-propanol, by electrocatalytic CO₂RR and CORR. It is noteworthy that the synthesis of a single product is still very difficult. Therefore, we mainly review the studies that can offer one of these C₂₊ compounds as the major product. The electrocatalysts other than Cu that are capable of forming C₂₊ products are also briefly touched. The possible reaction mechanism will be discussed with an emphasis on C–C coupling.

REVIEW

Energy & Environmental Science

4.1. Electrocatalytic CO₂RR and CORR into ethylene over Cu-based catalysts

Ethylene is one of the most important building block in the current chemical industry for the production of a wide range of chemicals, in particular plastics.^{7,8} It is primarily produced by thermal cracking of crude oil-derived naphtha. C₂H₄ can be produced by hydrogenation of CO via direct Fischer-Tropsch synthesis, indirect route via methanol synthesis followed by methanol-to-olefins (MTO) or direct route via methanol intermediate using a bifunctional catalyst.^{7,8} However, the selectivity of C₂H₄ by these thermocatalysis routes is generally not high (< 50%) even though the selectivity of C₂-C₄ olefins has recently made a significant step-forward by using the bifunctional catalyst.^{27,28,132,133} The thermocatalytic hydrogenation of

CO₂ also suffers from lower selectivity of C₂H₄.⁸⁻¹⁵ CO₂RR or CORR with H₂O by electrocatalysis provides a promising avenue¹³⁴⁻¹³⁹ for synthesis of C₂H₄ as a major product under mild conditions. This section contributes to summarizing recent advances in Cu-catalysed CO₂RR and CORR to C₂H₄ with the aim to offer insights into the key factors controlling the CO₂ or CO conversion activity and Faradaic efficiency (FE) of C₂₊ compounds, in particular C₂H₄. The effects of different influencing factors such as the exposed facet, chemical state of surface Cu and dopant-modification of Cu catalysts are discussed. Some engineering factors such as cell configuration, electrolyte engineering and reaction conditions will also be analysed. Some typical results for electrocatalytic CO₂ and CORR are displayed in Tables 3 and 4.¹³⁴⁻¹⁷⁵

Table 3 Typical electrocatalytic systems for CO₂RR to C₂₊ compounds

Electrocatalyst	Cell	<i>E</i> (V) ^a	<i>j</i> (mA cm ⁻²)	FE (%)					Ref.
				Ethylene	Acetate	Ethanol	propanol	C ₂₊	
Cu(100) nanocubes	H-cell	-0.96	-68	32	0	13	15.5	60.5	134
44 nm Cu cubes	H-cell	-1.1	-5.6	41.1	0.2	3.7	2.7	46.4	135
Plasma-activated Cu	H-cell	-0.9	-23	60	0	0	0	60	136
Cu ₂ O derived Cu	H-cell	-0.99	-25	40	0	8.7	0	48.7	137
Nano-defective Cu nanosheets	H-cell	-1.18	-60	83.2	0	0	0	83.2	138
B-doped Cu	H-cell	-1.1	-70	52	0	27	0	79	139
N-doped Cu	H-cell	-0.95	-22	39.3	0	18.4	6.0	63.7	140
Cu_I	H-cell	-0.90	-39	45	0.7	27	7.3	80	141
F-Cu	Alkaline GDE	-0.89	-1600	65	2	12	1	80	142
Thermally deposited Cu	Alkaline GDE	-0.67	-750	65	4	11	0	80	143
Cu-Al catalyst:ionomer bulk heterojunction	Alkaline GDE	-1.8	-600	80	~2	~13	~2	~97	144
Arypyridiniums-Cu	Neutral GDE	-0.83	-320	71.5	1.5	10.5	2.1	85.6	146
	MEA	-3.65 ^b	-120	60	-	-	-	60	
Mesoporous Cu	H-cell	-1.3	-14.3	2	46 (ethane)	-	-	48	147
Iodine-derived Cu	H-cell	-1.0	-20.5	0.8	4.0 (ethane)	1.9	-	6.7	148
Cu ₄ Zn	H-cell	-1.05	-8.2	10.7	0.96	29.1	4.4	45.16	149
Phase-blended Ag-Cu ₂ O	H-cell	-1.2	-3	9.5	5.6	34.15	0	49.25	150
Nanoporous CuAg-wire	Alkaline GDE	-0.7	-300	60	0	25	0	85	151
Ag _{0.14} /Cu _{0.86} alloy	Alkaline GDE	-0.67	-250	35	5	41	0	81	152
Cu ₂ S@Cu vacancy	Alkaline GDE	-0.92	-400	21.2	3.0	24.7	6.9	55.8	153
FeTPP[Cl]/Cu	Neutral GDE	-0.82	-300	39	2	41	3	85	154
Cu/N-doped carbon nanospike	H-cell	-1.2	-2	0	0	63	0	63	155
34%N-C/Cu	Alkaline GDE	-0.68	-300	37.5	2.3	52.3	1.4	93.5	156
N-C/Cu nanorods	Alkaline GDE	-0.9	-281	24	4	45	7.4	80.4	157
Cu single atom/C	H-cell	-0.7	-1.23	0	0	91	0	91	158
N-doped nanodiamond	H-cell	-1.0	-7	0	91	0	0	91	159
B- and N-co-doped nanodiamond	H-cell	-1.0	-0.5	0	0	93.2	0	93.2	160
Mesoporous N-doped carbon	H-cell	-0.56	-2	0	0	78	0	78	161
N-doped graphene quantum dots	Alkaline GDE	-0.75	-28	31	6	14	4	55	162

^aThe potential refers to RHE; ^bThe potential represents the full-cell potential (V).

Table 4 Typical electrocatalytic systems for CORR to C₂₊ compoundsView Article Online
DOI: 10.1039/D0EE01860K

Catalyst	Cell	E (V) ^a	j (mA cm ⁻²)	FE (%)				Ref.
				Ethylene	Acetate	Ethanol	propanol	
oxide-derived Cu	Alkaline GDE	-0.67	-700	41.8	13.9	26.7	8.3	90.7 163
oxide-derived Cu (5% CO/N ₂)	Alkaline GDE	-0.52	-120	72	-	-	-	72 164
oxide-derived Cu	H-cell	-0.3	-0.285	0.6	13.6	42.9	0	57.1 165
Cu/carbon nanotubes	H-cell	-0.3	-0.37	0	36	36	0	72 166
Cu nanowires	H-cell	-0.30	-0.22	0.66	14	50	0	65 167
Pd _{0.07} Cu	Alkaline GDE	-0.62	-700	37	14.9	33.2	6.3	91.4 168
Cu nanoflower	H-cell	-0.23	-0.21	0.39	23.76	15.38	59.32 (aldehyde)	99 169
Cu-Ag nanoflower	H-cell	-0.335	-0.61	1.2	1.8	2.6	70 (aldehyde)	75.6 170
Cu nanoparticles	MEA	-2.4 ^b	-144	35.2	30.4	3.6	1.8	71 171
Cu nanosheet	Alkaline GDE	-0.736	-200	16.3	48	2.4	2	68.7 172
Cu nanocavity	Alkaline GDE	-0.56	-37	21	7.8	12.5	21	62.3 173
Fragmented Cu	Alkaline GDE	-0.45	-50	20	7	13	20	60 174
Cu adparticle	Alkaline GDE	-0.44	-48	29.6	4.7	14.6	23	71.9 175

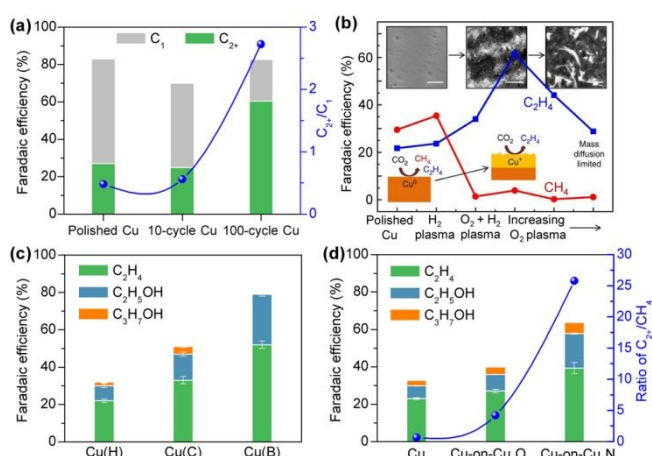
^aThe potential refers to RHE; ^bThe potential represents the full-cell potential (V).

Fig. 14 (a) Comparisons of C₂₊ FE and ratios of C₂₊/C₁ over different catalysts for electrocatalytic CO₂RR. 100-cycle Cu mainly with (100) facets exhibits a six-fold improvement as compared to the polished Cu foil primarily with (111) facets.¹³⁴ (b) C₂H₄ and CH₄ FE for plasma-treated Cu foils. From left to right, the insets show SEM images of the low surface area H₂ plasma-treated metallic Cu foil, the O₂ 20 W 2 min plasma-treated Cu foil with optimised C₂H₄ selectivity, and the high surface area nanoneedles on the O₂ 100 W 10 min oxidized sample after the reaction. Scale bars: 500 nm.¹³⁶ Reproduced from ref. 136 with the permissions of Springer-Nature, copyright 2016. (c) Comparison of C₂₊ FE on Cu(H), Cu(C) and Cu(B).¹³⁹ (d) Comparisons of C₂₊ FE and ratios of C₂₊/CH₄ on Cu, Cu-on-Cu₂O and Cu-on-Cu₃N.¹⁴⁰

The control of the exposed facet of a Cu catalyst may modulate its electrocatalytic performance, because different crystalline facets have different surface atomic arrangements and electronic structures, and may have different abilities to adsorb and activate the reactants and intermediates. Model studies using Cu single crystals showed that the product selectivity in electrocatalytic

reduction of CO₂ or CO depended strongly on the facet.¹⁷⁶⁻¹⁷⁸ Two early studies by Hori et al. showed that the electrocatalytic reduction of CO₂ in 0.1 M KHCO₃ aqueous solution using Cu(111) and Cu(100) yielded CH₄ and C₂H₄ as the major products, respectively.^{176,177} The introduction of (111) or (110) step atoms to (100) basal plane could significantly enhance the formation of C₂H₄. The Cu(110) facet favoured the formation of C₂₊ oxygenates such as CH₃COOH, CH₃CHO and C₂H₅OH.¹⁷⁷ Koper and co-workers found a similar trend in the electrocatalytic reduction of CO in aqueous solution over Cu single crystals with different facets; CH₄ was favoured on Cu(111), while C₂H₄ was favoured on Cu(100).¹⁷⁸ The reduction of CO on Cu(110) exhibited a similar potential dependence to that on Cu(111), but more C₂H₅OH was observed.¹⁷⁸ A study on electrocatalytic CO₂RR over Cu thin films on single crystals by epitaxial growth with the physical vapour deposition technique demonstrated that the Cu(100) film and the Cu(751) film that has a heterogeneous kinked surface with (110) terrace were more active and selective for C–C coupling than Cu(111) film, but the Cu(751) film was more selective toward C₂₊ oxygenate formation.¹⁷⁹

Yeo and co-workers performed experimental and computational studies for electrocatalytic CO₂RR on Cu(100), Cu(111) and Cu(110) single-crystal surfaces.¹⁸⁰ It was found that the onset potentials for C₂H₄ and CO were very closely related and Cu(100) showed the earliest onset potentials for CO and C₂H₄ formation, whereas Cu(111) exhibited the latest onset potentials for CO and C₂H₄ formation. The DFT calculations suggested that Cu(100) had the lowest energy barrier for CO dimerization and the energy barrier could be further lowered by increasing the *CO coverage.¹⁸⁰ These results indicate the importance of Cu(100) surfaces and *CO coverage in CO₂RR to C₂H₄. Recently, Wang, Chan and their co-workers performed a detailed DFT calculation on the energetics of the initial C–C coupling steps on

REVIEW

Energy & Environmental Science

different Cu facets in CO₂ reduction.¹³⁴ The result suggested that relative to Cu(111) facet, the Cu(100) and stepped (211) facets were more favourable for CO dimerization, and thus were beneficial to the formation of C₂₊ products. They synthesized Cu nanocubes with preferentially exposed (100) facets through a metal ion battery cycling method and found that the 100-cycled Cu nanocubes exhibited a six-fold increase in the ratio of C₂₊ (mainly C₂H₄) to C1 products as compared to the pristine polycrystalline Cu foil primarily with (111) facet (Fig. 14a).¹³⁴ The FEs of C₂₊ products and C₂H₄ could reach 60% and 32%, respectively, over the 100-cycled Cu nanotubes, which were much higher than those over the pristine polycrystalline Cu foil.

A few studies reported the fabrication of Cu nanocubes by other techniques for electrocatalytic reduction of CO₂ to C₂H₄.^{135,181} For example, Buonsanti and co-workers fabricated cube-shaped Cu nanocrystals with three different sizes (edge lengths) of 24, 44 and 63 nm by a colloidal chemistry-based method and found that the cubes with 44 nm edge length showed the best performance for C₂H₄ formation.¹³⁵ The FE of C₂H₄ over the Cu cubes with 44 nm edge length was 41%, significantly higher than those over the smaller or bigger Cu cubes as well as Cu foil. H₂ evolution reaction was very serious over the smaller Cu cubes.

Many groups found that as compared to the pure metallic Cu catalyst, the oxide-derived Cu catalysts showed enhanced C₂₊ selectivity.^{136-138,182-188} This may result from the differences in surface structures and local environments such as the density of defects, roughness factors, chemical states and oxygen modifiers. Cuenya and co-workers fabricated an oxide-derived Cu catalyst by treating Cu foil with O₂ plasma for electrocatalytic CO₂RR.¹³⁶ After O₂-plasma treatment of Cu foil, the formation of C₂H₄ was significantly enhanced, while the formation of CH₄ was suppressed. The FE of C₂H₄ reached 60% at -0.9 V versus reversible hydrogen electrode (RHE) for the Cu catalyst with 20 W-2 min O₂ plasma-treatment (Fig. 14b). On the other hand, the changes in the FEs of CH₄ and C₂H₄ were limited with H₂-plasma treatment (Fig. 14b). The O₂-plasma treatment could increase both the roughness factor and the surface Cu⁺ sites. It was found that when the O₂ plasma-activated Cu foil was further subjected to H₂-plasma treatment, the FE of C₂H₄ decreased significantly despite similar roughness. The H₂-plasma treatment could deplete the Cu⁺ sites. Thus, it was argued that Cu⁺ species played a key role in enhancing the formation of C₂H₄ on the oxide-derived Cu catalysts.

Through theoretical calculations, Goddard III and co-workers proposed a unique electrocatalyst composed of Cu metal embedded in oxidised matrix for CO₂RR to C₂₊ products.¹⁸² It was shown that the fully oxidised catalyst model could not explain the enhanced electrocatalytic performance and such a catalyst was also unstable under CO₂RR conditions. Both Cu⁺ and Cu⁰ were proposed to contribute to CO₂RR to C₂₊ products and they worked synergistically to improve the kinetics and thermodynamics for both CO₂ activation and CO dimerization.¹⁸² It was proposed that in the initial step, the Cu⁺ site could bind H₂O molecules at the edge of Cu⁰ region and this H₂O on surface Cu⁺ may form strong hydrogen bonds to CO₂, stabilising both the transition state and the final state of CO₂ activation on nearby Cu⁰, facilitating the formation of CO (Fig. 15a). In the next step, the carbon atom of CO on Cu⁺ site may be positively charged (Mulliken charge, +0.11), whereas that on Cu⁰ site may be

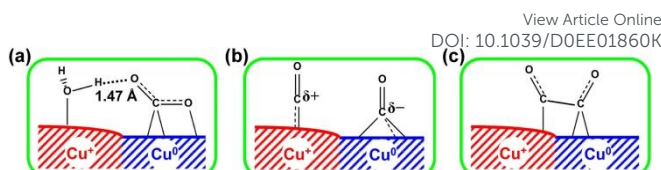


Fig. 15 Schematic illustration of the synergistic effects of Cu⁺ and Cu⁰.¹⁸² (a) CO₂ activation. (b) Chemical state of CO. (c) C–C coupling. Reproduced from ref. 182 with the permissions of National Academy of Sciences, copyright 2017.

negatively charged (Mulliken charge, -0.31) because of the back donation (Fig. 15b). The electrostatic attraction between the two carbon atoms would assist C–C coupling to form C₂₊ products (Fig. 15c). The theoretical calculation in combination with ambient-pressure X-ray photoelectron spectroscopy (XPS) studies by Goddard III and co-workers further pointed out the importance of the presence of a thin layer of suboxide below the metallic Cu surface in CO₂ sorption and activation.¹⁸³

The nature of active sites leading to high C₂₊ FE over oxide-derived Cu catalysts is still under debate. *In situ* ambient-pressure XPS and quasi *in situ* electron energy loss spectroscopy (EELS) studies showed no residual copper oxide over the oxide-derived Cu catalysts in electrocatalytic CO₂RR, but subsurface oxygen species may exist after oxidation-reduction cycles.¹⁸⁴ The subsurface oxygen species may increase the CO binding energy and contribute to enhance C–C coupling owing to the increased CO coverage on catalyst surfaces. It is noteworthy that the reduced oxide-derived Cu catalysts could be re-oxidised rapidly in air or H₂O environments, making the *ex situ* characterisations to determine the true chemical state of Cu under CO₂RR conditions highly challenging. Lum and Ager prepared an ¹⁸O-enriched oxide-derived Cu catalyst by oxidation/reduction cycling in H₂¹⁸O and the residual ¹⁸O in the Cu catalyst after the electrocatalytic CO₂RR was measured by secondary-ion mass spectrometry (SIMS).¹⁸⁵ The result showed that only a small fraction (< 1%) of original ¹⁸O was sustained after CO₂RR, whereas the catalyst maintained a high FE (~60%) towards C₂ and C₃ products.¹⁸⁵ Ager and co-workers further studied the possible active sites of a series of Cu₂O samples with different morphologies for electrocatalytic CO₂RR by *in situ* Raman in combination with real-time selected-ion flow tube mass spectrometry.¹⁸⁶ The result showed that the reduction of Cu₂O is kinetically and energetically more favourable than the CO₂RR, thus excluding the possibility of Cu₂O as active sites for the electrocatalytic CO₂RR.¹⁸⁶ Although further *operando* spectroscopy studies are needed, it is generally believed that the Cu^{δ+} sites on catalyst surfaces play pivotal roles in the formation of C₂₊ products.

Xu, Jiao and co-workers recently demonstrated that oxygen-containing surface species are unlikely involved in facilitating the formation of C₂₊ oxygenates in CORR.¹⁸⁹ By using *in situ* surface-enhanced Raman spectroscopy, they showed that oxygen-containing species do exist under the CORR conditions in an alkaline electrolyte for four commonly used Cu surfaces, i.e., Cu foil, Cu micro/nanoparticles, electrochemically deposited Cu film and oxide-derived Cu. The relative abundance of surface CuO_x on Cu foils is higher than that on other catalysts, while the opposite is true for the surface CuO_x/(OH)_y species. The surface speciation on different catalysts has been correlated with initial degree of oxidation of the

Cu surfaces prior to the exposure to negative potentials. However, the CORR experiments showed different trends in product selectivity. Thus, they concluded that the oxygen-containing surface species might not be the active species in the formation of C₂₊ oxygenates.¹⁸⁹

The doping of a heteroatom can modify the structure, the electronic and chemical properties of Cu catalysts, and thus plays an important role in governing the activity and selectivity for electrocatalytic CO₂RR by influencing the adsorption and activation of reactants and intermediates. Boron- and nitrogen-doped Cu catalysts have been found to show significantly improved performance for electrocatalytic CO₂RR to C₂H₄.^{139,140,190} On the other hand, the doping of chalcogen (such as sulfur, selenium and tellurium) has been reported to improve the formation of formate.^{191–193} For example, Sargent and co-workers synthesized a boron-doped Cu (Cu(B)) catalyst by reducing CuCl₂ with NaBH₄.¹³⁹ Two reference samples, Cu(C), which consisted of oxidized nanocopper, and Cu(H) that synthesized by using hydrazine hydrate as the reducing reagent were also prepared. The FE of C₂H₄ over Cu(B) reached 52% at -1.1 V versus RHE, which was 1.6 and 2.4 times higher than those of Cu(C) and Cu(H), respectively (Fig. 14c). The FE of total C₂ products (mainly C₂H₄ and C₂H₅OH) reached 79% with a current density of 70 mA cm⁻² under the same conditions over the Cu(B) catalyst, which was also much better than those over the Cu(H) and Cu(C) catalysts. The DFT calculation and characterisation results revealed that boron was located at the subsurface of catalyst. *In situ* X-ray absorption near-edge spectroscopy (XANES) studies indicated that the average oxidation state of Cu was between 0 and +1, and the slightly positive oxidation state of Cu was stable during the electrocatalytic CO₂RR. The electrocatalytic CO₂RR performance of the Cu(B) catalyst kept stable in 40 h of continuous operation, which was much better than other oxide-derived Cu catalysts.¹³⁹ Han and co-workers also reported the superior performance of a B-doped oxide-derived Cu catalyst, which was prepared by reduction of B₂O₃–Cu(OH)₂ film, for electrocatalytic CO₂RR.¹⁹⁰ An FE toward total C₂₊ products (C₂H₄, C₂H₆ and C₂H₅OH) of 48% was achieved at a current density of 33.4 mA cm⁻² at -1.05 V vs. RHE over the B-doped catalyst, better than that over the oxide-derived Cu catalyst without B (FE of C₂ products was 30.5% with a slightly lower current density at -1.05 V).¹⁹⁰ The XPS studies indicated that the doping of boron could stabilise a larger fraction of Cu⁺ on Cu surfaces.

The group of Sargent further synthesized Cu deposited on Cu₃N (Cu-on-Cu₃N) catalyst, which achieved a 6.3-fold enhancement in the ratio of C₂₊ to CH₄ as compared to Cu deposited on Cu₂O (Cu-on-Cu₂O) catalyst and a 40-fold enhancement relative to pure Cu catalyst (Fig. 14d).¹⁴⁰ The highest FE towards total C₂₊ products over the Cu-on-Cu₃N catalyst reached 64% at -0.95 V vs. RHE, with the FEs of C₂H₄, C₂H₅OH and C₃H₇OH being 39%, 19% and 6%, respectively. The Cu-on-Cu₃N catalyst also showed a better stability than the Cu-on-Cu₂O and Cu catalysts. The characterisations by XPS and *in situ* XANES suggested that Cu₃N could stabilise Cu⁺ to a larger extent as compared to Cu₂O during CO₂RR. DFT calculations further indicated that the modulated partial oxidation state by nitride enabled Cu-on-Cu₃N to achieve the lowest CO dimerization barrier energy. Therefore, both the boron and nitride modification contribute to stabilising Cu⁺ sites during electrocatalytic CO₂RR, which likely play

crucial roles in CO adsorption and dimerization to form C₂₊ products.^{139,140,190}

[View Article Online](#)

DOI: 10.1039/D0EE01860K

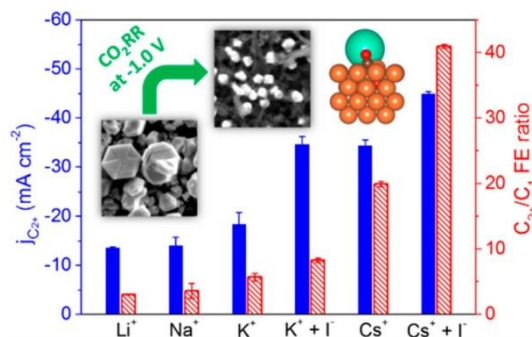


Fig. 16 Effects of cations and anions added in the electrolyte on CO₂RR.¹⁹⁶ Reproduced from ref. 196 with the permissions of American Chemical Society, copyright 2018.

A few groups reported that the modification of Cu by sulphur and other chalcogen modifiers enhanced the formation of formate during electrocatalytic CO₂RR.^{191–193} For example, Pérez-Ramírez, López and co-workers found that the FE of formate increased markedly from 26% to 78% after doping of sulfur on Cu surfaces at -0.8 V versus RHE.¹⁹³ It was proposed that the chalcogen modifier on Cu surfaces actively participated in the CO₂RR either by tethering CO₂ or transferring a hydride, thus suppressed the formation of CO and C₂₊ products. The different behaviours of heteroatoms doped on Cu catalysts reveal diversified functioning mechanisms of heteroatoms and offer us opportunities to explore more heteroatom dopants to narrow product distribution for electrocatalytic CO₂RR.

Cuenya and co-workers reported that the addition of a halide ion into KHCO₃ electrolyte could enhance the electrocatalytic CO₂RR into C₂₊ products over a plasma-oxidised polycrystalline Cu foil catalyst.¹⁹⁴ The CO₂ reduction rate was found to increase in the order of Cl⁻ < Br⁻ < I⁻, while the high FE of C₂₊ products kept almost unchanged. The enhancement in CO₂ reduction activity was proposed to arise from the adsorption of halide ions on Cu surfaces, which may facilitate the formation of carboxyl intermediate (*COOH), which was a precursor of CO, by partial charge donation from halide to CO₂. The effect of electrolytes on electrocatalytic CO₂RR over Cu(100) and Cu(111) surfaces was investigated by Yeo and co-workers.¹⁹⁵ They found that that the FEs of C₂H₄ and C₂H₅OH increased in the sequence of KClO₄ < KCl < KBr < KI over both Cu surfaces. The FE of total C₂₊ products reached 74% with those of C₂H₄ and C₂H₅OH being 50% and 16%, respectively, over Cu(100) surface in the case of KI. KI roughened the Cu surface but the increase in the roughness was not the major reason for the enhancement in performance. It was proposed that the increase in the population of adsorbed CO on Cu surfaces in the presence of KI might contribute to enhancing the formation of C₂₊ products. The effect of alkali metal cations in electrolyte was also examined for electrocatalytic CO₂RR in MHCO₃ (M = Li, Na, K, Cs) over O₂-plasma-activated Cu catalyst.¹⁹⁶ The increase in the size of alkali-metal cations increased the formation of C₂₊ products (mainly C₂H₄), and the co-existence of Cs⁺ and I⁻ further enhanced the partial current of C₂₊ compounds (Fig. 16). The highest FE of C₂₊ products reached ~69% with a C₂₊ partial current density of -45.5 mA cm⁻².

REVIEW

Energy & Environmental Science

Recently, the modification of Cu by halides has shown promising performances in CO₂RR to C₂₊ products.^{141,142} Cuenya and co-workers prepared halide-modified Cu (denoted as Cu_X, X = Cl, Br or I) catalysts by cycling electropolished Cu foils in 0.1 M KX solution and found that the Cu_I catalyst showed the best performance in electrocatalytic CO₂RR to C₂₊ products (mainly C₂H₄).¹⁴¹ The highest FE of C₂₊ product was ~80% with a partial current density of ~31.2 mA cm⁻² at -0.90 V vs. RHE. The nanostructure of Cu changed significantly for the Cu_I catalyst, and it was proposed that the enhancement in the formation of C₂₊ products arose from the reconstructed surface structures and adsorbed I⁻ species, which probably led to unique electronic and chemical effects to stabilise the subsurface oxygen and Cu⁺ species.

A recent work by our group demonstrated that a fluorine-modified Cu catalyst, which was fabricated by electroreduction of a Cu(OH)F precursor synthesized by a solvothermal method, showed excellent performance for electrocatalytic CO₂RR to C₂₊ products in a flow cell with a gas diffusion electrode (GDE).¹⁴² The FE of C₂₊ products (mainly C₂H₄ and C₂H₅OH) reached ~80% with an ultrahigh current density of 1.6 A cm⁻² at -0.89 V vs. RHE. The FE and formation rate of C₂H₄ reached 65% and ~3.2 mmol h⁻¹ cm⁻², much better than

those reported up to date. The carbon-based selectivity and single-pass yield of C₂₋₄ products (mainly C₂H₄ and C₂H₅OH) reached 85.8% and 16.5%, respectively, outperforming those achieved in high-temperature and high-pressure thermocatalysis.⁸ It was proposed that besides stabilising the Cu⁺ sites to enhance CO adsorption, the fluoride species on Cu surfaces facilitated the activation of H₂O and the hydrogenation of CO to CHO intermediate, which could undergo C-C coupling more facilely.¹⁴²

Most studies for electrocatalytic CO₂RR and CORR have typically been conducted in an H-cell. The limited CO₂ or CO solubility in water (33 mM for CO₂ and 1 mM for CO at 25 °C and 1 atm) usually leads to low reaction rates (< 100 mA cm⁻² for CO₂RR and < 10 mA cm⁻² for CORR), which are not viable for commercialisation, although the hydrophobic treatment can further enhance the CORR reaction rate in an H-cell.^{197,198} As already mentioned, the flow cell with GDE configuration enables the direct feeding of gaseous reactants to the electrode-electrolyte interface to circumvent the mass-transport limitation of CO₂ or CO, resulting in high reaction rates.¹¹⁹⁻¹²¹ The flow cells with different configurations (Fig. 17) have shown great potentials in electrocatalytic CO₂RR to C₂₊ products.^{142-146,199,200}

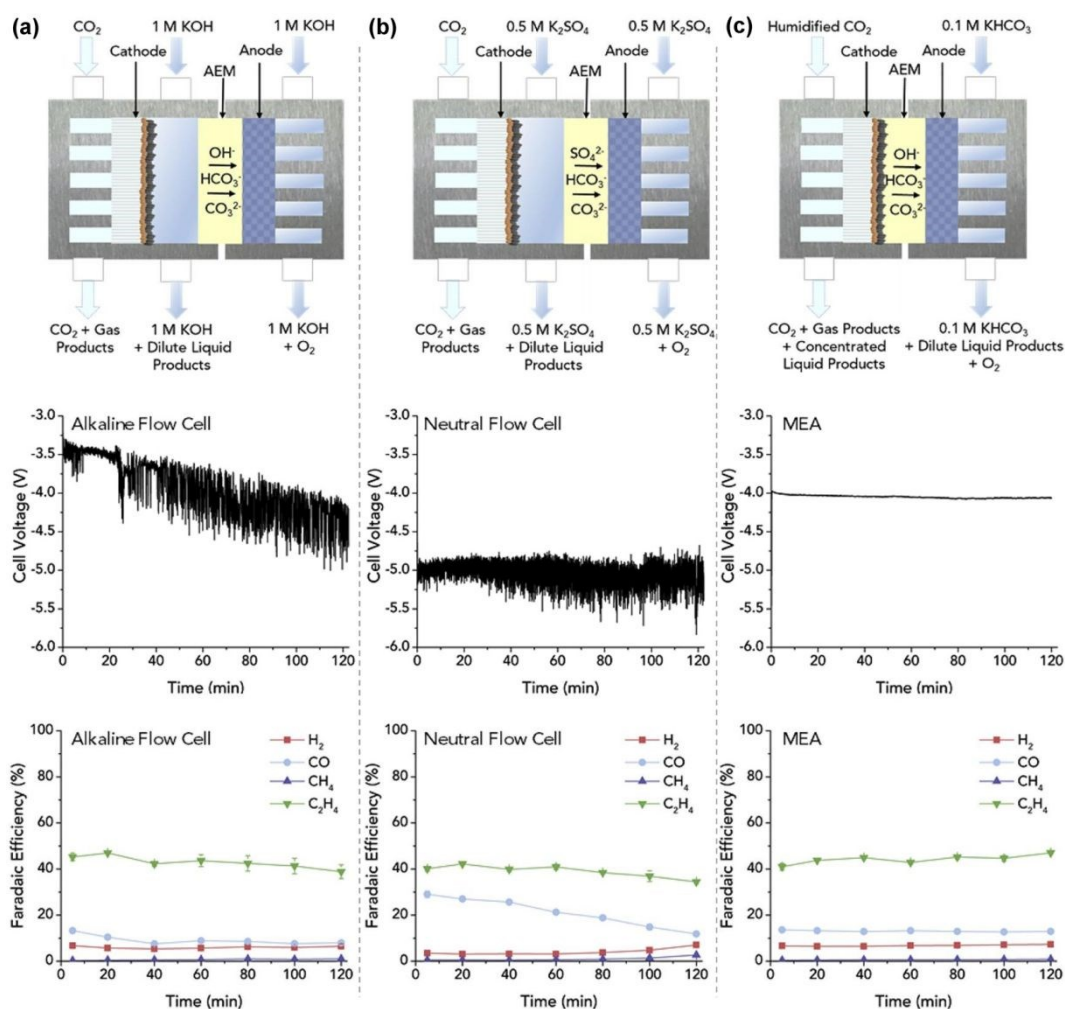


Fig. 17 Configurations of three types of flow cells, stability of the cell voltage and gas products for 120 min in different flow cells with an applied current density of 150 mA cm⁻².²⁰⁰
(a) Alkaline flow cell. (b) Neutral flow cell. (c) MEA flow cell. Reproduced from ref. 200, with permission of Elsevier, copyright 2019.

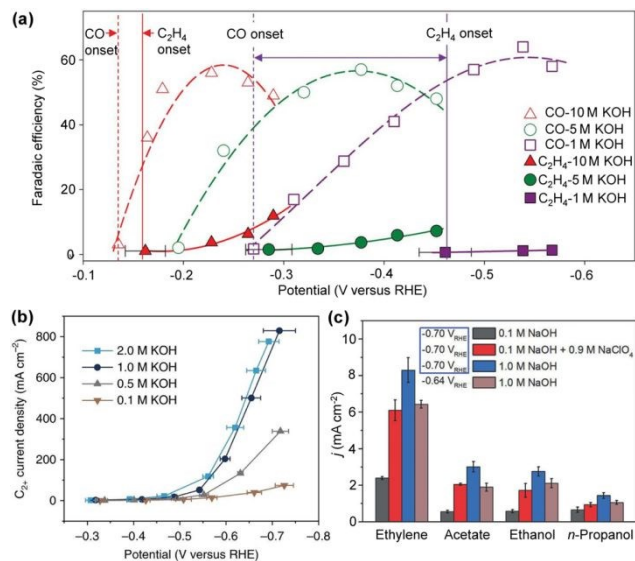


Fig. 18 (a) C_2H_4 and CO FE versus applied potential during CO_2 RR at different KOH concentrations.¹⁴³ (b) Partial current densities of C_{2+} products in CORR in KOH with different concentrations.¹⁶³ (c) Partial current densities of C_{2+} products in CORR in electrolytes with different Na^+ and OH^- concentrations.²⁰³ Reproduced from refs. 143, 163 and 203, with the permissions of American Association for the Advancement of Science, Springer-Nature and Wiley-VCH Verlag GmbH&Co. KGaA, copyright 2018 and 2020.

One significant merit of the flow cell is that it can be operated in a strong alkaline electrolyte (e.g., KOH) for CO_2 RR (Fig. 17a),²⁰⁰ whereas the use of strong alkaline electrolyte is restricted in the H-cell configuration because of the acidic nature of CO_2 molecule. The current consensus is that a high local pH can significantly promote the C–C coupling and suppress the formations of H_2 and methane.^{143,163,201,202} Thus, the alkaline flow cell particularly favours the formation of C_{2+} products, offering high FEs of C_{2+} compounds at impressively high current densities.^{142–146,202} For example, Sargent and co-workers reported that upon increasing the concentration of KOH from 1 to 10 M, the onset potential of C_2H_4 for CO_2 RR decreased to only -0.165 V versus RHE, close to the CO onset potential, whereas the onset potential of H_2 remained almost unchanged (Fig. 18a).¹⁴³ As such, a Cu catalyst with a thickness of 25 nm deposited on a carbon-based gas diffusion layer could achieve an C_2H_4 FE of 66% with a current density of 275 mA cm^{-2} at a potential of -0.54 V versus RHE in a 10 M KOH electrolyte. By further optimising the electrolyte to (3.5 M KOH + 5.0 M KI), the current density could increase to 750 mA cm^{-2} with C_2H_4 FE of 65% at -0.67 V versus RHE.

Very recently, a Cu-Al catalyst, which demonstrated further improved C_2H_4 selectivity in electrocatalytic CO_2 RR, was developed through machine learning-accelerated high-throughput DFT studies.¹⁴⁴ The de-alloyed nanoporous Cu-Al catalyst, which was fabricated by both thermal evaporation and co-sputtering followed by chemical etching, on carbon-based gas diffusion layer showed an FE of C_2H_4 as high as 80% at a current density of 600 mA cm^{-2} in 1 M KOH flow cell.

Similarly, by using the alkaline flow cell, Jiao and co-workers achieved excellent performances for electrocatalytic CORR to C_{2+}

compounds.¹⁶³ An oxide-derived Cu catalyst exhibited a C_{2+} FE of 91% and a C_{2+} partial current density of 635 mA cm^{-2} at a potential of -0.67 V versus RHE (Fig. 18b).¹⁶³ It is noteworthy that the current density is very low (~ 10 mA cm^{-2}) in electrocatalytic CORR with H-cell configuration due to the extremely low solubility of CO in aqueous electrolyte solution. Thus, the work by Jiao and co-workers is a significant step-forward in electrocatalytic CORR to C_{2+} compounds.

A recent work revealed that a high concentration of the cation (i.e., Na^+) rather than OH^- might be the determining factor in promoting the formation of C_{2+} products during electrocatalytic CORR.²⁰³ By systematically varying the concentration of cations (Na^+) and OH^- at identical absolute electrode potential, that is on the standard hydrogen electrode (SHE) scale, Lu, Xu and their co-workers found that the partial currents of C_{2+} products, including C_2H_4 , CH_3COO^- , C_2H_5OH and $n-C_3H_7OH$, all increased with an increase in the concentration of Na^+ but not OH^- (Fig. 18c).²⁰³ The promotional effect of OH^- at the same potential on the RHE scale was attributed to the larger overpotential at higher electrolyte pH. The chelation of Na^+ with a crown ether to form a bulky organic cation while maintaining the concentration of OH^- significantly decreased the current density and the FE of C_{2+} products, providing further evidence that Na^+ played a pivotal role in the formation of C_{2+} products from CO.

To further increase in efficiencies for CO_2 RR in alkaline flow cell, Sargent, Sinton and their co-workers recently designed a catalyst/ionomer bulk heterojunction (CIBH) architecture, which could decouple gas, ion and electron transport.¹⁴⁵ The ionomer layer with hydrophobic and hydrophilic functionalities was assembled into an architecture with differentiated domains that favoured gas and ion transport route on the metal catalyst surfaces. Gas transport was promoted through a side chain of hydrophobic domains, leading to extended gas diffusion, while water uptake and ion transport took place through hydrophilic domains. The CIBH configuration with Cu catalyst in 7 M KOH electrolyte could offer a FE of C_2H_4 in the range of 65–75% and a peak partial current density of ~ 1.3 A cm^{-2} at a cathodic energy efficiency of 45%.¹⁴⁵ This C_2H_4 partial current density is the highest one reported to date.

The alkaline GDE design successfully circumvents mass-transport limitations associated with the low solubility of CO_2 /CO in aqueous solutions and enables to achieve superior performances at high reaction rates, resulting in a significant step toward to future practical applications. However, challenges remain in sustaining the high reaction rate for CO_2 RR in the alkaline flow cell over a long period of time. The flooding and the salt accumulation in the triple-phase boundary are two major reasons that can cause decreases in activity and selectivity in electrocatalytic CO_2 RR using the alkaline GDE. To solve the problem of the formation of carbonate salt due to the undesirable consumption of CO_2 by KOH in the alkaline GDE, neutral electrolytes, such as $KHCO_3$ and K_2SO_4 , were employed (Fig. 17b).^{146,200} However, the activity in neutral GDE is significantly lower than that of alkaline GDE because of the high ohmic resistance and overpotential. Moreover, to maintain the stability of catholyte in neutral electrolytes still remains an issue due

REVIEW

Energy & Environmental Science

to the reaction-driven pH increase. A recent work demonstrated that the electrodeposition of *N*-aryl-substituted-tetrahydro-bipyridine films on a Cu catalyst could achieve 72% FE of C₂H₄ with a current density of 320 mA cm⁻² at a potential of -0.83 V versus RHE during electrocatalytic CO₂RR in a liquid-electrolyte flow cell using 1.0 M KHCO₃ as the electrolyte.¹⁴⁶ It was found that, although the large current densities in the flow cell drove up local pH, the tetrahydro-bipyridine layer did not create a further pH gradient near the active Cu surface, and the layer was chemically robust to the locally alkaline environment. When the substituents in the organic modifier were changed to tune the electronic structure of organic films, the configuration of CO adsorption changed. A volcano-shaped relationship was observed between the FE of C₂H₄ and the ratio of atop-bound CO to bridge-bound CO. Thus, there is an optimum ratio of atop-bound CO to bridge-bound CO for the formation of C₂H₄. The DFT calculations indicated that the coupling of CO molecules located on atop–bridge pair sites was more facile than that of CO molecules on the bridge–bridge pair sites or top–top sites. The adhered *N*-aryl-substituted-tetrahydro-bipyridine molecules may help to optimise the pairs of atop- and bridge-bound CO.

The membrane electrode assembly (MEA) cell, which has been widely applied to the H₂–O₂ fuel cell, is emerging as an alternative for CO₂RR to solve the stability issue.²⁰⁰ In the MEA cell, the cathodic GDE contacts directly with an ion-exchange membrane instead of a catholyte (Fig. 17c). The stability issues associated with GDE flooding, electrolyte consumption with CO₂ and electrolyte ohmic loss may be solved. Sargent and co-workers integrated the Cu catalyst sputtered onto a porous polytetrafluoroethylene gas diffusion layer and modified with *N*-aryl-substituted-tetrahydro-bipyridine films into a MEA device.¹⁴⁶ They found that the system operated at a full-cell voltage of 3.65 V was stable at least for 190 h, offering a stable C₂H₄ FE of 64% and a stable current density of ~120 mA cm⁻².¹⁴⁶ This is probably the best stability achieved for electrocatalytic CO₂RR with current density of > 100 mA cm⁻². In general, the reaction rate in MEA is still lower than that in alkaline flow cell. Future studies should be focused on improving the ion conductivity of the membrane and the assembly craft.

As already mentioned, excellent performances could also be achieved for electrocatalytic CORR by using an alkaline flow cell.¹⁶³ The electrocatalytic CORR in alkaline flow cell has advantages over the CO₂RR because of no salt accumulation problem and potentially higher efficiencies towards C₂₊ products.^{43,163} Moreover, no formation of carbonates in alkaline electrolyte can increase the process economics, since the regeneration of KOH and CO₂ from the formed carbonates would be costly in the case of CO₂RR in alkaline flow cell.

It is noteworthy that the C₂₊ products in electrocatalytic CORR in alkaline flow cell contained a large fraction of C₂₊ oxygenates (such as C₂H₅OH, CH₃CHO, CH₃COO⁻, *n*-C₃H₇OH) and the FE of C₂H₄ was not very high (~40%).^{43,163} A recent work suggested that the coverage of CO on Cu surfaces determined the path for C₂H₄ formation or for C₂H₅OH formation.¹⁶⁴ Conventionally, it is generally believed that a higher CO coverage on Cu surfaces is beneficial to the formation of C₂₊ products.¹⁸⁰ Through analysing the possible paths for C₂H₄ and C₂H₅OH formation, Sinton and co-workers proposed that the higher CO coverage may favour the formation of C₂ oxygenates,

while the lower CO coverage may favour the formation of C₂H₄.¹⁶⁴ They found that the concentration of CO significantly influenced the product selectivity in electrocatalytic CORR in alkaline flow cell using KOH as the electrolyte. At a fixed potential of -0.44 V vs. RHE, the CORR in 1 M KOH offered C₂₊ products containing C₂H₄, C₂H₅OH, CH₃COO⁻ and C₃H₇OH, and the FE of C₂H₄ was ~30%. The decrease in CO concentration to 10% or 5% increase the FE of C₂H₄ to ~50% at the expense of mainly C₃H₇OH, but a further decrease in CO concentration led to a significant increase in H₂ formation. By tuning conditions to constrain local CO availability, C₂H₄ FEs of 65–72% could be achieved with high cathodic energy efficiencies (35–44%) and current densities (120–1250 mA cm⁻²).¹⁶⁴ The DFT calculations indicated that a lower CO coverage favoured the dehydroxylation of *CHCOH, which was probably the common intermediate for C₂H₄ and C₂ oxygenates, to *CCH, leading to C₂H₄. On the other hand, the higher CO coverage would be beneficial to the hydrogenation of *CHCOH to *CHCHOH, resulting in oxygenates.

Recently, Strasser and co-workers found that the co-feeding of CO and CO₂ could enhance the formation of C₂H₄ during electrocatalysis over an oxide-derived Cu catalyst.²⁰⁴ There existed an optimum ratio of CO/CO₂ in the gas mixture for C₂H₄ formation. Using operando differential electrochemical mass spectrometry capillary flow cell with millisecond time resolution, it was demonstrated that the enhanced C₂H₄ formation mainly originated from a cross-coupling between two *CO species derived from CO₂ and CO (the so-called CO₂–CO pathway). It was speculated that the co-fed CO did not compete with CO₂ for adsorption sites, implying non-competitive and reactant-specific sites for CO and CO₂ on Cu surfaces. These insights enabled the design of a tandem system of oxide-derived Cu in combination with Ni–N-functionalised carbon (NiNC), which involved NiNC for CO formation from CO₂ and Cu for CO–CO coupling, for electrocatalytic CO₂RR to C₂H₄ with doubled C₂H₄ yields.²⁰⁴

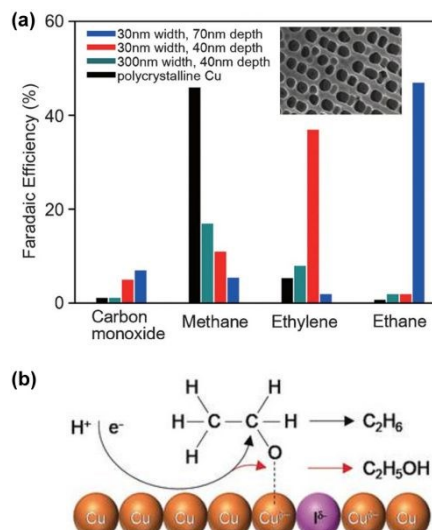


Fig. 19 (a) FEs of different CO₂RR products at -1.3 V versus RHE over polycrystalline Cu and mesoporous Cu catalysts with different widths and depths (inset: SEM image of mesoporous Cu).¹⁴⁷ (b) Reaction pathway toward the formations of ethane and ethanol

via ethoxy intermediate.¹⁴⁸ Reproduced from refs. 147 and 148, with the permissions of Wiley-VCH Verlag GmbH&Co. KGaA, copyright 2017 and 2020.

Besides C_2H_4 , C_2H_6 could also be obtained as a C_2 hydrocarbon product in electrocatalytic CO_2RR , although the selectivity of C_2H_6 was typically low in most cases. Nam and co-workers found that the selectivities of C_2H_4 and C_2H_6 could be tuned by using mesoporous Cu with different morphologies.¹⁴⁷ The mesoporous Cu catalysts with different pore widths and depths were fabricated by a thermal deposition method on anodized aluminium oxide. As the pore width decreased and the pore depth increased, the FE of C1 products gradually decreased and that of C_2 products increased. The FE of C_2H_4 reached 38% at the pore width and depth of 30 and 40 nm, respectively. As the pore depth increased to 70 nm, the major C_2 product changed to C_2H_6 and the FE of C_2H_6 was 46% (Fig. 19a). Through computational simulations, they proposed that the mesopore can change the local pH and prolong retention time of key intermediates, thus favouring deep hydrogenation of intermediates and promoting C_2H_6 formation.¹⁴⁷

Recently, Qiao and co-workers reported that an iodide-derived Cu was more selective for electrocatalytic CO_2RR to C_2H_6 than an oxide-derived Cu.¹⁴⁸ The iodide-derived Cu offered a normalized C_2H_6 selectivity of 72% (normalized to the total $C_2 + C_3$ products) at -1.0 V versus RHE, whereas that of oxide-derived Cu was only 27%. Through *in situ* X-ray absorption fine-structure (XAFS) and Raman spectroscopy studies, an O-bound ethoxy ($*OCH_2CH_3$) intermediate was detected during C_2H_6 formation and $*OCH_2CH_3$ was also responsible for C_2H_5OH formation (Fig. 19b).¹⁴⁸ The optimized oxidation state of Cu on iodide-derived Cu may stabilize the $*OCH_2CH_3$ intermediate and steer the reaction into C_2H_6 over C_2H_5OH .

4.2. Electrocatalytic CO_2RR and CORR into ethanol over Cu-based catalysts

Ethanol is a key chemical in both chemical and energy industries as well as in our daily life. It has widely been used as a fuel additive, alternative fuel, solvent or disinfectant, and can also serve as a versatile feedstock for the production of various chemicals and polymers.²⁰⁵ Traditionally, C_2H_5OH is primarily produced through the fermentation of sugars, and recently, the catalytic conversions of syngas derived from fossil resources (in particular natural or shale gas and coal) and cellulose have attracted much attention.^{38,206-212}

As described above, single Cu catalysts (in particular oxide-derived Cu catalysts) and some non-metallic dopant (e.g., boron and halogen)-modified Cu catalysts usually offer C_2H_4 as the major products during electrocatalytic CO_2RR . C_2H_5OH is typically formed as the second large product, and the ratio of FE of C_2H_5OH to that of C_2H_4 is typically lower than 0.5. DFT calculations suggested that the formation of C_2H_4 is more favourable than the formation of C_2H_5OH from CH_2CHO^* intermediate over Cu(100) surface.²¹³ It is generally believed that the incorporation of a different atom in the Cu lattice may alter its geometric and electronic structures, thus changing its selectivity and activity during CO_2RR . The design of bimetallic catalysts containing Cu and another guest metal such as Zn, Au or Ag

have shown potentials to improve the selectivity of C_2H_5OH especially C_2H_5OH in electrocatalytic CO_2RR .^{149,152,214,215/D0EE01860K}

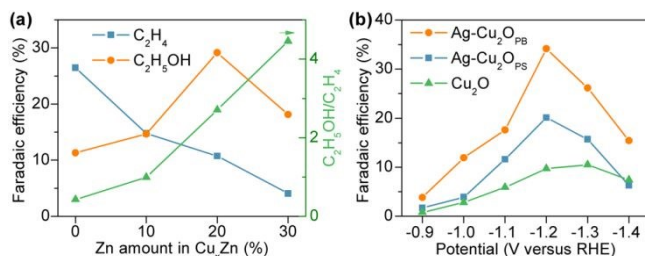


Fig. 20 (a) Maximum FEs of C_2H_4 and C_2H_5OH as well as the average $FE_{ethanol}/FE_{ethylene}$ ratio (calculated on the basis of the ratios measured at different potentials) in CO_2RR on Cu_xZn .¹⁴⁹ (b) Comparison of C_2H_5OH FEs on $Ag-Cu_2O_{ps}$, $Ag-Cu_2O_{pb}$ and Cu_2O .¹⁵⁰

Oxide film-derived Cu_xZn bimetallic catalysts were reported to exhibit enhanced selectivity towards C_2H_5OH .¹⁴⁹ Cu alone showed twice higher FE of C_2H_4 as compared to that of C_2H_5OH at most potentials studied, whereas CO was the major product along with a small fraction of $HCOO^-$ on Zn alone. By increasing the Zn content in the bimetallic catalysts, the maximum FEs of C_2H_5OH increased from 11.3% (on Cu) to 29.1% (on Cu_4Zn) and then decreased to 18.1% (on Cu_2Zn). Meanwhile, the maximum FEs of C_2H_4 decreased monotonically from 26.5% (on Cu) to 4.1% (on Cu_2Zn). The selectivities of C_2H_5OH versus C_2H_4 production, defined as the ratio of their FEs, could be modulated from 0.48 (on Cu) to 6 (on Cu_2Zn). The formation of C_2H_5OH was maximized on Cu_4Zn catalyst at -1.05 V versus RHE with a FE of 29.1% (Fig. 20a).¹⁴⁹ Although CO was a major product on Zn in the whole potential ranges investigated, the formation of CO was suppressed at potentials more negative than -1.0 V, where C_2H_5OH formation was significantly accelerated, over the Cu_4Zn and Cu_2Zn catalysts. Further, the formation of $HCOO^-$ was also inhibited over the bimetallic catalysts. These results suggest that Zn works synergistically with Cu to enhance the formation of C_2H_5OH . A dual-site mechanism has been proposed for the enhanced formation of C_2H_5OH . In brief, both Cu and Zn sites catalyse the reduction of CO_2 to CO, but Cu sites can work further for the formation of CHO or CH_x ($x = 1-3$) intermediates via CO. Zn sites provide CO, which might undergo spill-over to a nearby Cu site and then insert itself into the bond between Cu and $*CHO$ or $*CH_x$, eventually forming C_2H_5OH .¹⁴⁹

The deposition of Au nanoparticles on Cu foils without forming an alloy was found to enhance C_2H_5OH and C_3H_7OH formation at low overpotentials.²¹⁴ The Au/Cu catalyst had an earlier onset potential for alcohol production than either Cu or Au alone and it showed higher selectivity for alcohols as compared with hydrocarbons at lower overpotentials. Mechanistic studies suggest that Au nanoparticles work for the reduction of CO_2 to CO, driving a high CO coverage on the nearby Cu surface, enhancing the dimerization of CO and further reduction to C_{2+} compounds.

Several groups have studied Cu-Ag bimetallic catalysts for electrocatalytic CO_2RR to C_2H_5OH .^{150-152,215} For example, Lee and co-workers reported another interesting example to enhance the formation of C_2H_5OH by incorporating Ag, a CO formation electrocatalyst, into Cu_2O .¹⁵⁰ Two types of Ag-Cu₂O, phase-separated ($Ag-Cu_2O_{ps}$) and phase-blended ($Ag-Cu_2O_{pb}$) were fabricated by electrochemical co-deposition. The $Ag-Cu_2O_{pb}$ catalyst

REVIEW

Energy & Environmental Science

had more intimate contact between Ag and Cu atoms than the Ag–Cu₂O_{PS}. The maximum FEs of C₂H₅OH on Ag–Cu₂O_{PS} and Ag–Cu₂O_{PB} reached 20.1% and 34.2% at –1.2 V versus RHE, being twice and three times higher than that on pure Cu₂O, respectively (Fig. 20b).¹⁵⁰ This result also indicated the importance of intimate contact between Ag and Cu for synergistic formation of C₂H₅OH. Lee also pointed out the CO insertion mechanism for the enhanced C₂H₅OH. In other words, CO formed on Ag sites could migrate to Cu sites to couple with the CH_x intermediates, contributing to the formation of C₂H₅OH. The closer distance between Ag and Cu was vital for facilitating efficient CO transfer to Cu sites, thus affecting the ethanol selectivity. Nanoporous Cu–Ag alloy nanowires, which were fabricated by co-electrodeposition in the presence of 3,5-diamino-1,2,4-triazole (DAT), an additive to inhibit nucleation, and contained Cu and Ag atoms mixed homogeneously, demonstrated excellent performances for electrocatalytic CO₂RR to C₂H₄ and C₂H₅OH in alkaline flow cell.¹⁵¹ The FEs of C₂H₄ and C₂H₅OH reached ~60% and 25% and a current density of ~300 mA cm^{–2} at a cathode potential of only –0.7 V vs. RHE over the Cu–Ag alloy nanowires containing 6% Ag.¹⁵¹ The studies suggest that the presence of Ag may stabilise Cu₂O overlayer and keep optimal availability of CO intermediate, contributing to the enhanced formation of C₂₊ compounds. On the other hand, Bell and co-workers proposed a compressive-strain mechanism to explain the role of Ag in enhancing C₂₊ oxygenate formation over bimetallic Cu–Ag catalysts with surface alloy.²¹⁵ Briefly speaking, the formation of Cu–Ag surface alloy induced compressed strain in Cu lattice and thus modified the electronic structure of Cu, leading to decreases in the binding energies of H and O relative to CO. This results in the enhancement in the formation of C₂₊ oxygenates at the expense of C₂H₄ due to the reduced coverage of adsorbed H and the reduced oxophilicity of the compressively strained Cu.

Recently, Sargent and co-workers proposed through DFT calculations that after the introduction of Ag on Cu surfaces, the intermediates for the formation of C₂H₅OH would become more favourable than the formation of C₂H₄.¹⁵² They fabricated Ag/Cu catalysts with different Ag/Cu ratios by a co-sputtering technique. The morphology and in situ XAS characterizations indicated that Cu and Ag were distributed homogeneously in the bimetallic catalysts, forming Cu–Ag alloy phase. The best CO₂RR performance was achieved over the Ag_{0.14}/Cu_{0.86} catalyst, which exhibited a maximum FE of C₂H₅OH of 41% with current density of 250 mA cm^{–2} at –0.67 V vs. RHE in alkaline flow cell using 1 M KOH electrolyte.¹⁵² The cathodic energy efficiency reached 25%. Further in situ Raman spectroscopy studies suggest that the introduction of Ag into Cu could lead to multiple different binding configurations. The C₂H₄ formation path would be suppressed due to the unsaturated nature of C₂H₄ formation intermediates.

DFT calculations also suggest that the presence of vacancies on Cu surfaces, in particular on a Cu shell with a Cu₂S core, may increase the activation energy barrier for C₂H₄ formation via *CH₂CHO intermediate, which is believed as a common intermediate for both C₂H₄ and C₂H₅OH formations, while leaving that for C₂H₅OH formation mostly unaffected.¹⁵³ The Cu₂S@Cu-V catalyst with Cu₂S core and surface vacancy-enriched Cu shell, which is known as core-shell-vacancy engineering (CSVE) catalyst, showed enhanced

formation of C₂H₅OH and C₃H₇OH. In an alkaline flow cell with 1 M KOH as an electrolyte, the Cu₂S@Cu-V catalyst exhibited maximum

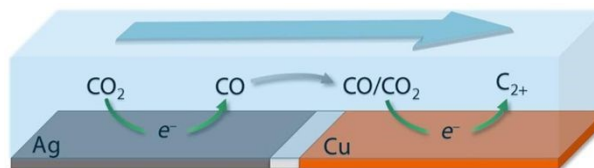


Fig. 21 Schematic illustration of tandem-catalysis strategy for CO₂RR to C₂₊ products.²¹⁷ Reproduced from ref. 217 with the permissions of American Chemical Society, copyright 2019.

FEs of C₂H₅OH and C₃H₇OH of 25 and 7% with a total current density of 400 mA cm^{–2}, respectively.¹⁵³ Cuanya and co-workers recently investigated the roles of surface defects and Cu(I) sites on Cu(100) surfaces in the formation of C₂₊ compounds.²¹⁶ They controlled the generation of surface defects and Cu(I) species on Cu(100) by designing a pulsed potential sequence applied, i.e., a brief pulse at an anodic potential to reconstruct Cu(100) surface and generate Cu(I), followed by a pulse at a cathodic potential (typically –1.0 V) for CO₂RR. The result indicated that the continuous regeneration of defects and Cu(I) species synergistically enhanced the C–C coupling especially to C₂H₅OH.²¹⁶

A tandem CO₂ electrocatalysis composed of two working electrodes (Ag and Cu) in a flow cell with 0.1 M CsHCO₃ electrolyte showed high FEs of C₂₊ oxygenates (Fig. 21).²¹⁷ Ag in the upstream worked for electrocatalytic CO₂RR to CO, which was then transported by convective flow to Cu to be converted to C₂₊ products. The ratio of oxygenates to C₂H₄ reached a maximum by operating Ag and Cu electrodes at –1 and –0.8 V, respectively, and the maximum FE of C₂₊ oxygenates was ~30%.²¹⁷ This tandem-catalysis concept has also been exploited to design and fabricate electrocatalysts such as Cu–Zn, Cu–Au and Cu–Ag bimetallic systems for CO₂RR to enhance the selectivity towards the formation of C₂H₅OH.^{149–152,214} Further, porphyrin-based metallic complex-immobilised Cu catalysts were recently reported to enhance the formation of C₂H₅OH during CO₂RR via the tandem mechanism.¹⁵⁴ A FeTPP[Cl] (5,10,15,20-tetraphenyl-21H,23H-porphine iron(iii) chloride)-modified Cu catalyst showed a maximum FE of C₂H₅OH of 41% with a partial current density of > 100 mA cm^{–2} at –0.82 V in a flow cell with 1 M KHCO₃ electrolyte. It was confirmed using ¹³CO₂ that the carbon in C₂H₅OH originated from CO₂. DFT calculations and control experiments suggested that the molecular complex mainly functioned for the reduction of CO₂ to CO, generating a rich *CO environment at molecule-metal interface, increasing the coverage of *CO on Cu surfaces.¹⁵⁴ This lowers the energy barrier for C–C coupling and favours the formation of C₂H₅OH.

Carbon materials have also shown potentials to modulate the products on Cu/carbon-catalysed CO₂RR.^{155–158,218} An early study reported that Cu nanoparticles loaded on a highly textured N-doped carbon nanospike film (CNS) could achieve high ethanol selectivity in electrocatalytic CO₂RR, whereas there was no ethanol formation over Cu/glassy carbon or bare CNS.¹⁵⁵ It was claimed that the Cu/CNS offered 63% FE of C₂H₅OH at –1.2 V versus RHE, whereas CO and CH₄ were the major CO₂RR products on CNS or Cu/glassy carbon catalysts (Fig. 22a). A synergistic effect between Cu and CNS was speculated

to accelerate the formation of C_2H_5OH . Very recently, Sargent and co-workers developed an electrocatalyst composed of Cu

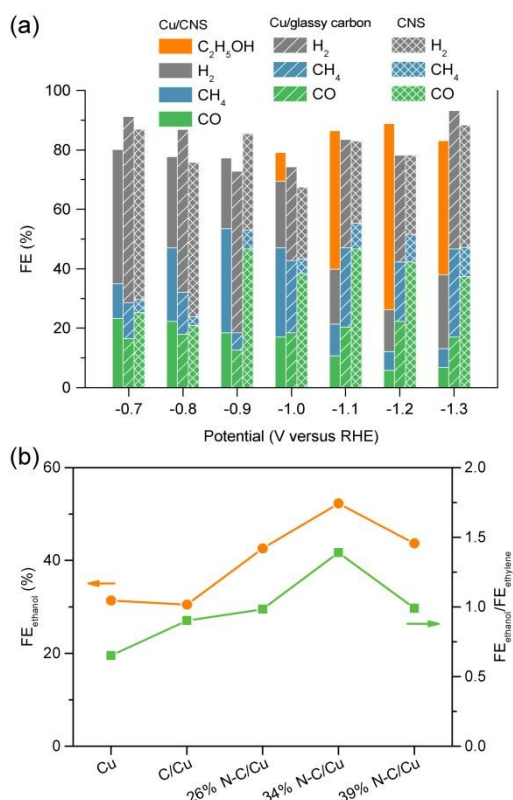


Fig. 22 (a) FFs of CO₂RR products at different potentials on Cu/CNS, Cu/glassy carbon and CNS catalysts.¹⁵⁵ (b) FEs of C₂H₅OH and the ratios of FE_{ethanol} to FE_{ethylene} at 300 mA cm⁻² on different catalysts.¹⁵⁶

nano-particles surrounded by N-doped carbon layers (denoted as N-C/Cu), which displayed high FEs of C₂H₅OH at high reaction rates.¹⁵⁶ The CO₂RR in a flow cell with 1 M KOH electrolyte using the 34% N-C/Cu (the percentage of N in the N-C layer = 34%) catalyst offered a total C₂₊ FE of 93% and a C₂H₅OH FE of 52% at a current density of 300 mA cm⁻² at -0.68 V vs. RHE.¹⁵⁶ This C₂H₅OH FE was significantly higher than that on Cu alone and the use of carbon-only layer to cover Cu did not improve the FE of C₂H₅OH as compared to Cu alone (Fig. 22b).¹⁵⁶ It is noteworthy that no C₂H₅OH was formed on the bare 34% N-C layer. These observations indicate the crucial role of the N-C layer on Cu surfaces in the formation of C₂H₅OH. The indispensability of nitrogen might imply that the electron-donating ability of the capping layer is a key. DFT calculations suggest that the confinement effect of Cu by N-C layer may stabilise the C-O bond of *CH-CHOH, the intermediate for the formation of either C₂H₅OH or C₂H₄, thus facilitating the path toward C₂H₅OH and suppressing that toward C₂H₄.

It is noteworthy that g-C₃N₄ cannot only be applied to photocatalytic CO₂ reduction,⁶³ but also holds the potential to tune the selectivity of C₂₊ products on Cu catalyst during the electrocatalytic CO₂RR. From DFT calculations, Qiao and co-workers revealed that g-C₃N₄ could modify the electronic structure of Cu in a Cu-g-C₃N₄ composite by shifting its d-orbital position toward the Fermi level, thus leading to a stronger

adsorption of intermediates.²¹⁸ In addition, the Cu-g-C₃N₄ composite shows an intramolecular synergistic effect with dual active centres (Cu and C) on electrocatalytic CO₂RR, different from the widely studied bifunctional catalysts composed of a metallic site and a support. Actually, the fabricated Cu-g-C₃N₄ catalyst was able to produce a wider variety of C₂ products (C₂H₄, C₂H₆ and C₂H₅OH) in electrocatalytic CO₂RR, whereas a Cu/N-doped graphene catalyst only provided C₁ products.²¹⁸

A comparison of CORR and CO₂RR on polycrystalline Cu has demonstrated that there is a large decrease in the overpotential for C-C coupling products during CORR.²⁰² Some studies have demonstrated that the electrocatalytic CORR on single Cu catalysts operated at a low overpotential can afford C₂H₅OH as the major product,^{163-167,219} whereas C₂H₄ is usually formed as the major product in CO₂RR on single Cu catalysts operated at higher overpotentials. For example, Kanan and co-workers found that an oxide-derived nanocrystalline Cu catalyst, which was fabricated by annealing polycrystalline Cu foil at 500 °C in air followed by electroreduction, offered C₂₊ oxygenates (C₂H₅OH, CH₃COO⁻ and C₃H₇OH) with a FE of 57% (C₂H₅OH FE: 43%) at -0.3 V versus RHE for electrocatalytic CORR.¹⁶⁵ On the other hand, a commercial Cu-nanoparticle catalyst provided H₂ as the major product under the same conditions. Characterisations of the oxide-derived Cu catalyst revealed particles with sizes of 30–100 nm and interconnected nanocrystalline networks with distinct grain boundaries between nanocrystals. The oxide-derived Cu catalyst reduced by H₂ at 130 °C instead of electroreduction also showed nearly 50% FE towards C₂₊ oxygenates (C₂H₅OH and CH₃COO⁻) in electrocatalytic CORR.¹⁶⁵ However, the annealing of the oxide-derived Cu catalyst in N₂ at 350 °C resulted in significant decreases in surface-area corrected current density and FE of CO reduction (<5%) as well as a remarkable increase in grain sizes. It is thus proposed that the excellent C₂₊ oxygenates (mainly C₂H₅OH) selectivity on oxide-derived Cu is not a consequence of nanocrystalline size or morphology. Instead, the grain boundaries play a pivotal role in electrocatalytic CORR to C₂₊ oxygenates.^{165,219}

Kanan and co-workers further fabricated Cu/carbon nanotubes (Cu/CNT) catalysts with different average grain-boundary densities by depositing Cu onto a film of superaligned CNTs using e-beam evaporation.¹⁶⁶ TEM characterisations showed that the CNTs were decorated with Cu NPs, most of which consisted of multiple Cu crystallites connected by grain boundaries. The density of grain boundaries, defined as the sum of surface grain boundary lengths divided by the sum of NP surface areas, was evaluated by TEM, and the fabricated Cu/CNT had a grain boundaries of $40.6 \pm 4.3 \mu\text{m}^{-1}$. The density of grain boundaries decreased monotonically by increasing the annealing temperature from 200 to 500 °C in N₂. The Cu/CNT catalyst showed a FE of 72% towards C₂H₅OH and CH₃COO⁻ with a current density of 0.37 mA cm⁻² at -0.3 V during the electrocatalytic CORR.¹⁶⁶ The catalyst after annealing showed increased FE of H₂ evolution at the expense of CO-reduction products. A strong relationship was found between the density of surface grain boundaries and the CO electrocatalytic activity.

REVIEW

Energy & Environmental Science

Cu nanowires, which were fabricated by reducing CuO nanowires by H₂ at 150 °C, also showed higher selectivity of C₂₊ oxygenates during CORR.¹⁶⁷ The FE of C₂H₅OH reached 50% with 65% FE towards total CO reduction products at a current density of −0.36 mA cm^{−2} at −0.22 V vs. RHE.¹⁶⁷ The H₂ reduction of CuO nanowires at higher temperatures led to significantly lower FE of CO reduction. Characterisations and DFT calculations suggested that the coordinately unsaturated (110) surface sites on Cu nanowires might be responsible for CORR to ethanol.¹⁶⁷ Jaramillo, Hahn and co-workers recently demonstrated that the roughness factor of Cu electrode was a key to determining the product selectivity of CO reduction.¹⁶⁹ By comparing Cu catalysts with different morphologies, such as nanoflowers, nanodendrites, nanowires and nanorods, they found that the activity of CORR and selectivity of C₂₊ oxygenates increased almost linearly with an increase in the roughness factor. It is of interest that although the current density was quite low, the nanoflower Cu catalysts with the highest roughness factor could offer a nearly 100% selectivity to C₂ oxygenates (C₂H₅OH, CH₃CHO and CH₃COO[−]) without detectable H₂ evolution at an applied potential of only −0.23 V versus RHE. Acetaldehyde was the major product with a FE of ~60% and the current density was ~0.2 mA cm^{−2} at this applied potential. The change in the applied potential to −0.33 V increased the current density to ~0.6 mA cm^{−2}, and meanwhile C₂H₅OH became the major product with a FE of ~60%. It was proposed that the porous mesostructure might contribute to suppressing H₂ evolution and enabling highly selective formation of C₂ oxygenates at a quite low overpotential.¹⁶⁹

Very recently, Jaramillo, Hahn and co-workers demonstrated that a Cu–Ag bimetallic electrocatalyst could achieve a high FE of CH₃CHO during electrocatalytic CORR in 0.1 M KOH electrolyte.¹⁷⁰ The FE of CH₃CHO reached 50% and the carbon-based selectivity of CH₃CHO reached 90% at a potential of −0.536 V vs. RHE. The FE of CH₃CHO could be further enhanced to 70% by using a porous bimetallic Cu–Ag nanoflower electrocatalyst with an increased roughness factor. DFT calculations suggested that the Ag-adatoms on Cu weakened the binding energy of the reduced acetaldehyde intermediate, thus suppressing its further reduction to C₂H₅OH.

4.3. Electrocatalytic CORR into acetate over Cu-based catalysts

Acetate is a versatile chemical in the current chemical industry, which can be used for the production of vinyl acetate monomer, cellulose acetate, acetate esters and polyhydroxyalkanoate (PHA) or used as a solvent in many processes such as the production of polyethylene terephthalate (PET). Recent studies demonstrated that the electrocatalytic synthesis of acetic acid would also be a very promising route for the utilization of CO₂ via CO.⁴³

As described above, although electrocatalytic CORR could offer high FEs of C₂ oxygenates at relatively low overpotentials, the current density in the conventional H-cell was typically very low (< 10 mA cm^{−2}) mainly due to the low solubility of CO.^{165–167,169,170} Recently, Kanan and co-workers designed flow cell with GDE to circumvent the problem of low CO solubility.¹⁷¹ It is reported that the electrocatalytic CORR in flow cell with Cu

catalyst and NaOH electrolyte could achieve not only high current density (> 100 mA cm^{−2}) and high ¹³C/¹²C FE but also high CO single-pass conversion. At a full cell potential of 2.4 V, the CO single-pass conversion reached 43% and acetate concentration

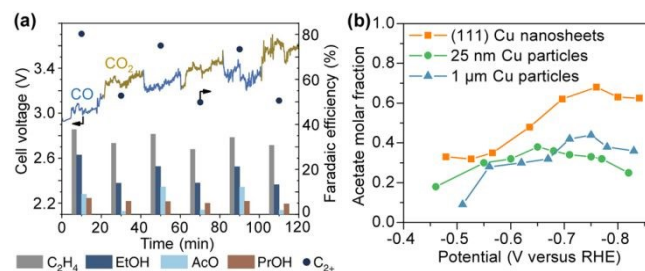


Fig. 23 (a) CO/CO₂ reduction on OD-Cu at 300 mA cm^{−2} in 1 M KOH over 2 h.¹⁶³ (b) Acetate molar fraction excluding hydrogen for CO reduction over (111) Cu nanosheets, 25 nm Cu particles and 1 μm Cu nanoparticles catalysts.¹⁷² Reproduced from ref. 163 and 172, with the permission of Springer-Nature, copyright 2018 and 2019.

reached 1.1 M over 24 h. Meanwhile, the FE of acetate and current density were 30% and 144 mA cm^{−2}, respectively. It is noteworthy that in the work reported by Kanan and co-workers, very limited CO flow rate (1.0 mL min^{−1}) and high CO pressure (4 bar) were used.¹⁷¹

At the same time, Jiao and co-workers discovered that after switching the reactant from CO₂ to CO over an oxide-derived Cu catalyst in an alkaline flow cell, the selectivity of C₂₊ oxygenates especially for acetate increased significantly and the FE of acetate could reach ~20% (Fig. 23a).¹⁶³ The C¹⁸O isotopic-labelling studies revealed that one oxygen of acetate originated from CO and the other oxygen originated from the electrolyte, probably from an OH[−]. The pH-gradient simulations for CO₂/CO reduction under various current densities clarified that the pH at electrode surfaces during CO reduction was much higher than that during CO₂ reduction, because of the carbonate formation through a fast chemical reaction between CO₂ and KOH. They thus attributed the high acetate selectivity in CORR to higher local pH at the electrode-electrolyte interface.

The same group further reported a freestanding triangle-shaped two-dimensional Cu-nanosheet catalyst, which exhibited an acetate FE of 48% with a current density of 200 mA cm^{−2} at −0.736 V vs. RHE for electrocatalytic CORR in flow cell with 2 M KOH electrolyte.¹⁷² This value of FE is the highest one reported to date for electrocatalytic synthesis of acetate. The Cu nanosheet catalyst, which was fabricated by chemical reduction of Cu(II) nitrate with ascorbic acid in the presence of hexadecyltrimethylammonium bromide (CTAB) and hexamethylenetetramine (HMTA), selectively exposed the (111) surface. As compared to Cu nanoparticles with polycrystalline surfaces, the Cu-nanosheet catalyst exhibited a similar intrinsic activity towards acetate formation but much suppressed intrinsic activities towards the formations of ethylene and ethanol, thus leading to a higher selectivity of acetate (Fig. 23b). Previous studies indicated that (100) and (110) facets were responsible for the formations of C₂H₄ and C₂H₅OH, respectively.¹⁷⁸ Thus, the preferentially exposed (111)

surface of the Cu-nanosheet catalyst was proposed to contribute to the high acetate selectivity.¹⁷² DFT calculations suggested that the formation of acetate may proceed through a ketene intermediate (CH_2CO) with the oxygen from CO molecule, and the incorporation of another oxygen from H_2O (or OH^-) resulted in the formation of acetic acid or acetate.

4.4. Electrocatalytic CORR into *n*-propanol over Cu-based catalysts

Higher alcohols, such as *n*-propanol, which have impressive volumetric energy densities (27 MJ L⁻¹ for *n*-C₃H₇OH) and excellent octane numbers (118 for *n*-C₃H₇OH), can be used as engine fuels. Typically, *n*-C₃H₇OH can be observed accompanying with C₂H₅OH and/or C₂H₄ in electrocatalytic CO₂RR or CORR on Cu catalysts under suitable conditions, but its selectivity is usually lower. For example, *n*-C₃H₇OH was formed with a FE of ~5% in CO₂RR on a Cu catalyst composed of monodisperse Cu nanoparticles deposited on carbon paper support.²²⁰ The Cu₂S@Cu-V catalyst with Cu₂S core and surface vacancy-enriched Cu shell offered a *n*-C₃H₇OH FE of ~7%.¹⁵³ A high FE (~13%) of *n*-C₃H₇OH was once reported during electrocatalytic CO₂RR on a Cu mesh-supported oxide-derived Cu catalyst at a potential of -0.9 V vs. RHE.²²¹ In electrocatalytic CORR, the oxide-derived Cu catalyst provided a FE of *n*-C₃H₇OH of ~10%.¹⁶⁵ It is expected that the key step in *n*-propanol formation may be the coupling between surface-adsorbed C1 and C₂ intermediates. However, the inadequate stabilization of C₂ intermediates on pristine Cu surfaces would result in desorption rather than further intermolecular coupling with C1 intermediates to form C₃ products. A few recent studies have contributed to developing strategies to design selective catalysts for the formation of *n*-C₃H₇OH.¹⁷³⁻¹⁷⁵

The first strategy is the confinement effect to enhance the concentration of C₂ intermediates. Sargent, Sinton and co-workers fabricated open Cu-nanocavity catalysts with tuneable geometry by acidic etching of Cu₂O nanoparticles and found that proper opening could significantly promote the formation of *n*-propanol during electrocatalytic CORR.¹⁷³ The FE of *n*-propanol reached 21% with a partial current density of 7.8 mA cm⁻² at -0.56 V versus RHE in an alkaline GDE, much better than solid and fragment Cu catalysts (Fig. 24a). Through finite element method (FEM) simulations, they found the nanocavity geometry could concentrate C₂ species via steric confinement and reduce the desorption of C₂ species, thus promoting the coupling to form a C₃ product.¹⁷³ DFT calculations suggest that the coupling between C₂ species and CO is the most likely route for the formation of C₃ species. A lower C₂ surface coverage would reduce the likelihood that CO and C₂ species meet to form C₃ species, and thus the enhancement in the concentration of C₂ species is vital to increasing the C₃ selectivity.

The second strategy is to create interfaces of (100) and (111) facets, which are selective towards C₂ and C1 species, respectively.¹⁷⁴ For this purpose, a highly fragmented (HF) Cu catalyst was fabricated by a slow hydrolysis and oxidation of CuI in aqueous solution to Cu₂O with a variety of crystalline phases, followed by in situ reduction on a GDE during CORR. TEM confirmed that the HF-Cu catalyst possessed Cu(100) and Cu(111) facets that were adjacent and comprised mostly fragments below 200 nm² (all fragments < 700 nm²). The electrocatalytic CORR in a flow cell with GDE and 1 M KOH

electrolyte showed that the HF-Cu catalyst exhibited a maximum FE of *n*-C₃H₇OH of 20.3% at -0.45 V vs. RHE (at overpotential of 0.55 V, iR corrected) (Fig. 24b).¹⁷⁴ The partial current density for *n*-C₃H₇OH formation was 8.5 mA cm⁻² at this electrode potential and the full cell electric power to chemical energy conversion efficiency was 10.8%. The control

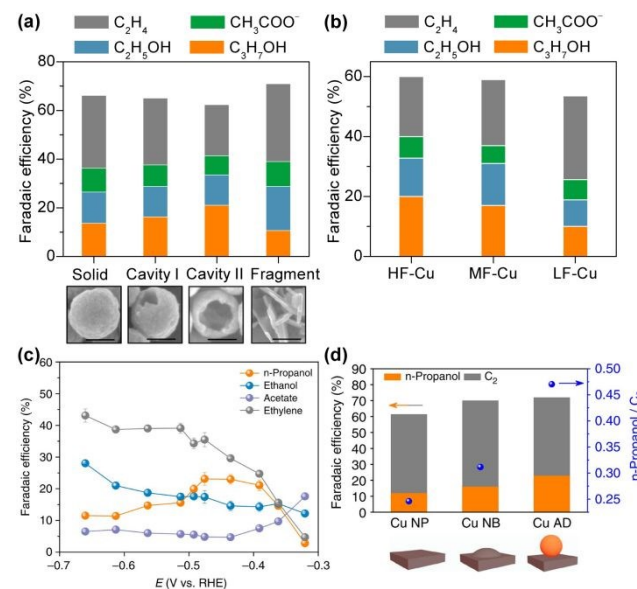


Fig. 24 (a) FEs of C₂₊ products in CORR at -0.56 V versus RHE on Cu-based catalysts with morphologies of solid, cavity I, cavity II and fragment as well as the corresponding SEM images. Scale bars, 100 nm.¹⁷³ (b) FEs of C₂₊ products in CORR at -0.45 V versus RHE on high-fragment Cu (HF-Cu), medium-fragment Cu (MF-Cu) and low-fragment Cu (LF-Cu) catalysts.¹⁷⁴ (c) FEs of C₂₊ products in CORR at different potentials on Cu adparticle catalysts.¹⁷⁵ (d) Maximum FEs of *n*-propanol and ratios of *n*-propanol FE to C₂₊ FE on Cu nanoparticle (NP), nanobump (NB) and Cu adparticle (AD).¹⁷⁵ Reproduced from refs. 173, 174 and 175, with the permission of Springer-Nature, copyright 2018 and 2019.

experiments with medium-fragmented (MF) and low-fragmented (LF) Cu catalysts further demonstrated that the interface between Cu(100) and Cu(111) played a critical role in the formation of *n*-C₃H₇OH (Fig. 24b).

The third strategy is to load Cu adparticles on Cu surfaces to enhance the adsorption of CO and binding energy of C₂ intermediates.¹⁷⁵ DFT calculations indicated that the presence of adatoms on pristine Cu surfaces, i.e., Cu(100), Cu(111) and Cu(211), could increase the CO adsorption. The adsorption of C₂ intermediates (*CCH₂ and *OCCOH) was stabilised on the Cu(111) surface in the presence of Cu adatoms. The reaction energies for *CO dimerization and the coupling between *CO and *CCH₂ or *OCCOH were lowered in the presence of Cu adatoms on the pristine Cu surfaces. Adparticle-covered Cu nanoparticle catalysts were fabricated by in situ electroreduction of a nanoparticulate copper oxide precursor deposited on a GDE under a rich CO condition, which enabled simultaneous rapid reduction of oxide and growth of adparticle. Electrocatalytic CORR in a flow cell with 1 M KOH electrolyte showed a maximum FE of *n*-C₃H₇OH of 23% at -0.44 to -0.47 V vs. RHE (Fig. 24c). The partial current of *n*-C₃H₇OH reached 11 mA cm⁻² at -0.47 V vs. RHE. The control experiments using adparticle-free Cu nanoparticles and the catalyst by reduction

REVIEW

Energy & Environmental Science

of the nanoparticulate copper oxide under N_2 instead of CO, which contained nanobumps (NBs) on surfaces, showed lower maximum FEs of $n\text{-}C_3H_7OH$ (Fig. 24d). The partial pressure of CO played a key role in the formation of $n\text{-}C_3H_7OH$ and it was found that the FE of $n\text{-}C_3H_7OH$ increased at the expense of that of C_2H_4 upon increasing the CO partial pressure.¹⁷⁵ This further supports the hypothesis that $n\text{-}C_3H_7OH$ is formed by coupling between CO and the C_2 intermediate, which may also be converted to C_2H_4 .

4.5. Electrocatalytic CO_2RR and CORR into C_{2+} over other catalysts than Cu

High FEs towards C_{2+} compounds have made Cu a star catalyst for electrocatalytic CO_2RR and CORR. One of the major reasons for the high C_{2+} FEs of Cu-based catalysts is believed to be the appropriate CO-binding ability. If a metal binds CO too weakly, CO would desorb rapidly as a final product, whereas a too strong CO adsorption of a metal would increase the difficult for the further conversion of surface CO species. The CO_2RR to C_{2+} products on Cu usually requires potentials more negative than or close to -1.0 V to achieve high current densities. The search for other electrocatalytic materials other than Cu might enable the CO_2RR to C_{2+} products to proceed at lower overpotential, thus resulting in alternative lower-energy pathways.

Several bimetallic catalysts that do not contain Cu have shown potentials to offer C_{2+} products during CO_2RR . Kortlever et al. demonstrated that a Pd–Au bimetallic catalyst fabricated by electrodeposition of Pd, which could bind CO strongly, on Au without strong binding to CO afforded $C_1\text{--}C_5$ hydrocarbons and C_{2+} oxygenates including ethanol and acetate besides HCOOH and CH_3OH .²²² The onset potential for the formation of hydrocarbons was -0.8 V vs. RHE. Electrocatalytic CORR to $C_1\text{--}C_5$ hydrocarbons could also take place on the Pd–Au catalyst with a slightly lower onset potential of -0.6 V, suggesting that CO was a key intermediate. The active sites were proposed to be Pd-rich Au–Pd alloy thin layer on the catalyst surface. The FE of C_{2+} products was $< 5\%$. Several Ni-based bimetallic catalysts have also been investigated for electrocatalytic CO_2RR to C_{2+} compounds.^{223–225} The Ni–Ga intermetallic compound is an interesting catalyst, since it has similar oxygen adsorption energy to Cu and has shown comparable or even better performance as compared to the well-known Cu–Zn–Al catalyst in the hydrogenation of CO_2 to CH_3OH .²²³ In electrocatalytic CO_2RR , the Ni–Ga intermetallic catalyst could work for the formation of C_{2+} hydrocarbons, mainly C_2H_4 and C_2H_6 , in addition to CH_4 .²²⁴ The onset potential for the formation of C_2H_4 and C_2H_6 on the Ni–Ga was -0.48 V vs. RHE, even more positive than that reported for Cu catalysts. The Ni₃Al intermetallic compound was reported to show the formation of C_3 oxygenates, including $n\text{-}C_3H_7OH$ and acetone, during the electrocatalytic CO_2RR .²²⁵ The FEs of C_{2+} products using these bimetallic electrocatalysts that do not contain Cu are still quite low ($< 5\%$).

Nitrogen-doped carbon-based materials have been reported to be candidates for metal-free electrocatalytic CO_2RR to C_{2+} products, in particular C_2 oxygenates.^{159–162,226–228} Quan and co-workers reported that a nitrogen-doped nanodiamond (NDD) catalyst deposited on Si rod array could work for the

electrocatalytic CO_2RR to CH_3COO^- and $HCOO^-$ in $NaHCO_3$ electrolyte.¹⁵⁹ The total FE toward CO_2 reduction was 91.8% with a current density of ~ 7 mA cm⁻² at -1.0 V vs. RHE. The FE of CH_3COO^- reached $\sim 78\%$ at the same time. The high overpotential for H_2 evolution on the NDD catalyst was proposed to favour the FE of CO_2 reduction. In situ FT-IR studies suggested the appearance of OOC–COO species, which might be a reaction intermediate. Further studies showed that the presence of nitrogen with proper content ($\geq \sim 2$ at.%) and its chemical state played crucial roles. The N-sp³C was found to be more active than the N-sp²C. It was speculated that the defect sites and the polarised carbon atoms adjacent to nitrogen might stabilise the CO_2^{*-} through electronic interactions. The coupling between CO_2^{*-} was proposed to account for the formation of CH_3COO^- .¹⁵⁹

A boron- and nitrogen-co-doped nanodiamond (BND) catalyst deposited on Si substrate was found to be very selective for the formation of CH_3OH during the electrocatalytic CO_2RR in H-cell with 0.1 M $NaHCO_3$ electrolyte.¹⁶⁰ A surprisingly high CH_3OH FE of 93.2% was claimed on a BND catalyst with 2.5 at.% boron and 4.9 at.% nitrogen at -1.0 V versus RHE in spite of the low current density (~ 1 mA cm⁻²). The increase in nitrogen content in BND catalysts from 3.1 at.% to 3.6 at.% and further to 4.9 at.% (from BND1 to BND2 and further to BND3) while keeping the boron content at 2.4–2.5 at.% increased the FE of CH_3OH (Fig. 25a). It is of interest that the nitrogen-doped

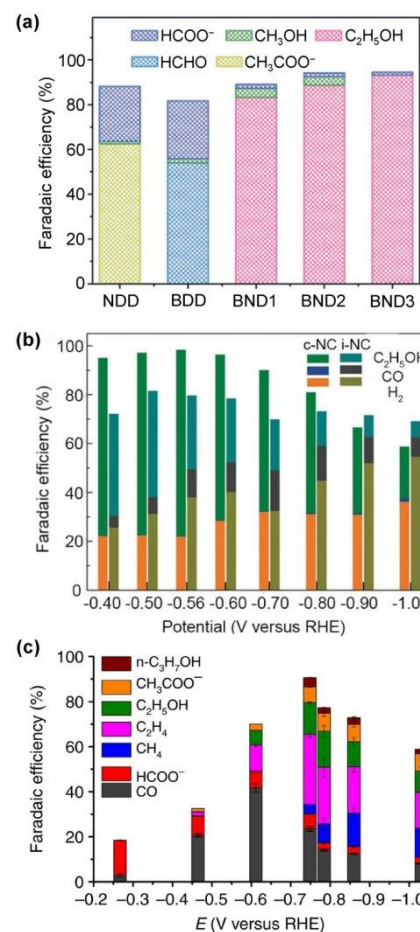


Fig. 25 (a) FE_s for CO₂ reduction on NDD, BDD, BND1, BND2 and BND3 at -1.0 V versus RHE.¹⁶⁰ (b) FE_s for CO₂ reduction on cylindrical mesoporous carbon (c-NC) and inverse mesoporous carbon (i-NC) catalysts at various applied potentials.²²⁶ (c) FE_s for CO₂ reduction at various applied potentials for NGQDs.¹⁶² Reproduced from refs. 160, 226 and 162, with the permission of Wiley-VCH Verlag GmbH&Co. KGaA and Springer-Nature, copyright 2017 and 2016.

nanodiamond (NDD) mainly provided CH₃COO⁻ and HCOO⁻, whereas HCHO and HCOO⁻ were the major products on the boron-doped nanodiamond (BDD) catalyst (Fig. 25a). Thus, the doping of nitrogen may be the key to C-C coupling. DFT calculations on the (111) facet of BND suggested that the CO₂RR might proceed via the following intermediates: CO₂ → *COOH → *CO → *COCO → *COCOH → *COCHOH → *COCH₂OH → *CHOCH₂OH → *CH₂OCH₂OH → CH₃CH₂OH.¹⁶⁰ The doped nitrogen and boron would work synergistically for the formation of C₂H₅OH.

Chen, Sun and co-workers demonstrated that a N-doped ordered cylindrical mesoporous carbon (denoted as c-NC) catalyst showed high selectivity toward C₂H₅OH during CO₂RR in 0.1 M KHCO₃ electrolyte.²²⁶ The FE of C₂H₅OH reached 77% with current density of ~0.2 mA cm⁻² at -0.56 V vs. RHE (Fig. 25b). The presence of nitrogen was also confirmed to play key roles in CO₂ reduction and C-C coupling, since H₂ evolution was the major reaction on the ordered cylindrical mesoporous carbon without nitrogen. The cylindrical mesoporous structure was also important, and the reference N-doped inverse mesoporous carbon only showed a much lower FE of C₂H₅OH (~44%) at -0.50 V vs. RHE and CO was formed as a major product. DFT calculations suggested that the pure carbon or graphitic N sites were highly unfavourable for the formation of *CO, which was the key intermediate for C₂ formation, whereas both pyridinic and pyrrolic N sites could work for the *CO formation.²²⁶ The formation of *CO proceeded preferentially on the pyridinic N site. The ordered channel surface with high electron density might stabilise *CO, thus favouring the coupling between *CO, and might also facilitate the subsequent multiple electron and proton transfer to form C₂H₅OH. A recent work from the same group demonstrated that the pore-structure engineering by constructing hierarchical micro-/mesoporous N-doped carbon materials could further enhance the formation of C₂H₅OH.¹⁶¹ The creation of medium micropores (~0.52 nm) in the channel walls of the N-doped ordered mesoporous carbon resulted in a FE of C₂H₅OH of 78% with a current density of ~2 mA cm⁻² at -0.56 V vs. RHE during CO₂RR in H-cell with 0.1 M KHCO₃ electrolyte. The formation rate of C₂H₅OH reached 2.3 mmol g⁻¹ h⁻¹ at -0.8 V vs. RHE, which was one order of magnitude higher than that on the corresponding catalyst without micropores. Further experiments and DFT calculations suggested that the microporous structure with the active pyridinic and pyrrolic N sites might lead to fast kinetics of charge transfer and high electric driving potentials to enhance the formation of ethanol.¹⁶¹

N-doped graphene quantum dots (NGQDs) were also found to be efficient for the electrocatalytic CO₂RR into C₂₊ products.¹⁶² C₂H₄, C₂H₅OH, CH₃COO⁻ and n-C₃H₇OH were all formed in CO₂RR in a flow cell with DGE and 1 M KOH electrolyte. The maximum FE of C₂H₄ was 31% at -0.75 V versus

RHE, and the total FE of C₂₊ products was 55% at the same time (Fig. 25c).¹⁶² The maximum FE of C₂₊ oxygenates was 26% at -0.78 V versus RHE with 16% FE of C₂H₅OH. The flow cell with DGE also resulted in high current density, and the partial current

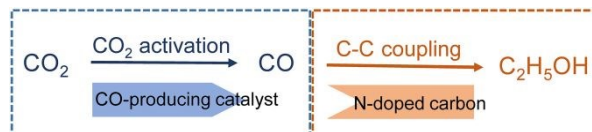


Fig. 26 Simplified mechanism on bifunctional catalyst for CO₂RR to ethanol by integrating CO synthesis and C-C coupling.

densities of CO, C₂H₄ and C₂H₅OH were 23, 46 and 21 mA cm⁻² at -0.86 V vs. RHE. On the other hand, CO and HCOO⁻ were the major products on the graphene quantum dots without nitrogen or the nitrogen-doped reduced graphene at similar applied potentials. Thus, it was confirmed again that the nitrogen sites played crucial roles in the formation of C₂₊ products. Further, the result indicated that the pyridinic N at edge sites were more efficient for C-C coupling than the pyridinic N at basal planes.

Recently, some studies have demonstrated that the addition of a catalyst component that can accelerate the CO₂RR to CO and the N-doped carbon can enhance the formation of C₂ oxygenates (Fig. 26).²²⁹⁻²³¹ For example, the immobilisation of a molecular catalyst, i.e., Ru(II) polypyridyl carbone complex (RuPC), which was efficient for electrocatalytic CO₂RR to CO, onto N-doped porous carbon (NPC) was found to show synergistic effects in the formation of C₂₊ products.²²⁹ The NPC alone could catalyse the electrocatalytic CO₂RR in H-cell with 0.5 M KHCO₃ electrolyte, forming C₂H₅OH, CH₃COO⁻, methanol, HCOO⁻ and CO. The immobilisation of RuPC onto NPC significantly enhanced the formation of C₂H₅OH. At -0.97 V vs. NHE, the FE_s of C₂H₅OH and CH₃COO⁻ were 27.5% and ~10%, respectively, on the RuPC/NPS, whereas they were ~15% and 10% on NPC. It was speculated that the RuPC enhanced the electrocatalytic reduction of CO₂ to CO and the increased coverage of *CO species on NPC or at the interface between RuPC and NPC would facilitate the C-C coupling to form C₂H₅OH. The loading of Ag nanoparticles, which are known to catalyse the CO₂RR to CO, onto a 3D graphene-wrapped nitrogen doped carbon foam (G-NCF) has also been found to enhance C₂H₅OH formation during electrocatalytic CO₂RR in H-cell with 0.1 M KHCO₃ electrolyte.²³⁰ The FE of C₂H₅OH reached 85.2% at -0.6 V vs. RHE despite the low current density (< 0.5 mA cm⁻²). The anchoring of CoO onto N-doped carbon materials composed of mesoporous carbon and carbon nanotube resulted in an efficient catalyst (Co/MC-CNT) for electrocatalytic CO₂RR to ethanol.²³¹ The maximum FE of C₂H₅OH on this catalyst was 60.1% at -0.32 V vs. RHE during the electrocatalytic CO₂RR in H-cell with 0.5 M KHCO₃ electrolyte. CH₃CHO, probably the precursor of C₂H₅OH, and H₂ were observed as the only by-products under such conditions. The FE of CH₃CHO was 10% and

REVIEW

Energy & Environmental Science

the partial current of ($\text{C}_2\text{H}_5\text{OH} + \text{CH}_3\text{CHO}$) was 5.1 mA cm⁻² at -0.32 V vs. RHE. Further studies indicated that CoO facilitated the formation of *CO intermediate that might undergo spill-over to MC-CNT, where the C-C coupling took place.²³¹ The pyridinic N and pyrrolic N on MC-CNT as well as the mesoporous structure may stabilise *CO species and promote C-C coupling.

4.6. Mechanism of C-C coupling for electrocatalytic CO₂RR and CORR to C₂₊ compounds

The most important step for the synthesis of C₂₊ hydrocarbons or oxygenates from CO₂ or CO is the C-C coupling. To understand how the C-C coupling occurs and how to control the C-C coupling as well as the formation of different products would be very helpful for rational design of highly selective catalysts for the formation of C₂₊ compounds.

The well-known catalytic system involving the coupling of C1 molecules is Fischer-Tropsch synthesis, i.e., the hydrogenation of CO to C₂₊ hydrocarbons, which typically proceeds on Fe-, Co- or Ru-based heterogeneous catalysts at high temperatures and pressures.⁷ The hydrogenation of CO₂ to C₂₊ hydrocarbons on related heterogeneous catalysts usually proceeds via CO intermediate, i.e., the reverse water-gas shift reaction ($\text{H}_2 + \text{CO}_2 \rightarrow \text{CO} + \text{H}_2\text{O}$) followed Fischer-Tropsch synthesis. The mechanism for Fischer-Tropsch synthesis is relatively mature. Take the formation of C₂H₄ as an example, it is accepted that the reaction proceeds through the following key elementary steps on catalyst surfaces: (1) adsorption and dissociation of CO and H₂; (2) formation of surface CH_x species; (3) C-C coupling of CH_x species; (4) hydrogenation or dehydrogenation of C₂H_x into C₂H₄ (Fig. 27a).⁷ However, the selective formation of C₂H₄ on the Fischer-Tropsch catalyst is very difficult because the C-C coupling is generally uncontrollable. Actually, the polymerisation of CH_x species to form C_nH_m with different carbon numbers, also known as the chain growth, can occur on the Fischer-Tropsch catalyst surfaces. Thus, the selectivity of products generally follows the Anderson-Schulz-Flory distribution, which is determined by the rate of chain growth and that of chain termination.⁷ According to the ideal ASF model, the maximum selectivity of C₂-C₄ (including olefins and paraffins) is only 58%. For the formation of ethanol by hydrogenation of CO over a heterogeneous catalyst, it is generally believed that both dissociated and non-dissociated CO species should exist on the catalyst surface.²⁰⁹ The formation of C₂H₅OH requires the coupling of CH_x species and *CO species, and the formed CH_xCO intermediate undergoes further hydrogenation to ethanol (Fig. 27b).

A few studies have claimed that similar to the thermocatalysis, the C-C coupling may take place between surface *CH₂ species to form C₂H₄ on Cu nanoparticles during electrocatalytic CO₂RR, and meanwhile the coupling between *CH₂ and *CO or the insertion of CO contributes to the formation of C₂H₅OH or CH₃CHO.^{199,201} However, most studies have pointed out that the electrocatalytic CO₂RR or CORR under mild conditions (typically ambient temperature and pressure) would proceed in different mechanisms.^{232-237,238} The current consensus is that CO is the key intermediate in electroreduction CO₂RR. The direct dimerization of CO₂ or activated CO₂ is very rare.¹⁵⁹ Thus, the electrocatalytic CO₂RR

to C₂₊ products proceeds via the same pathway with that for CORR after the reduction of CO₂ to CO. View Article Online DOI: 10.1039/D0EE01860K

Several possibilities have been proposed for C-C coupling of CO or CO-derived intermediates. The direct coupling of *CO to form *OCCO species followed by hydrogenation to C₂H₄ and C₂H₅OH has been proposed in most of the studies reported to date (Fig. 27c).²³²⁻²³⁴ The pathway of direct *CO dimerization has mainly been

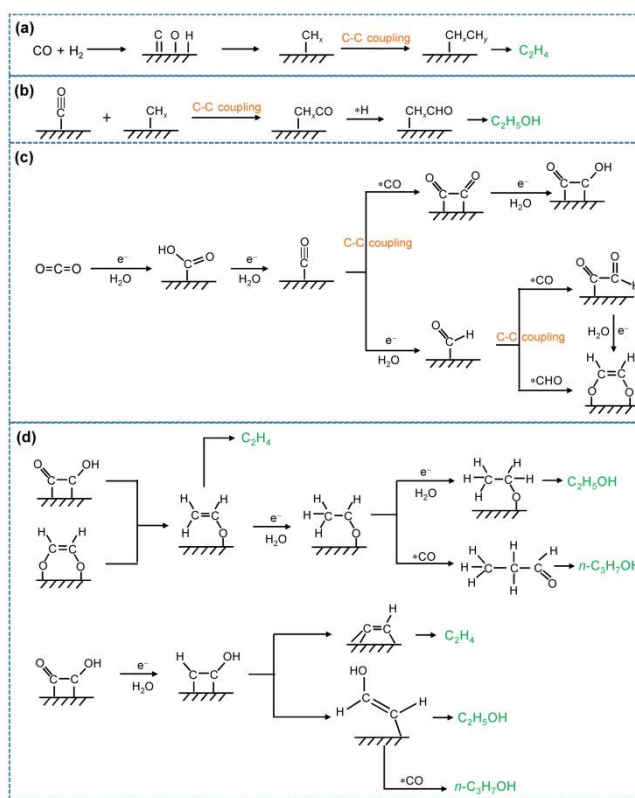


Fig. 27 (a) Mechanism for the conversion of syngas to C₂H₄ in Fischer-Tropsch synthesis. (b) Mechanism for the conversion of syngas to C₂H₅OH on thermocatalysts. (c) Three possible C-C coupling mechanisms in electrocatalytic CO₂RR. (d) Two possible mechanisms for the formation of C₂H₄, C₂H₅OH and n-C₃H₇OH.

supported by the DFT calculations. Recently, Calle-Vallejo, Koper and co-workers observed appearance of adsorbed species with vibrational bands at 1191 and 1584 cm⁻¹ in *in situ* FT-IR spectroscopic studies during CO reduction on the Cu(100) surface in LiOH electrolyte, which were assignable to the C-O-H and C=O stretching vibrations of *OCCOH species based on DFT calculations.²³⁵ The *OCCOH species was a hydrogenated CO dimer intermediate, and thus this provided evidence for the direct dimerization of *CO species. It is of interest that the *OCCOH species could not be observed on the Cu(111) surface, confirming that the coupling of CO is a structure-sensitive reaction. This result also agrees well with the fact that the Cu(100) with square symmetry is more selective for the formation of C₂₊ products.^{178,180}

On the other hand, some studies have demonstrated the importance and participation of *CHO species in the C-C coupling step (Fig. 27c).^{142,236,237,239} Nørskov and co-workers studied the kinetic barriers to the formation of a C-C bond between adsorbates

on the Cu(211) surface derived from CO using DFT calculations.²³⁶ The result demonstrated that the kinetic barriers for C-C coupling decreased significantly with the degree of hydrogenation of reacting adsorbates. It was confirmed that this trend was not affected by the electric field present during the solid-electrolyte interface. The DFT calculations offered energy barriers of 1.619, 0.675, 0.564, 0.364 and 0.203 eV for the coupling steps of (*CO + *CO), (*CO + *CHO), (*CHO + *CHO), (*CHO + *CH₂O) and (*CH₂O + *CH₂O), respectively.²³⁶ Generally, the coupling reaction with a kinetic barrier of < 0.7 eV can proceed facilely at ambient temperature. Thus, these coupling steps may occur except for the direct dimerization of *CO. It is believed that the unique feature of the electrochemical environment lies in that the chemical potential of hydrogen (electrons and protons) can be tuned by the applied potential. The computational work by Goddard III and co-workers tended to suggest that the *CHO species can be an intermediate for the formation of both CH₄ and C₂H₄.²³⁷ Bell, Head-Gorden and co-workers performed DFT calculations using an implicit electrolyte model, which enables a better simulation of the effect of an applied potential by varying on the surface to match the Fermi level to the target potential of electrode electrons, for CO₂RR on Cu(100) and Cu(111) surfaces.²³⁹ The results strongly suggest that the coupling between *CO and *CHO plays a pivotal role in the formation of C₂ compounds and *COCHO is the common intermediate for the formation of C₂H₄ and C₂H₅OH.²³⁹ Our recent work demonstrated that the coupling of (*CHO + *CHO) could also play a key role in the formation of C₂ compounds during CO₂RR on a fluoride-modified Cu catalyst, which exhibited excellent FEs and formation rates of C₂₊ compounds (C₂H₄ and C₂H₅OH).¹⁴² In situ electrochemical attenuated total reflection Fourier-transform infrared spectroscopy (ATR-FTIRS) measurements provided evidence for the generation of *CHO species on the fluoride-modified Cu surface, whereas the *CHO could not be detected on the Cu surface without fluoride modification probably due to the very low concentration.¹⁴²

Two possible mechanisms have been proposed for the formation of C₂₊ compounds including C₂H₄, C₂H₅OH and C₃H₇OH (Fig. 27d).^{127,237,239–241} Koper, Bell and co-workers proposed that after a series of protonation and electron transfer steps, the *OCCOH or *OCHCHO* species is converted to *CH₂CHO, which serves as the selectivity-determining intermediate to C₂₊ products.^{213,239–241} The hydrogenolysis of *CH₂CHO intermediate directs a pathway to C₂H₄, while the hydrogenation of *CH₂CHO results in *CH₃CHO and consequently C₂H₅OH. DFT calculations revealed that the barrier for C₂H₅OH formation via *CH₃CHO was ~0.2 eV higher than that for C₂H₄ formation via *CH₂CHO.²¹³ This may explain why higher C₂H₄ selectivity over C₂H₅OH is usually observed on Cu-based catalysts. Further, n-C₃H₇OH can be formed through a (*CH₃CHO + *CO) coupling step. Alternatively, Goddard III and co-workers suggested that the selectivity-determining intermediate may be formed earlier for the formation of different C₂₊ products.²³⁷ They proposed that the hydrogenation of *OCCOH gave *CHCOH intermediate, which was the selectivity-determining intermediate. After the formation of *CHCOH, the dehydroxylation of *CHCOH to *CCH leads to C₂H₄, whereas the hydrogenation of *CHCOH to *CHCHOH leads to C₂H₅OH.

5. Photocatalytic and electrocatalytic conversions of CH₄

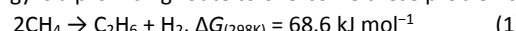
DOI: 10.1039/D0EE01860K

Methane is the major component of natural gas, shale gas, biogas and methane hydrate, and has abundant reserve and vast availability. Nowadays, CH₄ has become a major source for energy and fuels owing to its cleaner feature as compared with other fossil resources, but the chemical use of CH₄ is still insufficient.^{20,242,243} The activation and selective conversion of CH₄ is one of the most challenging goal and is regarded a "holy grail" in chemistry because of the much higher stability of CH₄ as compared to a potential target product (such as CH₃OH and C₂H₄).²⁴⁴ In the current chemical industry, the transformation of CH₄ is performed indirectly via syngas (CO/H₂), i.e., the steam reforming of CH₄ to syngas followed by conversion of syngas to CH₃OH or C₂₊ hydrocarbons by CH₃OH synthesis or Fischer-Tropsch synthesis. The steam reforming of CH₄ is a high-cost and energy-intensive process. Although a lot of efforts have been devoted to transform CH₄ directly into chemicals or liquid fuels via thermocatalysis, the selectivity of the target product is generally low at a reasonably high CH₄ conversion, because the reactive target product can undergo consecutive dehydrogenation or oxidation to carbon or CO₂ under severe conditions. Photocatalysis and electrocatalysis may provide new opportunities for the transformation of CH₄ to chemicals and fuels under mild conditions by introducing photo or electrical energy. Several review articles have been published for photocatalytic and electrocatalytic conversions of CH₄,^{55,56,245–248} but those are devoted to the photocatalytic or electrocatalytic conversion of CH₄ to C₂₊ compounds are still quite limited. Here, we focus on recent advances in the transformation of CH₄ to C₂₊ compounds via photocatalysis or electrocatalysis.

5.1. Photocatalytic conversion of CH₄ to C₂₊ compounds

Photocatalytic conversion of CH₄ alone by a non-oxidative dehydrogenation process mainly offered C₂₊ hydrocarbons. In the presence of H₂O, not only C₂₊ hydrocarbons but also C₂₊ oxygenates could be formed in CH₄ photocatalytic conversions. Some typical systems for photocatalytic coupling of CH₄ in the absence and presence of H₂O are summarized in Table 5.^{249–265}

5.1.1. Photocatalytic coupling of pure CH₄. The non-oxidative coupling of CH₄ to form C₂₊ hydrocarbons and H₂ is an attractive route for CH₄ utilisation. However, the dehydrogenation of CH₄ to C₂₊ compounds, such as C₂H₆ and benzene (eqn (1) and (2)), is generally thermodynamically unfavourable under mild conditions, and high temperatures are required to promote the equilibrium CH₄ conversion to an acceptable level by thermocatalysis. High temperatures may unavoidably lead to coke deposition. Under such circumstance, the photocatalytic conversion of CH₄ driving by solar energy is a promising route to overcome these problems.



A series of studies by Yoshida and co-workers showed that porous SiO₂ or metal oxides-loaded SiO₂ or Al₂O₃ (e.g., MgO/SiO₂, GaO_x/SiO₂, and CeO_x/Al₂O₃) could catalyse the dehydrogenative coupling of CH₄ to C₂H₆ and H₂ under UV light irradiation at mild

REVIEW

Energy & Environmental Science

temperatures.²⁴⁷⁻²⁵⁴ A SiO₂-Al₂O₃ composite evacuated at 800 °C was first reported to be active for non-oxidative coupling of CH₄ to C₂₊ hydrocarbons (including C₂H₆, C₂H₄, C₃H₈, C₃H₆, C₄H₁₀ and minor C₅₋₆) with C₂H₆ as the major product under UV-vis light irradiation by a 250 W Xe lamp at 37 °C.²⁴⁹ A later study found that the ternary composite of SiO₂-Al₂O₃-TiO₂ (Al 10 mol%, Ti 0.5 mol%) after 800 °C evacuation showed higher performance, offering a C₂H₆ yield of ~2% on a molar

carbon basis during the conversion of 200 μmol CH₄ with 1.0 g catalyst in a closed system for 3 h under UV-vis light irradiation by a 250 W Xe lamp at 37 °C.²⁵⁰ The pair site composed of dispersed AlO₄ and TiO₄ in silica matrix with Ti⁴⁺-O²⁻-Al³⁺ might function as the

Table 5 Typical photocatalytic systems for conversion of CH₄ to C₂₊ compounds

Photocatalyst	Formation rate (μmol g ⁻¹ h ⁻¹)	Quantum Efficiency (QE)	Light source	Ref.
Photocatalytic coupling of CH₄ alone				
SiO ₂ -Al ₂ O ₃	C ₂ H ₄ , 0.01; C ₂ H ₆ , 0.10; C ₃ H ₆ , 0.005; C ₃ H ₈ , 0.02; C ₄ H ₈ , 0.003; C ₄ H ₁₀ , 0.002	-	Xe lamp	249
SiO ₂ -Al ₂ O ₃ -TiO ₂	C ₂ H ₆ , 0.69; C ₃ H ₈ , 0.056	-	Xe lamp (220-300 nm)	250
FSM-16	C ₂ H ₆ , 0.09; C ₃ H ₈ , 0.003	-	Xe lamp (220-300 nm)	251
MgO/SiO ₂	C ₂ H ₆ , 0.046; C ₃ H ₈ , 0.0008	-	Xe lamp (220-300 nm)	252
Ga _x O/SiO ₂	C ₂ H ₄ , 0.005; C ₂ H ₆ , 0.11; C ₃ H ₆ , 0.002; C ₃ H ₈ , 0.002	0.01% (220-270 nm)	Xe lamp (220-300 nm)	253
Ce _x O/Al ₂ O ₃	C ₂ H ₄ , 0.053; C ₂ H ₆ , 0.24; C ₃ H ₆ , 0.038; C ₃ H ₈ , 0.0049	-	Xe lamp (220-300 nm)	254
Zn ²⁺ -ZSM-5	C ₂ H ₆ , 3.0	0.55% (300-400 nm)	high-pressure Hg lamp	255
Ga ³⁺ -ETS-10	C ₂ H ₄ , 0.61; C ₂ H ₆ , 10.89; C ₃ , 1.18; C ₄ , 0.74	-	high-pressure Hg lamp	256
Au/ZnO	C ₂ H ₆ , 11.5	0.08% (320-2500 nm)	Xe lamp (320-2500 nm)	257
Si-Doped GaN	Benzene, 55.6; Toluene, 0.5; Ethane, 3.3; Ethylene, 0.5	0.72% (290-380 nm)	Xe lamp (290-380 nm)	258
Ag-HPW-TiO ₂	C ₂ H ₆ , 23; C ₃ H ₈ , 1.2	3.5% (362 nm)	Hg-Xe lamp (280-400 nm)	259
Photocatalytic coupling of CH₄ in the presence of H₂O				
BiVO ₄	CH ₃ OH, 21; C ₂ H ₆ , 2	-	medium-pressure mercury lamp (>185 nm)	260
Beta zeolite	CH ₃ OH, 242; HCHO, 117; HCOOH, 122	-	deep UV irradiation (< 200 nm)	261
BiVO ₄ /V ₂ O ₅ /Beta zeolite	CH ₃ OH, 10.7; C ₂ H ₆ , 2.46	-	medium-pressure Hg lamp	262
Pt-TiO ₂	C ₂ H ₆ , 50.6	3.3% (254 nm)	UV lamp (254 nm)	263
Pd-TiO ₂	C ₂ H ₆ , 54.7	2.76% (254 nm)	UV lamp (254 nm)	264
Cu-0.5/PCN	CH ₃ OH, 24.5; C ₂ H ₅ OH, 106	-	Xe lamp	265

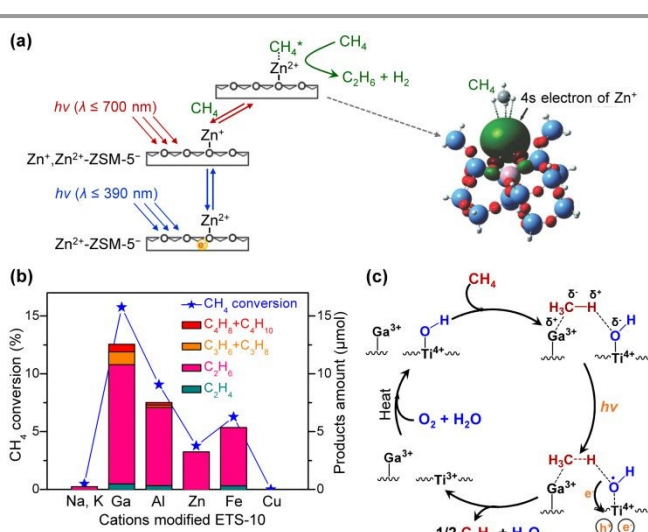


Fig. 28 (a) Schematic energy diagram for the processes of the photocatalytic conversion of CH₄ to C₂H₆ over Zn²⁺-ZSM-5 (insert: optimized geometry of the adsorbed CH₄ on Zn²⁺ active site; red: O, blue: Si, pink: Al, gray: C, white: H, and green: the 4s electron of Zn⁺).²⁵⁵ (b) Photocatalytic performance for the conversion of CH₄ over different cation-modified ETS-10 catalysts.²⁵⁶ (c) Proposed reaction mechanism for the photocatalytic conversion of CH₄ over Ga³⁺-ETS-10.²⁵⁶ Reproduced from refs. 255 and 256, with permission of Wiley-VCH Verlag GmbH&Co. KGaA, copyright 2011 and 2012.

active site. Nevertheless, pure SiO₂, in particular mesoporous silica such as MCM-41 or FSM-16 could also work for this reaction in spite of lower activity.²⁵¹ The photocatalytic sites on pure SiO₂ were proposed to be surface defect sites such as non-bridging oxygen hole sites (=Si-O•), which were generated during pretreatment at a high temperature (e.g., 800 °C) to remove surface hydroxyl groups. The photoexcitation of this site was believed to be the first step, followed by CH₄ activation to CH₃• and H• and the coupling of radical intermediates into C₂H₆ and H₂.²⁵¹ The mesoporous silica with

thinner silica wall such as FSM-16 showed better performance than that with thicker wall (MCM-41) and amorphous SiO_2 . The excitation occurred at 258 nm and thus only a part of UV light could be harnessed for this photochemical process. The highest yield of C_{2+} -hydrocarbons (~91% C_2H_6 with 8.8% C_3H_8 and minor C_2H_4) on FSM-16 (0.20 g) after 3 h reaction for 200 μmol CH_4 under UV-vis irradiation was ~0.1%.²⁵¹ The loading of MgO improved the performance of amorphous silica.²⁵² Ga_2O_3 alone exhibited much higher yield of C_2H_6 during the photocatalytic conversion of CH_4 , but the formation of H_2 was very low possibly due to the occurrence of other side-reactions such as coke deposition.²⁵³ The dispersion of Ga^{3+} on SiO_2 (0.1 mol% Ga/SiO_2) could smoothly catalyse the dehydrogenation of CH_4 to C_2H_6 and H_2 with enhanced product formation. The yield of C_2H_6 reached 0.14% after 3 h irradiation under UV-vis light, which was ~35 times higher than the pure amorphous silica.²⁵³ The bulk Ga_2O_3 could work as a semiconductor photocatalyst and thus showed high activity, but side-reactions would also occur. On the other hand, the highly dispersed tetrahedral Ga^{3+} sites on SiO_2 surfaces may function as another type of photoactive sites and the photoexcitation may take place on localised isolated sites, thus leading to the selective dehydrogenation of CH_4 to C_2H_6 and H_2 .²⁵³ Similarly, the highly dispersed Ce^{3+} sites on SiO_2 or Al_2O_3 surfaces could also accelerate the non-oxidative dehydrogenation coupling of CH_4 to C_2H_6 and H_2 .²⁵⁴

A Zn^+ -modified ZSM-5 catalyst was found to show significantly higher activity for non-oxidative coupling of CH_4 to C_2H_6 and H_2 than SiO_2 - or Al_2O_3 -based catalysts.²⁵⁵ The Zn^{2+} -ZSM-5⁻ sample, which was fabricated by a solid-vapour reaction between dehydrated H-ZSM-5 and metallic Zn vapour, contained delocalised electrons on the zeolite framework. The irradiation of Zn^{2+} -ZSM-5⁻ under UV light from a 150 W high-pressure Hg lamp led to the generation of Zn^+ as confirmed by ESR. The obtained ($\text{Zn}^+, \text{Zn}^{2+}$)-ZSM-5⁻ catalyst could work for the non-oxidative coupling of CH_4 to C_2H_6 and H_2 under either UV or sunlight irradiation. The formation rate of C_2H_6 was 9.8 $\mu\text{mol h}^{-1} \text{g}^{-1}$ under UV-light irradiation from high-pressure Hg lamp. Almost equimolar amount of H_2 was formed and the selectivity of C_2H_6 was close to 100%. The conversion of 200 μmol CH_4 with 1.0 g ($\text{Zn}^+, \text{Zn}^{2+}$)-ZSM-5⁻ catalyst offered a 17.5% C_2H_6 yield in 24 h UV-light irradiation, and the quantum efficiency was around 0.55%.²⁵⁵ The highest CH_4 conversion reached 23.8% with 99% C_2H_6 selectivity under optimised conditions. Further studies suggested a two-stage mechanism (Fig. 28a): (1) the generation of ($\text{Zn}^+, \text{Zn}^{2+}$)-ZSM-5⁻ in the first stage that required irradiation by UV light of 278–390 nm; (2) the dehydrogenative coupling of CH_4 by the ($\text{Zn}^+, \text{Zn}^{2+}$)-ZSM-5⁻ catalyst that could work under visible light of < 700 nm.²⁵⁵

A latter study from the same group found that the Ga^{3+} -modified zeolite ETS-10, which was a microporous titanosilicate with a framework containing one-dimensional O-Ti-O-Ti-O semiconducting nanowires (diameter, 0.67 nm) insulated from each other by the surrounding SiO_2 matrix, could work for photocatalytic dehydrogenative coupling of CH_4 , offering a CH_4 conversion rate of 29.8 $\mu\text{mol g}^{-1} \text{h}^{-1}$, which was about 3 times higher than that of ($\text{Zn}^+, \text{Zn}^{2+}$)-ZSM-5⁻.²⁵⁶ The ETS-10 samples containing exchanged cations of Ga^{3+} , Al^{3+} , Zn^{2+} and Fe^{3+} were all active, and the Ga^{3+} -ETS-10 catalyst was the most efficient for photocatalytic conversion of CH_4 (Fig. 28b). During the conversion of 200 μmol CH_4 with 0.2 g catalyst in a closed system, CH_4 conversion reached 14.9% with C_2H_6

selectivity of 70% after 5 h irradiation under UV light from a high-pressure Hg lamp.²⁵⁶ Other products included C_2H_4 , C_3H_8 , C_3H_6 , C_4H_{10} and C_4H_8 . The catalyst was also efficient for photocatalytic conversion of C_2H_6 , offering C_4H_{10} with a selectivity of 57% at C_2H_6 conversion of 11% after 5 h of reaction. Ga^{3+} was found to be a key to the reaction, but the Ga^{3+} -ZSM-5 and Ga^{3+} -Y catalyst only showed very poor performances for photocatalytic conversion of CH_4 . Therefore, the Ga^{3+} ions and TiO_2 -wire units in the ETS-10 framework both played crucial roles in photocatalytic conversion of CH_4 . The in-depth studies by Chen and co-workers indicated a dual active site mechanism (Fig. 28c).²⁵⁶ In other words, the extraframework metal cation (Ga^{3+}) and the Ti^{4+} -OH group on the titanate wire interacted

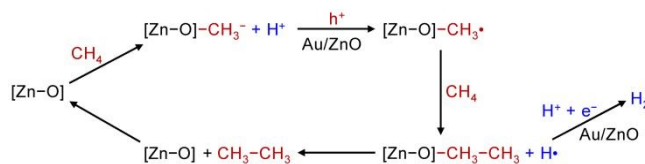


Fig. 29 Proposed reaction mechanism for photocatalytic conversion of CH_4 over plasmonic Au/ZnO catalyst.²⁵⁷

synergistically under UV-light irradiation, leading to the cleavage of C-H bond in CH_4 . Probably, CH_4 was adsorbed and polarized through the interaction between Ga^{3+} and methyl group to weaken the C-H bond, and then the hydrogen abstraction from CH_4 took place by the $\bullet\text{OH}$ radical in the vicinity generated by photoexcitation of the surface Ti-OH species. C_2H_6 is formed through the C-C coupling of two CH_3 surface species or radicals.

Semiconductor-based photocatalysts have also been examined for non-oxidative photocatalytic conversion of CH_4 to C_{2+} compounds.^{257,258,266} Long and co-workers fabricated a plasmonic photocatalyst consisting of Au nanoparticles and ZnO nanosheets with exposed (001) facets.²⁵⁷ C_2H_6 and H_2 with formation rates of about 11 and 10 $\mu\text{mol g}^{-1} \text{h}^{-1}$ could be achieved on the optimized Au/ZnO catalyst under simulated solar-light irradiation, and the solar-to- C_2H_6 energy conversion efficiency was 0.08%. It was proposed that the strong polarisation of (001) facet of ZnO nanosheets would promote the polarization and activation of the C-H bond of CH_4 . Meanwhile, the SPR effect of Au nanoparticles offered photogenerated holes and electrons for the reduction of H^+ to H atom to give H_2 and the oxidation of CH_3^- to $\text{CH}_3\bullet$, which coupled to produce C_2H_6 (Fig. 29).

Li and co-workers found that GaN nanowires with a 3% top *c*-plane and 97% lateral *m*-plane showed high selectivity of C_6H_6 during non-oxidative photocatalytic conversion of CH_4 under UV light irradiation at room temperature.²⁵⁸ The selectivity of C_6H_6 in hydrocarbon products was about 97% and H_2 was also formed with a ratio of benzene to H_2 of 1:9, in agreement with the stoichiometry (eqn (2)). Further studies with GaN samples with different morphologies and different fractions of exposed facets revealed that the reaction was structure sensitive (Fig. 30a). The analysis of results indicated that the lateral *m*-plane, which was composed of Ga^{3+} and N^{3-} tetrahedrally coordinated with each other, contributed to CH_4

REVIEW

Energy & Environmental Science

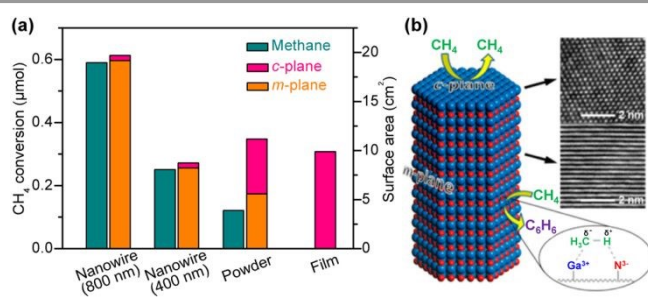


Fig. 30 (a) Photocatalytic conversion of CH₄ over GaN catalysts with different morphologies and different exposed surface areas of *m*-plane.²⁵⁸ (b) Schematic diagram for CH₄ C-H bond polarization on the *m*-plane of GaN.²⁵⁸ Reproduced from ref. 258, with permission of the American Chemical Society, copyright 2014.

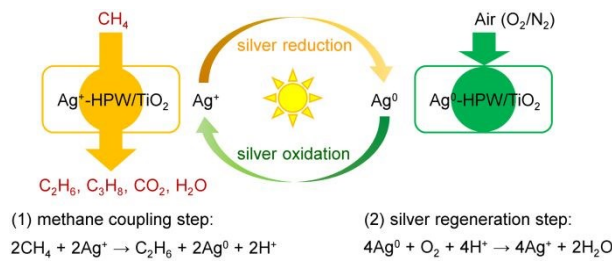


Fig. 31 Schematic illustration of photochemical looping process for coupling of CH₄ to C₂H₆.²⁵⁹

conversions, whereas the *c*-place made up of only Ga or N atoms had no contribution to the photocatalytic conversion of CH₄ (Fig. 30b). Mechanistic studies suggested that the Ga³⁺ and N³⁻ on *m*-plane could interact with CH₄, leading to polarisation of H⁺–CH₃^{δ-} and heterolytic dissociation of CH₄. The photogenerated electrons and holes would function for the reduction and oxidation of H⁺ and CH₃^{δ-} to H[•] and CH₃[•], respectively. The coupling of radical intermediates could give H₂ and C₂H₆, and benzene was formed by the dehydrogenation of C₂H₆ to C₂H₄, followed by cyclization and dehydrogenation processes (Fig. 30b).²⁵⁸

Very recently, Khodakov and co-workers reported an interesting photochemical looping strategy for CH₄ conversion to C₂H₆ over a silver–phosphotungstic acid–titania nanocomposites (Ag-HPW/TiO₂) photocatalyst.²⁵⁹ When a batch photo-reactor was used, the selectivity of C₂H₆ could reach 90% with small amounts of C₃H₈ and CO₂, and the C₂H₆ yield was lower than 0.1%. The yield of C₂H₆ could reach 9% after 5 h irradiation in a capillary photo-reactor with a C₂H₆ selectivity of ~55%. It was proposed that the photochemical looping involved two importance steps, i.e., CH₄ coupling step and silver regeneration step (Fig. 31).²⁵⁹ During the CH₄ coupling step, C₂H₆ was formed through oxidative coupling by photogenerated holes, while the photogenerated electrons were responsible for the reduction of cationic Ag⁺ to metallic Ag⁰. Ag⁰ was then re-oxidized to Ag⁺ under light irradiation in the presence of air in the silver regeneration step. The cationic Ag⁺ dispersed in the HPW layer over Ag-HPW/TiO₂ was essential for the coupling of CH₄ to C₂H₆.

5.1.2. Photocatalytic coupling of CH₄ in the presence of H₂O. Early studies reported that the photocatalytic conversion of CH₄ in the presence of H₂O or an oxidant could provide C₁ oxygenates, in particular CH₃OH, using WO₃, La³⁺-doped WO₃ and BiVO₄

semiconductor photocatalysts.^{260,267–269} In these systems, photogenerated holes were considered to oxidize H₂O to •OH, which then participated in the activation of CH₄ to CH₃[•], eventually giving CH₃OH as the major product. Pure silica zeolite could also catalyse the conversion of CH₄ to CH₃OH under deep ultraviolet light ($\lambda = 165$ or 185 nm) irradiation.²⁶¹ Beta zeolite could offer a selectivity of C₁ oxygenates (including CH₃OH, HCHO and HCOOH) of 95% at CH₄ conversion of 13%. It was speculated that the surface ≡Si-OH was activated by deep UV light irradiation to ≡Si-O• and H•, and the ≡Si-O• functioned for the activation of CH₄ to CH₃[•], followed by the transformation of CH₃[•] to CH₃OH. Actually, the formation of C₂ products, mainly C₂H₆, which can be formed via the coupling of CH₃[•], have also been observed in some of these systems using

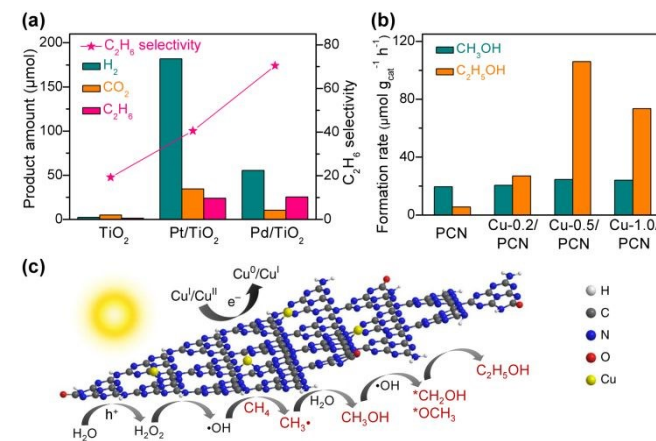


Fig. 32 (a) Photocatalytic conversion of CH₄ over TiO₂, Pt/TiO₂ and Pd/TiO₂.^{263,264} (b) Photocatalytic conversion of CH₄ over Cu-X/PCN photocatalysts with different amounts of Cu.²⁶⁵ (c) Proposed mechanism for photocatalytic conversion of CH₄ with H₂O over Cu-0.5/PCN.²⁶⁵ Reproduced from ref. 265, with the permission of Springer-Nature, copyright 2019.

semiconductor- or zeolite-based catalysts.^{260,261} The formation rate of C₂H₆ could reach 10 μmol g⁻¹ h⁻¹ on a beta zeolite under light irradiation by a medium-pressure Hg lamp, and the loading of V₂O₅ or BiVO₄/V₂O₅ heterojunction could shift the product to CH₃OH.²⁶²

Pt- or Pd-loaded semiconductor TiO₂ was reported to catalyse the conversion of CH₄ to C₂H₆ in aqueous medium under UV-light irradiation.^{263,264} H₂ and CO₂ were also formed with considerable amounts. The studies using electron or hole scavenger suggested that H₂ was formed by photogenerated electrons, while holes participated in the formation of C₂H₆ and CO₂. The selectivity of C₂H₆ was quite low on TiO₂ alone because of the formation of large fraction of CO₂ from CH₄. The loading of Pt or Pd not only enhanced H₂ formation but also improved the formation rate and the selectivity of C₂H₆ (Fig. 32a).^{263,264} It is of interest that although Pd is not as efficient as Pt in promoting H₂ formation, it is more suitable for the formation of C₂H₆. The C₂H₆ selectivity and CH₄ conversion quantum efficiency could reach 73% and 2.8% over the Pd/TiO₂ catalyst, respectively.²⁶⁴ Electron spin resonance (ESR) spectroscopy studies showed the generation of •OH and CH₃[•] radicals. Thus, the •OH species generated by the oxidation of H₂O by photoexcited holes was proposed to be responsible for abstracting hydrogen atom from CH₄ to generate CH₃[•], the coupling of which afforded C₂H₆. Although it

Energy & Environmental Science

was assumed that Pd nanoparticles on TiO₂ surfaces might participate in the activation of C-H bond of CH₄,²⁶⁴ there was no evidence to support this hypothesis.

To design a photocatalytic system that can generate •OH with controllable manner could be beneficial to the conversion of CH₄. Wang and co-workers recently reported that a Cu-modified polymeric carbon nitride (PCN) catalyst could work for photocatalytic conversion of CH₄ and H₂O to C₂H₅OH under UV-vis light irradiation.²⁶⁵ PCN with a bandgap of 2.97 eV and valence band position of 1.82 eV can work for the oxidation of H₂O to H₂O₂ but not to •OH. The control experiment for photocatalytic conversion of H₂O on PCN confirmed the formation of H₂O₂. The photocatalytic conversion of CH₄ on PCN led to the formation of CH₃OH as a major product together with a small amount of C₂H₅OH. The loading of Cu onto PCN from 0 to 0.5% significantly increased the formation rate of C₂H₅OH from 5.5 to 106 μmol g⁻¹ h⁻¹, whereas the formation rate of CH₃OH remained almost unchanged (20–25 μmol g⁻¹ h⁻¹) (Fig. 32b).²⁶⁵ The Cu sites could accelerate the decomposition of H₂O₂ to •OH radicals and the oxidised Cu⁺ or Cu²⁺ could be reduced by photogenerated electrons. The Cu sites might also function for the adsorption and activation of CH₄ to help the formation of CH₃• by the •OH species. The synergistic effect between the Cu sites and the adjacent C atom in PCN has been proposed to play key roles in the formation of C₂ product. To understand the mechanism for C-C coupling would be very helpful for the design of more efficient photocatalytic systems for the conversion of CH₄ to C₂ compounds. Wang and co-workers considered that C₂H₅OH was formed via CH₃OH intermediate on the Cu/PCN catalyst and the C-C coupling might proceed through hydroxymethyl and methoxy species formed by interaction of CH₃OH with •OH radical (Fig. 32c).²⁶⁵ However, this mechanism is too speculative and there exist many other possibilities. Considering that Cu-based catalysts show interesting performances also in C-C coupling of C1 intermediates from CO₂/CO during photocatalysis or electrocatalysis, further studies on the Cu-based CH₄ photocatalytic conversion are definitely needed in the future.

5.2. Electrocatalytic conversion of CH₄ to C₂₊ compounds

The electrocatalytic partial oxidation of CH₄ could produce C1 (such as CH₃OH, HCHO) or C₂₊ (such as C₂H₆, C₂H₄) compounds.^{54,55,246,270,271}

Table 6 Typical electrocatalytic systems for conversion of CH₄ to C₂₊ compounds

Catalyst	Reaction condition	E (V)	j (mA cm ⁻²)	CH ₄ conv. (%)	C ₂₊ selectivity (%)	C ₂₊ yield (%)	Ref.
Bi ₂ O ₃ -Ag	SOE, CH ₄ O ₂ , 700 °C	1.3 ^a	-	-	C ₂ H ₄ + C ₂ H ₆ : 47	-	272
porous Ag	SOE, CH ₄ O ₂ , 800 °C	-	5	97	C ₂ H ₄ + C ₂ H ₆ : 91	88	273
Mn-Ce-Na ₂ WO ₄ /SiO ₂	SOE, CH ₄ O ₂ , 800 °C	-	470	61	C ₂ H ₄ : 36; C ₂ H ₆ : 6.2	23	274
Ag	SOE, CH ₄ H ₂ O, 820 °C	-	400	26	C ₂ H ₄ : 26; C ₂ H ₆ : 4.3	8	275
Ag + Ce-Na ₂ WO ₄ /SiO ₂	SOE, CH ₄ H ₂ O, 800 °C	-	150	23	C ₂ H ₄ : 44; C ₂ H ₆ : 17	13	276
Ag + SrZr _{0.95} Y _{0.05} O ₃	SOE, CH ₄ H ₂ O, 720 °C	-	250	18	C ₂ H ₄ : 21; C ₂ H ₆ : 21	7.6	277
Ag + Mn-Ce-Na ₂ WO ₄ /SiO ₂	SOE, CH ₄ H ₂ O, 800 °C	-	70	34	C ₂ H ₄ : 36; C ₂ H ₆ : 7.4	15	278
0.075Fe-Sr ₂ Fe _{1.5} Mo _{0.5} O _{6-δ}	SOE, CH ₄ O ₂ , 850 °C	1.6 ^a	1000	41	C ₂ H ₄ + C ₂ H ₆ : 82	33	279
0.075Fe-Sr ₂ Fe _{1.5} Mo _{0.5} O _{6-δ}	SOE, CH ₄ CO ₂ , 850 °C	1.6 ^a	750	14	C ₂ H ₄ + C ₂ H ₆ : 76	10	279
Co ₃ O ₄ /ZrO ₂	Na ₂ CO ₃ as the electrolyte, CH ₄ H ₂ O, RT	2.0 ^a	8.7	40	1-propanol: 31; 2-propanol: 30	24	280

Previous studies tend to suggest that the major useful products obtained from low-temperature electrocatalytic reaction system were C1 derivatives, whereas useful C₂₊ compounds could be formed at high temperatures (> 600 °C).^{270,271} Some typical electrocatalysts and performances are summarized in Table 6.²⁷²⁻²⁸³

The oxidative coupling of methane (OCM) to C₂ compounds

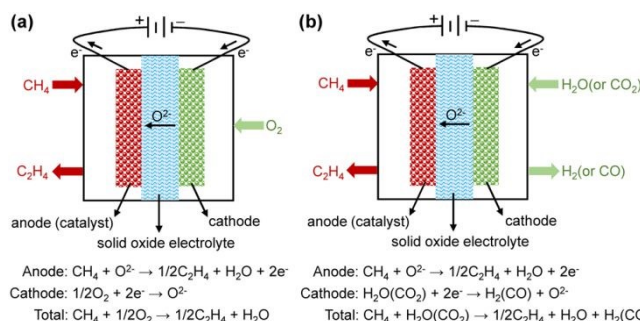


Fig. 33 (a) Schematic illustration of solid oxide electrolyte reactor for O₂/CH₄ conversion. (b) Schematic illustration of solid oxide electrolyte reactor for H₂O/CH₄ or CO₂/CH₄ conversion.

(mainly C₂H₆ and C₂H₄) is a well-known thermocatalytic reaction for CH₄ transformation at high temperatures.^{20,242,243} The selectivity of C₂H₆ and C₂H₄ usually decreases with an increase in the conversion of CH₄, thus limiting the C₂ yield. It is generally accepted that the molecular oxygen in the gas phase would lead to the formation of CO and CO₂, whereas the oxygen species on catalyst surfaces are responsible for the OCM reaction.^{20,242,243} To suppress the gas-phase non-selective oxidation of CH₄, the O₂ concentration in the gas phase should be minimized. The solid oxide electrolyte electrochemical reactor, which uses oxygen ion conductors as the electrolyte, has been harnessed for the electrocatalytic oxidation of CH₄ with the aim to improve the selectivity of C₂ products. This electrochemical reactor provides an oxidant through transferring oxygen ion from cathode side to the anode side, and thus can avoid the co-feeding of CH₄ and O₂. An electrocatalytic reactor with solid oxide electrolyte (SOE) mainly consists of two porous electrodes (i.e., anode and cathode) and a dense SOE to separate cathode and anode compartments (Fig. 33). The anode compartment is usually fed with

REVIEW

Energy & Environmental Science

ZrO ₂ :NiCo ₂ O ₄	Na ₂ CO ₃ as the electrolyte, CH ₄ H ₂ O, RT	2.0 ^a	2.3	48	propionic acid: 65 C ₂ H ₅ OH: 85 (FE)	31 View Article Online DOI: 10.1039/D0EE01860K	281
NiO@NiHF	NaOH as the electrolyte, CH ₄ H ₂ O, RT	1.5 ^b	0.04		C ₂ H ₅ OH: 89 (FE)		282
NiO/Ni	proton exchange membrane, CH ₄ H ₂ O, RT	1.4 ^b	3.0 mA g _{NiO} ⁻¹		C ₂ H ₅ OH: 89 (FE) 25 μmol g _{NiO} ⁻¹ h ⁻¹ (formation rate)		283

^aThe potential represents the full-cell potential (V); ^bThe potential refers to RHE; RT: room temperature.

CH₄, while the cathode compartment can be fed either with O₂ (Fig. 33a) or another reactant (e.g., H₂O or CO₂) that is capable of providing oxygen ion (Fig. 33b). It is noteworthy that the feeding of H₂O or CO₂ can simultaneously produce H₂ or CO.

Otsuka and co-workers reported a pioneering work for CH₄ coupling in a SOE electrocatalytic reactor in 1985.²⁷² A Y₂O₃-stabilized ZrO₂ (YSZ) with high oxygen ion conductivity was used as solid oxide electrolyte, and Ag and Bi₂O₃-Ag were used as anode catalysts for electrocatalytic conversion of CH₄ at 700 °C. CH₄ and O₂ were fed in anode and cathode compartments separately (Fig. 33a). The oxygen transfer flux through the YSZ could be controlled by the externally applied potential. The CH₄ conversion rate increased with an increase in oxygen flux over Ag and Bi₂O₃-Ag catalysts, but the selectivity of C₂ compounds (C₂H₄ and C₂H₆) decreased upon increasing the oxygen flux. The Bi₂O₃-Ag catalyst reached a maximum C₂ formation rate of ~1.85 μmol min⁻¹ (selectivity, 47%) at an oxygen flux of 12 μmol min⁻¹, whereas the C₂ formation rate was only 0.42 μmol min⁻¹ (selectivity, 30%) at the same oxygen flux over the Ag catalyst (Fig. 34a).

After that, many catalysts and reaction systems based on the SOE electrocatalytic reactor have been developed.^{273,274,284,285} Vayenas and co-workers developed a reaction system with product separation and CH₄ recycling abilities for electrocatalytic conversion of CH₄ to C₂ hydrocarbons.²⁷³ The C₂ hydrocarbons could be separated by molecular sieve trap, thus significantly inhibiting the over-oxidation of C₂ hydrocarbons and improving the total yield of C₂ hydrocarbons (Fig. 34b). Over a porous Ag catalyst, at an applied current density of 5 mA cm⁻² at 800 °C, CH₄ was oxidatively coupled to C₂ hydrocarbons with a C₂ hydrocarbons yield of 88% and a C₂H₄ yield of 85%. Some typical OCM catalysts in thermocatalysis, such as Mn/Na₂WO₄/SiO₂ and La-doped SrTiO₃, were also examined for the electrocatalytic conversion of CH₄ to C₂ hydrocarbons.^{274,284,285} Tang and co-workers integrated a Mn-Ce-Na₂WO₄/SiO₂ catalyst with SOE tubular membrane reactor for electrocatalytic coupling of CH₄.²⁷⁴ The reaction could be operated at a high applied current density of 470 mA cm⁻² at 800 °C with a CH₄ single-pass conversion of 61% and C₂₊ selectivity of 42%. The C₂₊ selectivity still needs to be improved.

The oxygen for electrocatalytic oxidation of CH₄ could be provided by H₂O instead of O₂, enabling the simultaneous formation of H₂ and C₂ hydrocarbons (C₂H₄ and C₂H₆).^{275-278,286,287} Single-chamber reactor configuration with Ag/YSZ/Pt (anode/solid electrolyte/cathode) co-fed with CH₄ and H₂O mixture was reported

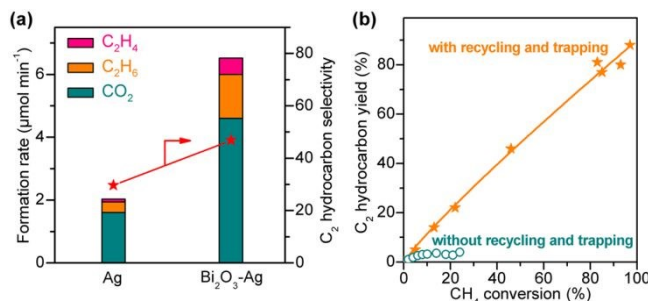


Fig. 34 (a) Electrocatalytic conversion of CH₄ over Ag and Bi₂O₃-Ag catalysts at the same oxygen flux of 12 μmol min⁻¹.²⁷² (b) Catalytic performances of porous Ag catalyst without and with C₂ hydrocarbons trapping and gas recycling.²⁷³

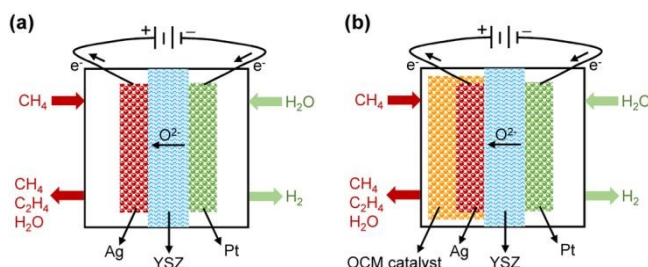


Fig. 35 Schematic diagram of O₂-conducting solid oxide electrolyte reactor. (a) Without OCM catalyst. (b) with OCM catalyst.

to show a maximum C₂ yield of ~8% under optimised conditions at 820 °C.²⁷⁵ The addition of 5 wt% Ce-5wt% Na₂WO₄/SiO₂ to the single-chamber Ag/YSZ/Pt reactor could enable thermocatalytic oxidation of CH₄ by the O₂ released to gas phase, enhancing the C₂ yield to 13% at 800 °C.²⁷⁶ The double-chamber reactor with CH₄ and H₂O vapours fed separately to the anode and cathode chambers has the potential to obtain higher C₂ selectivity. In the double-chamber reactor with Ag/YSZ/Pt configuration (Fig. 35a), Stoukides and co-workers obtained a C₂ yield of 5.7% at 840 °C at CH₄ conversion of 16.2% and C₂ selectivity of 35.1%.²⁷⁷ Although O₂ was not co-fed with CH₄, some excess oxygen ions electrochemically pumped from to anode may form O₂ and evolve to the CH₄ stream, leading to the gas-phase non-selective oxidation of CH₄. To enhance the selective oxidation of CH₄ on anode surfaces, a layer of OCM catalyst was deposited on the top of anodic electrode (Fig. 35b). When a perovskite OCM catalyst (SrZr_{0.95}Y_{0.05}O_{3-a}) was deposited, the C₂ yield was improved to 7.6% with a CH₄ conversion of 18% and C₂ selectivity of 42.2%, and reaction temperature could decrease to 720 °C.²⁷⁷ In a Ag/YSZ/Ag double-channel reactor, the addition of the Mn-Ce-Na₂WO₄/SiO₂ catalyst could promote the C₂ yield to 15% at 800 °C.²⁷⁸

CO_2 could also be used as the source of oxygen for the electrocatalytic oxidation of CH_4 . Xie and co-workers reported simultaneous electrocatalytic reduction of CO_2 to CO on the cathode and the oxidation of CH_4 on the anode (Fig. 36a).^{279,288} The utilisation of a redox-reversible layered perovskite, i.e., $\text{Sr}_2\text{Fe}_{1.5}\text{Mo}_{0.5}\text{O}_{6-\delta}$ (SFMO), as the anode and the in situ construction of metal/oxide interfaces at nanoscale using $\text{Sr}_2\text{Fe}_{1.5+x}\text{Mo}_{0.5}\text{O}_{6-\delta}$ ($x = 0\text{--}0.1$) to grow iron nanoparticles on SFMO scaffold ($x\text{Fe-SFMO}$) were demonstrated to be an efficient approach for the electrocatalytic oxidation of CH_4 to C_2 compounds by oxygen from CO_2 .²⁷⁹ A $\text{La}_{0.9}\text{Sr}_{0.1}\text{Ga}_{0.8}\text{Mg}_{0.2}\text{O}_{3-\delta}$ (LSGM) was used as the solid electrolyte and $\text{Ce}_{0.5}\text{Sm}_{0.2}\text{O}_{2-\delta}$ (SDC) was mixed with $x\text{Fe-SFMO}$ to fabricate a single cell composed of $x\text{Fe-SFMO-SDC/LSGM/SFMO-SDC}$ (anode/solid electrolyte/cathode). DFT calculation suggested that the Fe-SFMO metal-oxide interface favoured the cleavage of C-H bond of CH_4 with a lower energy barrier than the SFMO alone (Fig. 36b). Such a metal/oxide interface structure also improved the coking resistance and the thermal stability. The 0.075Fe-SFMO showed the best catalytic performances at an applied voltage of 1.6 V and a temperature of 850 °C (Fig. 36c,d).²⁷⁹ When O_2 was fed to the cathode, the conversion of CH_4 , selectivity and yield of C_2 products (C_2H_4 and C_2H_6) could reach 41%, 81.2% and 33%, respectively (Fig. 36c). The conversion of CH_4 ,

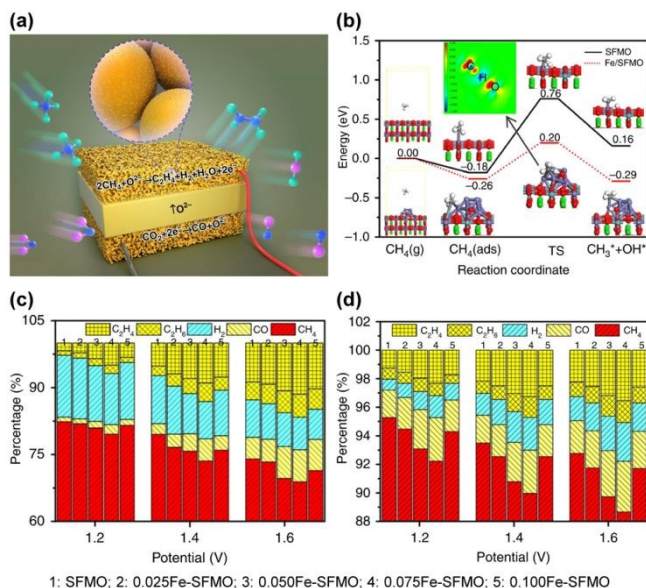


Fig. 36 (a) Schematic diagram of electrocatalytic conversion of CH_4 on the anode and reduction of CO_2 on the cathode. (b) Energy diagrams for adsorption and C-H bond cleavage of CH_4 on SFMO (001) and Fe/SFMO (001) surfaces including their initial, transition and final states. Inset: electronic charge density difference for the transition state of Fe/SFMO (001). (c) Anodic product concentrations of $x\text{Fe-SFMO}$ catalysts in the electrocatalytic conversion of CH_4 on the anode and O_2 feeding on the cathode. (d) Anodic product concentrations of $x\text{Fe-SFMO}$ catalysts in the electrocatalytic conversion of CH_4 on the anode and reduction of CO_2 on the cathode.²⁷⁹ Reproduced from ref. 279, with the permission of Springer-Nature, copyright 2019.

selectivity and yield of C_2 products were 13.7%, 75.6% and 10.3%, respectively, as CO_2 was fed to the cathode (Fig. 36d). The decreased performance in the case of electrocatalytic conversion of $\text{CH}_4\text{--CO}_2$ as compared to that of $\text{CH}_4\text{--O}_2$ may probably arise from the higher thermodynamic and kinetic barriers for CO_2 electrolysis than O_2

splitting to generate oxygen ions on the cathode. The simultaneous electrocatalytic conversion of CH_4 and CO_2 to C_2H_4 and CO is an interesting and challenging direction and is worth further study.

The studies on electrocatalytic conversion of CH_4 to C_2 -compounds under mild conditions are rare. Park and co-workers claimed that CH_4 could be electrocatalytically oxidized to C_2 -alcohols, acids and ketones at ambient temperature.^{280,281} It is very surprising that 2-propanol and 1-propanol were obtained as major products when a $\text{Co}_3\text{O}_4/\text{ZrO}_2$ nanocomposite loaded on carbon paper (Alfar) was employed as the anode for CH_4 oxidation with Na_2CO_3 as the electrolyte and Pt as the cathode for H_2O reduction (Fig. 37a).²⁸⁰ Acetaldehyde was formed at shorter times and was proposed to be the precursor for the formation of 2-propanol and 1-propanol. When a $\text{ZrO}_2\text{:NiCo}_2\text{O}_4$ quasi-solid solution catalyst loaded on graphite foil was used as the anode for the oxidation of CH_4 , propionic acid was obtained as the major products along with 2-propanol, 1-propanol, acetone and acetic acid. The conversion of CH_4 could reach 47.5% after 20 h of reaction and the formation rate of propionic acid was $1173 \mu\text{mol g}_{\text{cat}}^{-1} \text{ h}^{-1}$ (selectivity ~65%) at ambient temperature operated in a two-electrode system at 2.0 V versus Pt counter electrode.²⁸¹ The reaction-time-course studies suggested that 1-propanol, acetaldehyde and 2-propanol were the major products in the first 5 h of reaction, and these products were further oxidized to

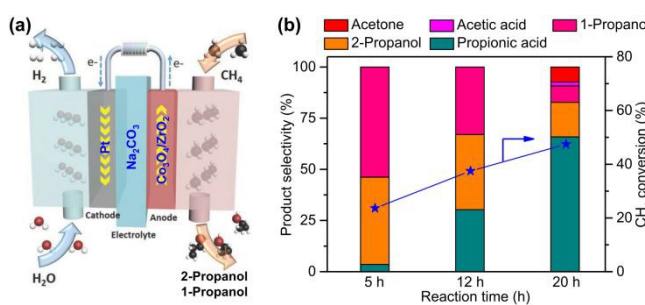


Fig. 37 (a) Schematic reaction processes for electrocatalytic conversion of CH_4 .²⁸⁰ (b) Catalytic performances of $\text{ZrO}_2\text{:NiCo}_2\text{O}_4$ quasi-solid solution catalyst for electrocatalytic conversion of CH_4 to C_2 -compounds.²⁸¹ Reproduced from ref. 280, with permission of Wiley-VCH Verlag GmbH&Co. KGaA, copyright 2017.

propionic acid, acetic acid and acetone in 20 h of reaction, respectively (Fig. 37b). Although the phenomenon that the electrocatalytic conversion of CH_4 could offer C_2 -alcohols, acids and ketones (with C_3 alcohols or acids as the major products) at room temperature is very interesting, some solid evidence, such as $^{13}\text{CH}_4$ -labelling isotopic experimental results, is expected to further confirm these very surprising results obtained in the oxidation of CH_4 with such kind of carbon-containing catalyst systems.

Recently, Chen, Sun and co-workers reported that CH_4 could be converted to $\text{C}_2\text{H}_5\text{OH}$ with high selectivity by electrocatalytic oxidation over a NiO/Ni catalyst.^{282,283} They constructed catalysts with a series of NiO/Ni interface (Fig. 38a) by controlling the calcination temperature of Ni foam.²⁸³ The 3.0NiO/Ni catalyst calcined at 500 °C with a NiO content of 3.0 wt% showed the best performance. At an applied potential of 1.4 V vs. RHE, the FE and formation rate of $\text{C}_2\text{H}_5\text{OH}$ reached 89% and $25 \mu\text{mol g}_{\text{NiO}}^{-1} \text{ h}^{-1}$, respectively.²⁸³ The optimised NiO/Ni interface with appropriate NiO content showed the balanced charge transfer ability and the highest

REVIEW

Energy & Environmental Science

electrochemically active surface area, thus enabling the efficient C–H activation and C–C coupling. DFT calculations further demonstrated a thermodynamically favourable route on NiO(200)/Ni(111) interface for $\text{C}_2\text{H}_5\text{OH}$ formation with the elementary steps of $\text{CH}_4^* \rightarrow \text{CH}_3^* + \text{H}^*$, $\text{CH}_3^* \rightarrow \text{CH}_2^* + \text{H}^*$, $\text{CH}_2^* + \text{OH}^* \rightarrow \text{CH}_2\text{OH}^*$ and $\text{CH}_3^* + \text{CH}_2\text{OH}^* \rightarrow \text{C}_2\text{H}_5\text{OH}^*$ in sequence (Fig. 38b).²⁸³ The NiO(200)/Ni(111) interface favours the dissociation of CH_4^* to CH_3^* with a relatively low activation barrier (0.30 eV). Although the steps of CH_3^* to CH_2^* and CH_3OH^* had similar activation barriers, the exothermic reaction

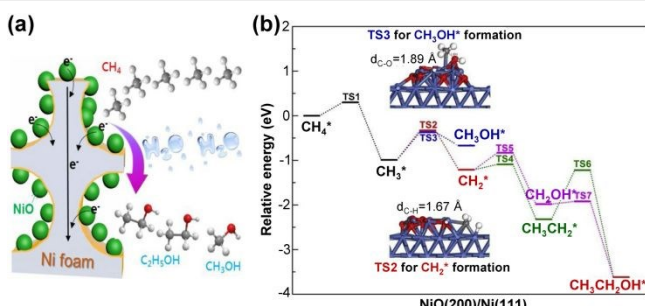


Fig. 38 (a) Schematic illustration of electrocatalytic conversion of CH_4 to $\text{C}_2\text{H}_5\text{OH}$ on NiO/Ni interface. (b) Reaction energy profiles for electrocatalytic conversion of CH_4 to CH_3OH and $\text{C}_2\text{H}_5\text{OH}$ at $\text{NiO}(200)/\text{Ni}(111)$ interface from DFT calculations.²⁸³ Reproduced from ref. 283, with permission of Elsevier, copyright 2020.

energy of CH_3^* to CH_2^* was significantly lower than that of CH_3^* to CH_3OH^* . This may be the main reason for the low CH_3OH selectivity observed over the NiO/Ni catalyst. The subsequent hydroxylation of CH_2^* and the C–C coupling of CH_3^* and CH_2OH^* to $\text{C}_2\text{H}_5\text{OH}^*$ are both more energy favourable steps.

5.3. Mechanism of C–C coupling for photocatalytic and electrocatalytic conversions of CH_4 to C_{2+} compounds

Many studies have been devoted to the transformation of CH_4 by thermocatalysis.⁵⁶ For the oxidative coupling of methane (OCM) at high temperatures (typically 873–1073 K), gas-phase methyl radical ($\text{CH}_3\bullet$) has long been proposed as the key intermediate for the C–C coupling into C_2H_6 , which undergoes dehydrogenation to C_2H_4 . The generation of $\text{CH}_3\bullet$ during OCM was confirmed by synchrotron VUV photoionization mass spectroscopy.²⁸⁹ $\text{CH}_3\bullet$ has also been proposed as the

intermediate for the C–C coupling of CH_4 to C_2H_6 in photocatalysis,^{251,256–258,264} and the formation of $\text{CH}_3\bullet$ has been detected by in situ electron spin resonance (ESR) spectroscopy.²⁶⁴ The selectivity of C_2H_4 is lower by photocatalysis. This is probably because the dehydrogenation of C_2H_6 becomes difficult at low temperatures used for photocatalysis. $\text{C}_2\text{H}_5\text{OH}$ could also be formed by photocatalytic conversion of CH_4 on a Cu/PCN catalyst, and CH_3OH was proposed to be the intermediate.²⁶⁵ However, this mechanism still lacks solid evidence. On the other hand, in the electrocatalytic CH_4 transformations, C_2H_4 and C_2H_6 could be obtained at high temperatures,^{272,273,279} whereas 1-propanol and $\text{C}_2\text{H}_5\text{OH}$ may be obtained at low temperatures.^{280–283} The studies on the mechanism of electrocatalytic C–C coupling of CH_4 are very scarce. In the future, the advanced characterization techniques used for thermocatalytic CH_4 studies such as synchrotron VUV photoionization mass spectroscopy should be exploited for mechanistic studies for photocatalytic and electrocatalytic CH_4 conversions to offer deeper understanding of the C–C coupling and other elementary steps.

6. Photocatalytic and electrocatalytic conversions of CH_3OH and HCHO

Methanol is an abundant and key C1 feedstock, which can be produced from either fossil resources (in particular coal and natural/shale gas via syngas) or renewable carbon resources (biomass via syngas or CO_2 hydrogenation).²⁹⁰ Various types of C_{2+} chemicals, including both hydrocarbons and oxygenates, can be produced from methanol. The selective oxidation of methanol to formaldehyde, carbonylation of methanol into acetic acid and the conversion of methanol to olefins (MTO) and gasoline (MTG) are well-established commercial processes. The direct conversion of methanol into a high-value C_{2+} product with high selectivity is still the most attractive and challenging target in methanol chemistry. Here, we highlight recent studies on the conversion of methanol or formaldehyde to C_{2+} compounds under mild conditions using photocatalysis and electrocatalysis (Table 7).^{291–306}

Table 7 Photocatalytic and electrocatalytic systems for the conversions of CH_3OH and HCHO to C_{2+} compounds

Catalyst	Target product	Reaction condition	Formation rate ($\text{mmol g}^{-1} \text{h}^{-1}$)	Selectivity (%)	Yield (%)	Ref.
Photocatalytic conversion of CH_3OH						
ZnS	EG	Hg arc lamp	1.0	75	0.3 (60 h)	291
MoS_2/CdS	EG	Xe lamp (420–780 nm)	11	90	16 (100 h)	292
$\text{CoP/Zn}_2\text{In}_2\text{S}_5$	EG	Xe lamp (AM 1.5)	18.9	90	4.5 (12 h)	293
GaN	$\text{C}_2\text{H}_5\text{OH}$	Xe lamp (290–380 nm)	~4.0	100	~5.4 (12 h)	294
$\text{Ni}_2\text{P}/\text{CdS}$	1,1-dimethoxymethane	Xe lamp (>400 nm)	188	83	1.7 (3 h)	295
Pt/TiO ₂	EG	UV light (320–400 nm)	~2	80	~0.4 (10 h)	296
Pt/TiO ₂	Aliphatic alcohols	Xe lamp (200–400 nm)	0.013–0.094	>90	0.94–6.6 (15 h)	297
CdS	Aliphatic alcohols	Xe lamp (>420 nm)	0.0035–0.0070	>70	0.35–0.70 (20 h)	298
Electrocatalytic conversion of CH_3OH (including dielectric barrier discharge, DBD)						
$\text{Co}_3\text{ZnC}/\text{NC}$	$\text{C}_2\text{H}_5\text{OH}$	$j: 10 \text{ mA cm}^{-2}, E: 1.54 \text{ V}^\alpha$	24.4 $\text{mg cm}^{-2} \text{ h}^{-1}$	95 (FE: 12)	3.2 (4.5 h)	299

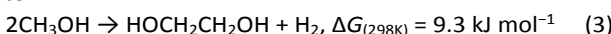
-	EG	DBD, AC 16.8 kV ^b , 300 °C	~1.7 mmol h ⁻¹	72	11.3	View Article Online DOI: 10.1039/D0EE00300K 300
-	EG	DBD, AC 16.8 kV ^b , 300 °C	~3.3 mmol h ⁻¹	75	22.5	301
-	n-C ₄ H ₁₀	DBD, AC 30 kV ^b , 140 °C	-	37.5	15	302
Photocatalytic conversion of HCHO						
BiVO ₄	EG, CH ₃ CHO, HOCH ₂ CHO	Xe lamp (320-780 nm)	11	74	8 (12 h)	303
MnO _x -Pt@MoO _x /BiVO ₄	EG, CH ₃ CHO, HOCH ₂ CHO	Xe lamp (320-780 nm)	54	74	21 (12 h)	304
Electrocatalytic conversion of HCHO						
Mercury	EG	j: 250 mA cm ⁻² , E: ~−1.0 V ^a	-	FE: 30	-	305
Graphite	EG	j: 400 mA cm ⁻² , E: −1.0 V ^a	-	FE: 97	~10.4	306

^aThe potential refers to RHE; ^bThe potential represents the full-cell potential (V).

6.1. Photocatalytic and electrocatalytic conversions of CH₃OH

6.1.1 Photocatalytic conversion of CH₃OH. CH₃OH has been widely used as a sacrificial agent for photocatalytic H₂ evolution, where CH₃OH serves as a hole scavenger. In most cases, the products of methanol oxidation were C1 derivatives, such as HCHO, HCOOH, CO₂.³⁰⁷ However, some recent studies have demonstrated that CH₃OH can be converted to high-value C₂₊ compounds such as ethylene glycol and ethanol by semiconductor photocatalysis under light irradiation.^{291-295,308} Further, the photocatalytic coupling of CH₃OH with other molecules such as HCHO and olefins can also proceed with CH₃OH as a hydroxymethylation agent, forming unique higher alcohols.²⁹⁶⁻²⁹⁸

The dehydrogenative coupling of methanol to ethylene glycol (EG) (eqn (3), denoted as MTEG) is a very attractive but highly challenging reaction. The product of this reaction, i.e., EG, is an important chemical with many important applications, in particular as a monomer for the production of poly(ethylene terephthalate) (PET). Currently, EG is primarily produced from ethylene by hydration. The development of methanol-based EG production route would provide an alternative non-petroleum route.



In an early communication, Yanagida and co-workers reported that the oxidation of methanol over ZnS ($E_g = 3.6$ eV, corresponding to $\lambda = 345$ nm) under UV-light irradiation formed HCHO and EG.²⁹¹ The rate and selectivity of EG were ~ 1 mmol g⁻¹ h⁻¹ and $\sim 75\%$, respectively.

Recently, our group demonstrated that the dehydrogenative coupling of methanol into ethylene glycol could proceed over CdS ($E_g = 2.4$ eV, corresponding to $\lambda = 518$ nm) under visible-light irradiation.²⁹² ZnS and CdS were found to be unique photocatalysts for the formation of EG and other types of semiconductors such as TiO₂, ZnO, C₃N₄ and CuS provided HCHO, HCOOH, CO and CO₂. Nanorod-shaped CdS showed better performances than CdS nanoparticles. Different types of co-catalysts were examined to enhance the performance of CdS nanorods and MoS₂ was found to be the best co-catalyst. Upon loading 5 wt% three-dimensional MoS₂ nanofoams to CdS nanorods (Fig. 39a), the formation rate of EG increased from 0.46 to 11 mmol g⁻¹ h⁻¹ and the selectivity of EG on a molar carbon basis increased from 71% to 90%. The yield

of EG on the molar carbon basis was calculated to be $\sim 2.5\%$ after 12 h of reaction under visible-light ($\lambda = 420$ -780 nm) irradiation. The increase in reaction time to obtain higher yield of EG in the conventional batch-type reactor led to significant decreases in EG selectivity due to the consecutive oxidation. The design of a process-intensified reactor with simultaneous reaction and CH₃OH/EG separation ability could keep the EG selectivity at 90% during 100 h of reaction, affording an EG yield of 16% (Fig. 39b).²⁹² The mechanistic studies revealed that EG was formed by oxidative coupling of CH₃OH by photogenerated holes, while photogenerated electrons contributed to H₂ formation. CdS was found to be quite unique in the preferential activation of the

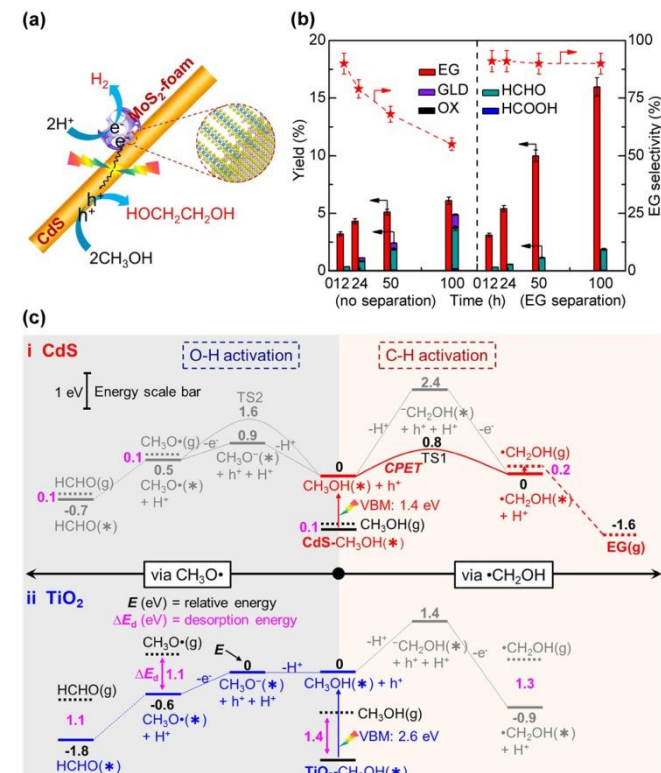


Fig. 39 (a) Schematic illustration of MoS₂ foam/CdS for photocatalytic synthesis of EG and H₂ from CH₃OH. (b) Catalytic performance of MoS₂ foam/CdS with process intensification. (c) Reaction energy profiles via •CH₂OH and CH₃O• on CdS(100) and rutile TiO₂(110).²⁹² Reproduced from ref. 292, with the permission of Springer-Nature, copyright 2018.

REVIEW

Energy & Environmental Science

C–H bond in CH_3OH by the holes without affecting the O–H group, generating $\bullet\text{CH}_2\text{OH}$ intermediate, which coupled to give EG. DFT calculations suggested that the weak absorption of CH_3OH on CdS surfaces offered a possibility of preferential activation of C–H bond instead of O–H bond (Fig. 39c). The cleavage of C–H bond in CH_3OH on CdS surfaces to produce $\bullet\text{CH}_2\text{OH}$ radical occurred through a concerted proton-electron transfer (CPET) mechanism with a low activation barrier. The weakly adsorbed $\bullet\text{CH}_2\text{OH}$ could readily desorb from CdS surfaces for subsequent C–C coupling. On the other hand, the stronger adsorption of CH_3OH on TiO_2 led to a very easy proton transfer in the first step, forming CH_3O^- species on TiO_2 surfaces, which consequently resulted in the formation of HCHO (Fig. 39c).

Very recently, instead of CdS, an environmental-friendly sheet-like $\text{Zn}_2\text{In}_2\text{S}_5$ semiconductor was further found to be efficient for selective conversion of CH_3OH to EG under visible-light irradiation.²⁹³ The loading of 0.25 wt% CoP onto $\text{Zn}_2\text{In}_2\text{S}_5$ enhanced the EG selectivity to 90%. Under the simulated sunlight irradiation (AM1.5), the formation rate of EG on the 0.25 wt% CoP/ $\text{Zn}_2\text{In}_2\text{S}_5$ catalyst reached 18.9 mmol g⁻¹ h⁻¹ and the EG yield on the molar carbon basis was 4.5% after 12 h of reaction.²⁹³ In addition to the conversion of CH_3OH to EG, the CoP/ $\text{Zn}_2\text{In}_2\text{S}_5$ catalyst could also work for the photocatalytic

of the rod and the non-polar surface (*m*-place) located at the side of the rod. The conversion of 25 μl CH_3OH over 0.35 mg GaN nanowire doped with trace amount of Mg²⁺ (*p*-GaN) under UV-vis-light irradiation offered 17 μmol $\text{C}_2\text{H}_5\text{OH}$ in 12 h, showing a formation rate of $\text{C}_2\text{H}_5\text{OH}$ of ~4.0 mmol g⁻¹ h⁻¹.²⁹⁴ Further studies indicated that the polar plane (*c*-plane) was mainly responsible for the formation of $\text{C}_2\text{H}_5\text{OH}$. Mechanistic studies suggested that methyl carbene ($:\text{CH}_2$) intermediate might be generated on the polar *c*-plane of GaN surfaces for subsequent inserting to the C–H bond of CH_3OH to form $\text{C}_2\text{H}_5\text{OH}$ (Fig. 40). Moreover, CH_3OH could be converted to *n*- $\text{C}_3\text{H}_7\text{OH}$ over GaN nanowire under UV-vis-light irradiation by lowering the reaction temperature from 15 to 0 °C, and this indicated that this reaction system may have the potential for synthesis of a wide range of lower to higher alcohols.

Besides EG and $\text{C}_2\text{H}_5\text{OH}$, 1,1-dimethoxymethane (DMM) could also be synthesized by photocatalytic conversion of CH_3OH . DMM is a product without C–C bond but is of importance as the precursor of polyoxymethylene dimethyl ether (POMM), which is an environmental-friendly embalming agent to replace HCHO. When Ni₂P/CdS was used as a photocatalyst for the conversion of CH_3OH under visible-light irradiation, the major product was found to shift from EG to DMM by adding a small amount of sulphuric acid.²⁹⁵ The selectivity and formation rate of DMM reached 83% and 188 mmol g⁻¹ h⁻¹ at a H_2SO_4 concentration of 40 mM. It was speculated that the presence of H⁺ induced the reaction between the formed HCHO and CH_3OH to produce DMM.

Photocatalytic coupling of CH_3OH with other molecules have been reported by Zhong, Sun and co-workers.^{296–298} For example, the photocatalytic coupling of CH_3OH and HCHO could proceed over a Pt/ TiO_2 catalyst under UV-light irradiation, offering EG with a selectivity of 80%.²⁹⁶ It was proposed that CH_3OH was first oxidised by photogenerated holes to form $\bullet\text{CH}_2\text{OH}$ and then the $\bullet\text{CH}_2\text{OH}$ intermediate reacted with HCHO to give $\text{HOCH}_2\text{CH}_2\text{O}\bullet$, which was finally transformed to EG by photogenerated electrons and protons. The coupling of $\bullet\text{CH}_2\text{OH}$ could also afford EG. The photocatalytic coupling of CH_3OH with terminal olefins could proceed efficiently over Pt/ TiO_2 or CdS to form higher aliphatic alcohols.^{297,298} In the reaction, CH_3OH worked as a hydroxymethylation agent and a wide range of terminal olefins were successfully functionalized to the corresponding longer aliphatic alcohols with high anti-Markovnikov selectivity. Mechanistic studies indicated that CH_3OH was oxidised by photogenerated holes to $\bullet\text{CH}_2\text{OH}$ radical, which then attacked the terminal olefins to generate a new C–C bond and another radical intermediate for subsequent reduction by photogenerated electrons to aliphatic alcohols.

6.1.2 Electrocatalytic conversion of CH_3OH .

Electrocatalytic conversion of CH_3OH has widely been studied in direct CH_3OH fuel cell (DMFC), where CH_3OH is completely oxidised to CO_2 over most electrocatalysts.³⁰⁹ Only a few papers have reported the electrocatalytic conversion of CH_3OH to C_2+ products. Recently, Zhan and co-workers demonstrated that CH_3OH could be converted to $\text{C}_2\text{H}_5\text{OH}$ over a carbon-supported metal cathode at 20 °C and atmospheric pressure (eqn (4)–(6)).²⁹⁹ A Co₃ZnC/NC (NC = nitrogen-containing carbon) catalyst was found to show the best performance for $\text{C}_2\text{H}_5\text{OH}$ formation among several carbon-supported metal

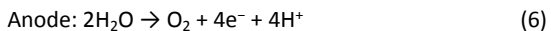
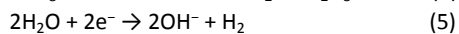


Fig. 40 Proposed mechanism for the conversion of CH_3OH to $\text{C}_2\text{H}_5\text{OH}$ on GaN surface.²⁹⁴

dehydrogenative coupling of ethanol to 2,3-butanediol. Under visible-light irradiation, the selectivity and formation rate of 2,3-butanediol were 53% and 3.2 mmol g⁻¹ h⁻¹, respectively.²⁹³ ESR measurements confirmed that the reaction proceeded via the $\bullet\text{CH}(\text{OH})\text{CH}_3$ intermediate. The photocatalytic dehydrogenative coupling of ethanol to 2,3-butanediol was also reported previously using TiO_2 catalyst by Zhu and co-workers.³⁰⁸ The pre-treatment of TiO_2 at high temperatures to remove the surface hydroxyl groups was found to be the key to obtaining high selectivity of 2,3-butanediol from ethanol, and this might indicate that to avoid the interaction of –OH of ethanol with surface was vital.

Photocatalytic conversion of CH_3OH could also afford $\text{C}_2\text{H}_5\text{OH}$ as the major product. Li and co-workers showed that GaN nanowires could catalyse the one-step conversion of CH_3OH to $\text{C}_2\text{H}_5\text{OH}$ under UV-vis-light irradiation at ambient temperature.²⁹⁴ The cylinder-shaped GaN-nanowire catalyst with average diameters of 100 nm and lengths of 800 nm was fabricated and the catalyst exposed two types of surfaces, i.e., the polar surface (*c*-plane) located at the end

catalysts. The conversion rate of CH_3OH reached $25.7 \text{ mg cm}^{-2} \text{ h}^{-1}$ with a $\text{C}_2\text{H}_5\text{OH}$ selectivity (molar carbon basis) of 95% and a $\text{C}_2\text{H}_5\text{OH}$ FE of 12%.²⁹⁹ The lower FE of $\text{C}_2\text{H}_5\text{OH}$ was due to the competitive H_2 evolution reaction on the cathode. It is clear that the FE of $\text{C}_2\text{H}_5\text{OH}$ needs to be improved in the future.



Dielectric barrier discharge (DBD) is the electrical discharge between two electrodes separated by an insulating dielectric barrier, which can readily generate free radicals in the gas phase for radical

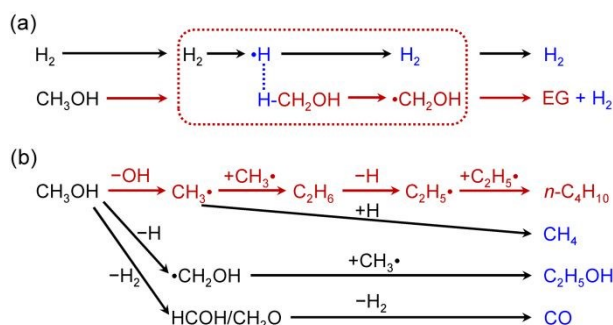


Fig. 41 Proposed mechanisms for the conversion of CH_3OH in a dielectric barrier discharge reactor. (a) EG formation,³⁰¹ (b) $n\text{-C}_4\text{H}_{10}$ formation.³⁰²

reactions. The DBD has been used for methanol conversion to C_{2+} compounds such as EG and $n\text{-C}_4\text{H}_{10}$.^{300-302,310} Guo and co-workers have systematically studied the direct synthesis of EG by co-feeding of CH_3OH and H_2 in a double dielectric barrier discharge reactor.^{300,301} Under the optimised reaction conditions, under a $\text{H}_2/\text{CH}_3\text{OH}$ molar ratio of ~7.2 and 300 °C, the CH_3OH conversion and EG selectivity reached 30% and 75%, respectively. The co-feeding of H_2 could improve the CH_3OH conversion and EG selectivity, and played a catalytic role by releasing $\cdot\text{H}$ radicals for the abstraction of hydrogen from CH_3OH to form $\cdot\text{CH}_2\text{OH}$ intermediates for subsequent C–C coupling to EG (Fig. 41a).³⁰¹ Tu and co-workers demonstrated that CH_3OH could be converted to $n\text{-C}_4\text{H}_{10}$ and H_2 in a DBD reactor.³⁰² The optimised selectivities of $n\text{-C}_4\text{H}_{10}$, H_2 and CO were 37.5%, 28.9% and 14%, respectively, with a CH_3OH conversion of 40% at a CH_3OH inlet concentration of 18 mol% and a reaction temperature of 140 °C using N_2 as a carrier gas. It was proposed that $\text{CH}_3\bullet$ radicals were generated by electron impact dissociation and then the $\text{CH}_3\bullet$ radicals dimerized to C_2H_6 , which could further be converted to $\text{C}_2\text{H}_5\bullet$ radicals through hydrogen abstraction and then undergo C–C coupling to $n\text{-C}_4\text{H}_{10}$ (Fig. 41b). The presence of several competitive pathways for the formation of CO, CH_4 , and $\text{C}_2\text{H}_5\text{OH}$ reduced the selectivity of $n\text{-C}_4\text{H}_{10}$.

6.2. Photocatalytic and electrocatalytic conversions of HCHO

Photocatalysis and electrocatalysis also offer opportunities for the direct conversion of formaldehyde to C_{2+} compounds, in particular EG.³⁰³⁻³⁰⁶ Our group first developed a photocatalytic route for coupling of HCHO to C_2 oxygenates.³⁰³ BiVO_4 and Bi_2WO_6 were found to catalyse the conversion of HCHO, providing EG, glycolaldehyde, acetaldehyde as the major products with a total C_2 selectivity of 74%.

BiVO_4 nanocrystals with truncated tetragonal bipyramidal morphology and controllable {010} and {110} facets were fabricated.³⁰⁴ The BiVO_4 nanocrystal catalyst with an equal fraction of {010}/{110} showed a C_2 yield of 12% during the conversion of HCHO aqueous solution under UV-vis-light irradiation for 12 h.³⁰⁴ This catalyst had the highest ability to separate the photogenerated electrons and holes probably because photogenerated electrons and holes migrated separately to {010} and {110} facets, respectively. The effects of co-catalysts were further investigated. The photo-deposition of co-catalysts showed that $\text{Pt}@{\text{MoO}}_x$ with Pt core and MoO_x shell was selectively deposited on the {010} facets, whereas MnO_x was deposited selectively on the {110} facets (Fig. 42a).³⁰⁴ This provided further evidence for the migration of photogenerated electrons and holes towards different facets for reduction and oxidation. The single Pt or MoO_x did not significantly promote the catalytic activity of BiVO_4 , whereas the $\text{Pt}@{\text{MoO}}_x$ co-catalyst accelerated the formation of C_2 oxygenates, in particular EG (Fig. 42b). The presence of MnO_x as an oxidation co-catalyst further enhanced EG formation. The yields of C_2 compounds and EG over the 3% MnO_x –0.5% Pt @3% $\text{MoO}_x/\text{BiVO}_4$ catalyst reached 21% and 11%, respectively, under UV-vis light irradiation for 12 h. Mechanistic studies revealed that Pt worked for the extraction of photogenerated electrons and accelerate the electron-hole separation, while MoO_x provided active sites for the activation of HCHO. In brief, Mo^{6+} was proposed to be reduced to Mo^{5+} by accepting a photogenerated electron passed from Pt core, and the Mo^{5+} site could adsorb HCHO

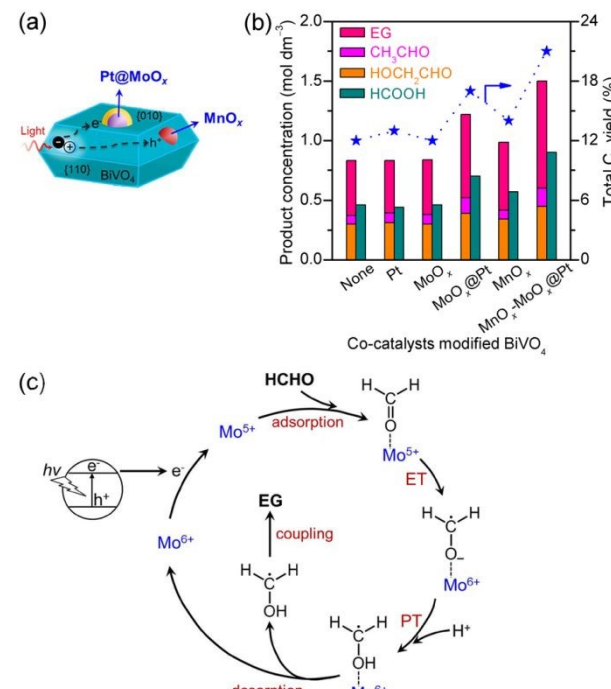


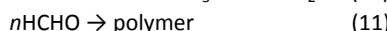
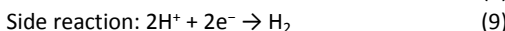
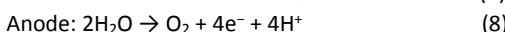
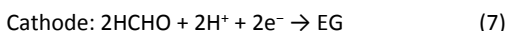
Fig. 42 (a) Model of $\text{MnO}_x\text{-Pt}@{\text{MoO}}_x/\text{BiVO}_4$ catalyst. (b) Effect of co-catalysts on the performance of BiVO_4 for photocatalytic conversion of HCHO. (c) Proposed mechanism for the conversion of HCHO to EG over $\text{MnO}_x\text{-Pt}@{\text{MoO}}_x/\text{BiVO}_4$.³⁰⁴

and transfer the electron (ET) to the adsorbed HCHO (Fig. 42c). Then, the proton transfer (PT) led to the formation of $\cdot\text{CH}_2\text{OH}$, which coupled to give EG after desorption.

REVIEW

Energy & Environmental Science

The electrocatalytic reductive coupling of HCHO is also an important route for the synthesis of EG under mild conditions (eqn (7) and (8)).^{305,306} The materials with high H₂ evolution overpotential, such as Cd, Hg, Pb, Ti, and graphite, could be used as cathode to suppress the competitive H₂ evolution reaction (eqn (9)). Mazur and co-workers found that graphite showed the best performance for the formation of EG.³⁰⁶ A large fraction of HCHO was in the hemiacetal form in the presence of methanol inhibitor, and a high pH could cause the disproportionation of HCHO to CH₃OH and HCOO⁻ (eqn (10)), whereas a lower pH would lead to the polymerization of HCHO by acid catalysis (eqn (11)). Thus, the control of reaction conditions to obtain a high concentration of free HCHO for C–C coupling and to suppress side reactions is essential to EG formation. The optimum reaction conditions required high concentration of aqueous HCHO solution, near-neutral pH of 5 to 8, the addition of quaternary ammonium salt and reaction temperature of about 80 °C. Under the optimized conditions, with an applied current density of 300 mA cm⁻² and HCHO concentration of 52%, the FE of EG was higher than 80% and EG concentration reached 23%.³⁰⁶ However, with an increase in HCHO conversion, the FE of EG decreased significantly. The separation of EG from the electrolyte solution is also a challenging issue that needs to be solved for commercialisation.



6.3. Mechanism of C–C coupling for photocatalytic and electrocatalytic conversions of CH₃OH and HCHO to C₂₊ compounds

The thermocatalytic activation of CH₃OH usually leads to the cleavage of its C–O or O–H bond, and the resulting CH_x species may undergo C–C bond formation. The use of zeolite catalysts like in the MTO process can partially control the product selectivity due to their shape-selective effect.²² Interestingly, the preferential activation of C–H bond of CH₃OH has been successfully achieved by photocatalysis using CdS-based catalysts, and EG could be obtained with a selectivity of 90% via the subsequent coupling of •CH₂OH intermediate.^{292,293} To the best of our knowledge, this cannot be accomplished through thermocatalysis. The formation of •CH₂OH in photocatalytic conversion of CH₃OH has been confirmed by *in situ* ESR.^{292,293} In a DBD reactor, CH₃OH could also be converted to •CH₂OH with electrical energy, which undergoes coupling to EG.^{300,301} Further, EG can be produced by photocatalytic or electrocatalytic reduction of HCHO. Similarly, •CH₂OH is the key intermediate during photocatalytic/electrocatalytic conversion of HCHO to EG.^{303–306} Besides EG, C₂H₅OH was reported to be obtained through photocatalytic or electrocatalytic conversion of CH₃OH.^{294,299} It is proposed that C₂H₅OH is formed by insertion of methyl carbene (:CH₂) into the C–H bond of CH₃OH on the polar plane of GaN in photocatalysis.²⁹⁴ On the other hand, CH₃[•] and •CH₂OH intermediates were confirmed by *in situ* ESR on Co₃ZnC/NC in electrocatalysis, and thus C₂H₅OH might be the coupling product between these two radicals.²⁹⁹ In the DBD reactor, CH₃OH may also be transformed into CH₃[•] intermediate, which then undergoes C–C coupling to C₂H₆. C₂H₆ could be further converted to n-C₄H₁₀ via

C₂H₅[•].³⁰² Thus, the nature of the intermediate generated from CH₃OH or HCHO in photocatalysis/electrocatalysis has a significant effect on the final C–C coupling product.

7. Conclusion and outlook

The selective transformation of C1 molecules to value-added C₂₊ compounds through controllable C–C coupling is a highly attractive but challenging research goal in chemistry. The control of C–C bond formation in the conversion of C1 molecules by thermocatalysis under harsh reaction conditions is generally difficult. Photocatalysis and electrocatalysis have offered promising ways for activation and selective transformation of C1 molecules to C₂₊ compounds under mild conditions by harnessing photo or electrical energy. The present article has highlighted key advances in photocatalytic and electrocatalytic conversions of typical C1 molecules, including CO₂, CO, CH₄, CH₃OH, and HCHO, to C₂₊ compounds, in particular C₂H₄, C₂H₆, C₂H₅OH, ethylene glycol and *n*-propanol.

Photocatalytic reduction of CO₂ to C₂₊ compounds requires efficient transfer of multi-electrons/multi-protons and suitable active sites to catalyse not only CO₂ activation but also C–C coupling. Many semiconductors, e.g., TiO₂,⁶² g-C₃N₄,⁶³ BiVO₄,⁶⁴ Bi₂WO₆,⁶⁵ and InTaO₄,⁶⁶ have been reported to be capable of working for the reduction of CO₂ to C₂₊ compounds, but the efficiencies were low. Several strategies have been reported to increase the activity and the selectivity of C₂₊ compounds. To increase the light harvesting by semiconductor doping, combination with sensitizer and loading of SPR metals could enhance the activity for CO₂ photocatalytic reduction in particular under visible-light irradiation. The enhancement in the separation of photogenerated electrons and holes by the hybridisation of different semiconductors or a semiconductor with a carbon nanomaterial and loading of co-catalysts may contribute not only to increasing the activity but also to improving the selectivity to C₂₊ products by promoting the multi-electron transfer. Several studies demonstrated that the hybridisation of TiO₂ with CNT or graphene could enhance the formation of C₂H₅OH or C₂H₆.^{73–76} The nanostructure of photocatalyst may also affect the C–C coupling. For example, the construction of mesoporous g-C₃N₄ was found to be beneficial to the formation of C₂H₅OH. The surface structure is the key to the surface reaction, and thus the modification of catalyst surfaces may modify the selectivity of C₂₊ products. For example, the coating of a thin Nafion layer on catalyst surface may increase the local proton concentration, thus favouring the multi-step proton-coupled electron transfer (PCET) reactions to facilitate the formation of C₂₊ products.⁷⁹ The co-catalyst can not only enhance the electron-hole separation but also provide active sites for CO₂ activation and C–C coupling. Several co-catalysts such as Pd,^{78,80} Rh,⁸⁰ NiO,^{66,81} Cu,^{67,83,94} and Cu–Pt bimetallic^{83,84,96} have been reported to hold potentials to promote the formation of C₂₊ compounds. Among these co-catalysts, Cu has received particular interest in the formation of C₂₊ hydrocarbons and the enhancing effect of Cu or Cu-based co-catalysts has been confirmed in many studies.^{67,69,82,83,85,94} The loading of co-catalysts on semiconductors has been demonstrated to be one of the most effective strategies for improving the photocatalytic activity and tuning the C–C coupling selectivity in CO₂ reduction. The findings suggest that the co-catalysts are necessary for developing highly efficient photocatalysts for

photocatalytic reduction of CO₂ to C₂₊ compounds. In addition, the reaction conditions and reaction medium could also exert influences on the selectivity of C₂₊ compounds. For example, the increase in CO₂ pressure and the use of a basic medium were reported to be beneficial to the formation of C₂₊ products.⁶² The addition of ionic liquid (EMIM-BF₄) into aqueous solution with a proper concentration could promote the selectivity of C₂ and C₃ hydrocarbons during photocatalytic reduction of CO₂ on plasmonic Au nanoparticles under green-light irradiation because of the enhanced CO₂ activation and accelerated electron transfer from Au nanoparticles to CO₂.⁸⁷ Despite the progress achieved, the formation rates of C₂₊ compounds are still quite low, being < 100 μmol g⁻¹ h⁻¹ in most cases (Table 1). It is noteworthy that the results with such low rates should be treated carefully, because the carbon sources contained in the reaction system including CO₂ may all have possibilities to be reduced to C₂₊ products. Therefore, to carry out isotopic ¹³C-labelling experiments to confirm that the products are derived from CO₂ as well as the quantification of O₂ formation is crucial to providing solid results. This is particularly necessary when carbon-containing photocatalysts are studied.

Three pathways, i.e., oxalic acid pathway, glyoxal pathway and methyl radical pathway, have been proposed for C-C coupling in photocatalytic reduction of CO₂ (Fig. 10b).^{45,59,104} The deep understanding of how the surface structure and other influencing factors determine the CO₂ activation and the C-C coupling is still lacking. The mechanism for the formation of C₂₊ compounds needs further studies.

Photo-driven Fischer-Tropsch synthesis is the major research in photocatalytic conversion of CO to C₂₊ compounds. It is demonstrated that the conversion of syngas to C₂₊ hydrocarbons could proceed over several supported metal catalysts under light irradiation without external heating.¹¹⁰⁻¹¹⁵ The typical Fischer-Tropsch metal (i.e., Co, Fe and Ru)-based and Ni-based catalysts all showed activities in the light-driven syngas conversions. The photo-thermal effect by metal catalysts and the photogenerated charge carriers on catalyst surfaces may both contribute to the light-driven CO hydrogenation to C₂₊ hydrocarbons. The photo-thermal effect could provide sufficient temperature at the catalyst bed for CO hydrogenation. The photogenerated charges on catalyst surfaces may create unique oxidation state and electronic structure of catalyst, thus regulating the C-C coupling and hydrogenation ability to obtain unique product selectivity. For example, lower olefins were formed with higher selectivity in the Co- and Fe (or Fe₅C₂)-catalysed photo-driven syngas conversions.¹¹⁰⁻¹¹² Ni-based catalysts could also work for the formation of C₂₊ hydrocarbons under light irradiation, whereas CH₄ was the only hydrocarbon product over Ni catalysts under thermocatalytic conditions.¹¹⁵ Despite uniqueness, the distribution of hydrocarbon products is still quite broad in the photo-driven CO hydrogenation, indicating that the C-C coupling is still uncontrollable.

Electrocatalytic reduction has recently been proven to be very promising for the synthesis of C₂₊ compounds from CO₂ or CO. Although Cu is still the only selective catalyst for electrocatalytic reduction of CO₂ to C₂₊ compounds owing to its moderate CO binding energy, significant advances have been achieved in developing active and selective Cu-based electrocatalysts for the formation of various C₂₊ compounds, including C₂H₄, C₂H₅OH, CH₃COOH and n-C₃H₇OH.

Model studies using Cu single crystals reveal that the electrocatalytic reduction of CO₂ is structure sensitive; the Cu(111) surfaces favorably offer the formation of CH₄, whereas Cu(100) and Cu(110) surfaces can offer C₂H₄ and C₂₊ oxygenates, respectively.¹⁷⁶⁻¹⁷⁸ As compared to pure metallic Cu, the oxide-derived Cu catalyst showed enhanced C₂₊ selectivity. Although the nature of active sites leading to high C₂₊ FE over oxide-derived Cu catalysts is still under debate, the current consensus is that the presence of surface Cu^{δ+} sites plays a pivotal role in the C-C coupling and the formation of C₂₊ products. Many studies have been devoted to improving the C₂₊ formation activity on Cu-based catalysts and high C₂₊ FEs have been reported. For example, the doping of a heteroatom such as boron, nitrogen or halogen on surfaces of Cu nanoparticles could offer high FEs (~80%) towards C₂₊ compounds with C₂H₄ as the major product.¹³⁹⁻¹⁴² A nano-defective Cu nanosheets catalysts derived from CuO nanosheets showed a FE of C₂H₄ as high as 83.2%.¹³⁸ Electrolyte engineering could also improve C₂₊ FEs, and larger sizes of anions or cations (e.g., I⁻ or Cs⁺) added into the electrolyte showed significant promoting effects.¹⁹⁴⁻¹⁹⁶ Recent studies using the flow cell with GDE instead of H-cell to circumvent the mass-transport limitation have achieved high C₂₊ FEs at high current densities. Typically, the alkaline GDE design has successfully enabled to achieve superior performances at commercially-relevant levels ($\geq 200 \text{ mA cm}^{-2}$).

Many studies have attempted to improve the FE toward C₂₊ oxygenate formation. The fabrication of bimetallic catalysts containing Cu and another guest metal such as Zn, Au or Ag has shown great promising for the formation of C₂₊ oxygenates, in particular C₂H₅OH, in electrocatalytic CO₂RR. The FE of C₂H₅OH could be enhanced to 41% on an Ag_{0.14}/Cu_{0.86} alloy catalyst at a current density of 400 mA cm⁻² in the alkaline flow cell.¹⁵² The design of carbon materials also holds potentials to modulate the selectivity of C₂H₅OH in Cu/carbon-catalysed CO₂RR. For example, Cu nanoparticles surrounded by N-doped carbon layers displayed a C₂H₅OH FE of 52% with a total C₂₊ FE of 93% at a current density of 300 mA cm⁻² in an alkaline flow cell.¹⁵⁶

As compared to electrocatalytic CO₂RR, Cu-catalysed electrocatalytic CORR has typically demonstrated lower overpotentials for C-C coupling and higher selectivity towards C₂₊ oxygenate formation. For example, a nanoflower Cu catalyst with a high roughness factor offered a nearly 100% selectivity to C₂ oxygenates at a potential of only -0.23 V vs. RHE despite the low current density.¹⁶⁹ Not only C₂H₅OH but also CH₃CHO, CH₃COO⁻ and n-C₃H₇OH can be produced with high selectivity during electrocatalytic CORR. CH₃COO⁻ formation was typically enhanced after switching CO₂ reactant to CO, which was attributed to higher local pH at the electrode-electrolyte interface in CORR. A 48% FE of CH₃COO⁻ was achieved at a current density of 200 mA cm⁻² during electrocatalytic CORR over a Cu nanosheet catalyst.¹⁷² It is expected that the key step in n-C₃H₇OH formation is the coupling between C1 and C₂ intermediates, however, the inadequate stabilization of C₂ intermediates on Cu surfaces usually results in desorption rather than further coupling with C1. Several strategies have been developed to stabilize C₂ species and promote the C₁-C₂ coupling to n-C₃H₇OH, including the confinement effect, creating interfaces of Cu(100) and Cu(111) facets and loading Cu adparticles on Cu surfaces. The maximum FE of n-C₃H₇OH achieved to date is 20-25%.¹⁷³⁻¹⁷⁵

REVIEW

Energy & Environmental Science

The moderate CO binding strength is believed to be one major reason for the excellent performance of Cu catalysts in electrocatalytic CO₂RR and CORR to C₂₊ products. The electrocatalytic CO₂RR to C₂₊ products on Cu usually requires potentials more negative than or close to -1.0 V to achieve industrial-relevant current densities. The search for electrocatalytic materials other than Cu may enable the CO₂RR to C₂₊ products at lower overpotentials. The fabrication of Cu-free bimetallic catalysts (e.g., Pd-Au, Ni-Ga and Ni-Al), which combine one metal that binds CO strongly with the other that binds CO weakly, could offer C₂₊ products during CO₂RR. However, the C₂₊ FEs of these bimetallic catalysts are still quite low (< 5%). Nitrogen-doped carbon-based materials have been exploited for metal-free electrocatalytic CO₂RR to C₂₊ products. A surprisingly high FE of C₂H₅OH (> 90%) has been claimed on a boron- and nitrogen-co-doped nanodiamond catalyst despite of the low current density (~1 mA cm⁻²).¹⁶⁰ In addition, some studies have demonstrated that the fabrication of bifunctional catalyst composed of a catalyst component that can accelerate the CO₂RR to CO and the N-doped carbon can enhance the formation of C₂ oxygenates, in particular C₂H₅OH.²²⁹⁻²³¹

CO is generally believed to be the key intermediate in the electrocatalytic CO₂RR to C₂₊ compounds. Several mechanisms have been proposed for C-C coupling of CO or CO-derived intermediates on Cu-based catalysts. The direct coupling of *CO to form *OCCO intermediate followed by hydrogenation to C₂H₄ and C₂H₅OH is believed to be the major C-C coupling route in most studies reported to date. Some studies have demonstrated the importance of *CHO species in the C-C coupling step, and the (*CO + *CHO) coupling or (*CHO + *CHO) coupling may participate in the formation of C₂ compounds. Two major mechanisms have been proposed for the formation of C₂H₄ and C₂ oxygenates. One assumes that *CH₂CHO serves as the selectivity-determining intermediate, while the other considers that *CHCOH is the key intermediate. In both cases, it is accepted that the hydrogenolysis of the selectivity-determining intermediate leads to C₂H₄ formation, while the hydrogenation results in C₂₊ oxygenate.

As compared to photocatalytic CO₂RR or CORR, electrocatalytic CO₂RR and CORR have made significant step-forward in controlling the product selectivity. Excellent selectivity of C₂H₄ or C₂ oxygenates such as C₂H₅OH or CH₃COO⁻ has been achieved at industrial-relevant current densities. Nevertheless, challenges still remain for electrocatalytic CO₂ and CO conversions to C₂₊ products. First, the most efficient alkaline GDE suffers from stability issue. More effort should be put to improve the resistance of GDE flooding. Electrocatalytic CORR can avoid the salt accumulation in alkaline condition, and thus improved stability may be expected for electrocatalytic CORR than for direct CO₂RR. Thus, to implement a tandem strategy to synthesize C₂₊ products from CO₂ via CO would be useful. Second, most electrocatalytic CO₂RR and CORR studies have only touched the cathodic half-reaction, and the oxygen evolution reaction in the anode has seldom been considered. Combining an efficient oxygen-evolution catalyst with CO₂RR or CORR to improve the full-cell energy conversion efficiency would be important for future industrial application. Third, it still remains challenging to achieve a sufficient CO₂/CO single-pass conversion or single-pass target product yield that is comparable to the commercial Fischer-Tropsch synthesis process.

As compared to the traditional thermocatalytic OCM and CH₄ dehydrogenative coupling processes, the photocatalytic conversion of CH₄ to C₂₊ compounds can be performed under very mild conditions, although the efficiency is quite limited. Metal cations or oxides highly dispersed on SiO₂, Al₂O₃ and zeolites (e.g., Zn⁺-ZSM-5²⁵⁵ and Ga-EST-10²⁵⁶) and some semiconductors (Au/ZnO²⁵⁷, GaN²⁵⁸ and Ag⁺-HPW/TiO₂²⁵⁹) have been reported for the non-oxidative dehydrogenation of CH₄ to C₂H₆ or C₆H₆ under UV-light irradiation. The active site, such as Zn²⁺ and Ga³⁺ ions, could promote the adsorption of CH₄ and the polarization of C-H bond to form CH₃ surface species or radicals for C-C coupling to C₂H₆. The formation of C₆H₆ is more difficult, because it needs multi-step dehydrogenation and cyclization processes. The non-oxidative reaction condition may facilitate the C-C bond formation to C₂₊ hydrocarbons. In the presence of H₂O, in addition to hydrocarbons, CH₃OH and C₂H₅OH are also formed. Hydroxyl radicals (•OH) formed through the oxidation of H₂O by photogenerated holes have been detected and proposed to be the reactive oxygen species for abstracting a hydrogen atom from CH₄ to generate CH₃•. The •OH radical can be easily generated through the decomposition of H₂O₂. Thus, the design of photocatalysts with high H₂O₂ generation activity may be promising for CH₄ conversion.

Electrocatalytic conversion of CH₄ to C₂ hydrocarbons could be performed in solid oxide-electrolyte reactors at high temperatures similar to that used for OCM reactions. However, the gas-phase non-selective oxidation of CH₄ may be inhibited, because CH₄ and O₂ are fed separately in anode and cathode compartments. Many modified OCM catalysts have been employed as the electrocatalysts for CH₄ conversion. By using a reaction system with product separation and CH₄ recycling abilities, the yields of C₂ hydrocarbons and C₂H₄ could reach 88% and 85%, respectively, over a porous Ag catalyst.²⁷³ Over a Fe-doped layered perovskite anode (Sr₂Fe_{1.575}Mo_{0.5}O_{1.6}) for CH₄ oxidation, the single-pass conversion of CH₄ could reach 41% and the yield of C₂ hydrocarbons (C₂H₄ and C₂H₆) reached 33%, when O₂ was fed to the cathode.²⁷⁹ O₂ on the cathode could be replaced by H₂O or CO₂ and H₂ or CO would be formed simultaneously with CH₄ oxidative coupling products. Because of the higher thermodynamic and kinetic barriers for H₂O and CO₂ electrolysis to generate oxygen ions on the cathode, the performance of electrocatalytic conversion of CH₄ to C₂ hydrocarbons using H₂O or CO₂ is still not high. However, the full use of the anode and cathode half reaction to produce useful chemicals is important, and much effort should be put in the future to develop high efficiency electrocatalysts for both cathode and anode reactions. The studies on electrocatalytic conversion of CH₄ to C₂₊ compounds at moderate temperatures have also emerged in recent years, and this direction is definitely worthy of further study.

The photocatalytic and electrocatalytic conversions of CH₃OH and HCHO to C₂₊ compounds are important targets that have not been widely studied. Some novel reactions, such as the visible-light-driven dehydrogenative coupling of CH₃OH to EG,^{292,293} light-driven one-step conversion of CH₃OH to C₂H₅OH,²⁹⁴ photocatalytic coupling of HCHO to EG,^{303,304} and electrocatalytic conversion of CH₃OH to C₂H₅OH,²⁹⁹ have been developed in recent years. A high selectivity (90%) and yield (16%) of EG have been achieved through photocatalytic coupling of CH₃OH to EG by using MoS₂ foam-modified CdS nanorod catalyst under visible-light irradiation.²⁹² It has been demonstrated that C-H bond of CH₃OH is activated by the

photogenerated hole to $\bullet\text{CH}_2\text{OH}$, which couples to give EG.²⁹² Thus, these studies also offer an opportunity for the preferential activation of C–H bond of functionalised molecules. It is of interest that $\bullet\text{CH}_2\text{OH}$ is a common intermediate for the photocatalytic and electrocatalytic coupling of CH_3OH or HCHO to EG. Thus, CH_3OH or HCHO could be utilised as a platform for hydroxymethylation reaction to construct new C–C coupling to produce diols or higher aliphatic alcohols in synthetic chemistry.

Some catalysts have shown promising performances for photocatalytic and electrocatalytic conversions of C1 molecules into C_{2+} compounds. For photocatalytic reduction of CO_2 , a Pt-0.5G-TiO_{2-x} catalyst achieved formation rates of CH_4 and C_2H_6 of 37 and 11 $\mu\text{mol g}^{-1}\text{ h}^{-1}$, respectively, under one sun AM 1.5G illumination with solid evidence for the formation of CH_4 and C_2H_6 from CO_2 by ¹³ CO_2 isotopic control experiments.⁷⁶ The apparent quantum yield of ($\text{CH}_4 + \text{C}_2\text{H}_6$) reached 7.9% and the catalyst was stable during 42 h of reaction. A Cu-modified polymeric carbon nitride (PCN) could work for photocatalytic conversion of CH_4 with H_2O to $\text{C}_2\text{H}_5\text{OH}$ under UV-vis light irradiation, and the formation rate of $\text{C}_2\text{H}_5\text{OH}$ reached 106 $\mu\text{mol g}^{-1}\text{ h}^{-1}$.²⁶⁵ Despite the progress, the state-of-the-art performances for photocatalytic conversions of CO_2 and CH_4 are far from commercial consideration. On the other hand, the performances for photocatalytic conversions of CO, CH_3OH and HCHO are usually significantly better than those for photocatalytic conversions of CO_2 and CH_4 . For example, without external heating, the Fe₅C₂ for photo-thermal hydrogenation of CO at atmospheric pressure under UV-vis light irradiation provided a CO conversion of 49.5% (conversion rate, 17 $\text{mmol g}^{-1}\text{ h}^{-1}$) with $\text{C}_2\text{-C}_4$ olefin selectivity of 55.5% (CO_2 selectivity, 18.9%).¹¹² For photocatalytic conversion of methanol, the EG formation rate could reach 11 $\text{mmol g}^{-1}\text{ h}^{-1}$ over a MoS₂/CdS catalyst under visible-light irradiation, with EG selectivity, yield and quantum yield of 90%, 16% and 5%, respectively.²⁹² HCHO is more reactive and the formation rate of C_2 compounds (EG, CH_3CHO , HOCH₂CHO) could reach 54 $\text{mmol g}^{-1}\text{ h}^{-1}$ from HCHO over a MnO_x-Pt@MoO_x/BiVO₄ catalyst under UV-vis light irradiation.³⁰⁴ Further, as compared to photocatalysis, electrocatalysis has achieved much better performances for the transformations of inert CO_2 and CH_4 . For electrocatalytic CO₂RR, the FE and partial current density of C_2H_4 over Cu-based catalysts could reach 83% and 1.3 A cm^{-2} , respectively.^{138,145} A fluorine-modified Cu catalyst offered C_{2-4} products (mainly C_2H_4 and $\text{C}_2\text{H}_5\text{OH}$) with selectivity of 85.8% and single-pass yield of 16.5%, and the formation rate of C_2H_4 reached 3.2 $\text{mmol h}^{-1}\text{ cm}^{-2}$ (12.8 mol $\text{g}^{-1}\text{ h}^{-1}$).¹⁴² This performance outperforms those achieved in high-temperature and high-pressure thermocatalysis.⁸ A Fe-Sr₂Fe_{1.5}Mo_{0.5}O_{6-δ} catalyst showed a current density of 1.0 A cm^{-2} in the electrocatalytic oxidation of CH_4 at an applied voltage of 1.6 V and a temperature of 850 °C.²⁷⁹ The conversion of CH_4 , the selectivity and yield of C_2 products (C_2H_4 and C_2H_6) reached 41%, 81.2% and 33%, respectively.²⁷⁹ It is noteworthy that recent studies on electrocatalytic conversion of CH_3OH or HCHO to C_{2+} compounds are very limited.

With the flourishing development of photocatalytic and electrocatalytic systems for the transformations of C1 molecules into C_{2+} products, the catalyst stability has become an important issue for future applications. Better stability would reduce the associated maintenance and consumable costs, and is one of the keys for commercial applications of photocatalytic and electrocatalytic

conversions of C1 molecules into C_{2+} compounds. Many photocatalysts and electrocatalysts reported for the conversion of C1 molecules showed good stability of tens or hundreds of hours. For a potential photocatalytic process such as H_2 evolution by water splitting, a stability of 1000 h with a solar to chemical efficiency of 10% is required for commercial applications.³¹¹ Considering the comparability, the catalyst stability for photocatalytic conversions of C1 molecules to C_{2+} compounds should exceed 1000 h at a sufficiently high quantum efficiency (at least >10%). As described above, the FE (>80%) and current density (>1 A cm^{-2}) reported for the electrocatalytic CO₂RR to C_{2+} products (mainly C_2H_4 , $\text{C}_2\text{H}_5\text{OH}$) could meet the industrial requirement, but the long-term catalyst stability is still a challenge. The best stability achieved to date for electrocatalytic CO₂RR to C_{2+} compounds is 190 h at a current density of ~120 mA cm^{-2} .¹⁴⁶ It was once considered that a catalyst stability of about 5000 h is required as the first cornerstone for an electrocatalytic process.³¹² There is a large room for the future studies to improve the catalyst stability in photocatalytic and electrocatalytic transformations of C1 molecules to C_2 compounds.

The understanding of reaction mechanism would not only deepen our knowledge of C1 chemistry but also can help to develop more efficient photocatalysts and electrocatalysts for valorisation of C1 molecules. Generally, the photocatalytic and electrocatalytic conversions of C1 molecules to C_{2+} compounds include two major steps: the activation of C1 molecules to C1 intermediates and C–C coupling of C1 intermediates to C_{2+} compounds. The C1 intermediates may also be easily converted into other C1 molecules,

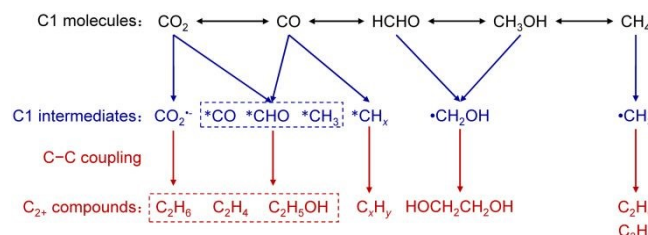


Fig. 43 Proposed C1 intermediates in photocatalytic and electrocatalytic conversions of C1 molecules to C_{2+} compounds. “*” in the figure represents surface or radical species.

and thus controlling C–C coupling of C1 intermediates is the key to obtaining high selectivity of C_{2+} products. Mechanistic studies have pointed out that the typical C1 molecules, including CO_2 , CO, CH_4 , CH_3OH and HCHO, are transformed into specific C1 surface species or radicals, which then undergo C–C coupling to C_{2+} compounds through multi-electron/multi-proton transfer processes (Fig. 43). For example, $\text{CO}_2\bullet^-$, $\bullet\text{CHO}$ and $\text{CH}_3\bullet$ have been proposed as the C1 intermediates for C–C coupling to form oxalic acid, glyoxal and C_2H_6 , respectively, in photocatalytic CO_2 reduction.^{67,107-109} In electrocatalytic CO₂RR and CORR, $*\text{CO}$ species has been proposed to be the major intermediate for C–C coupling in most studies,²³²⁻²³⁴ but recent studies have demonstrated that the coupling between $*\text{CHO}$ species is a more facile pathway.^{142,236,237,239} $\bullet\text{CH}_2\text{OH}$ radical is the intermediate for C–C coupling in photocatalytic and electrocatalytic conversions of CH_3OH and HCHO to EG.^{292,301,304,306} Meanwhile, $\text{CH}_3\bullet$ radical is the key intermediate for the C–C coupling in either photocatalytic or electrocatalytic conversion of CH_4 to C_2H_6 .^{251,256-258,264,279} It is noteworthy that the insights into the detailed mechanisms for C1-molecule activation, reaction

REVIEW

Energy & Environmental Science

intermediate formation, C–C coupling and product formation are still very limited. The nature of active sites and the synergy between catalytically active sites and electrons/holes/protons are not well documented. The state-of-the-art knowledge cannot enable rational design of efficient photocatalysts or electrocatalysts with controlled product selectivity.

Advanced characterization techniques have also promoted the progress in photocatalytic and electrocatalytic transformations of C₁ molecules, in particular for the elucidation of active sites and reaction intermediates. Take electrocatalytic CO₂RR and CORR as examples. To understand the nature of active sites leading to high C₂₊ FE over oxide-derived Cu catalysts, multiple *in situ* characterization techniques have been employed to investigate the oxidation state of Cu under reaction conditions, including secondary-ion mass spectrometry¹⁸⁵, surface-enhanced Raman spectroscopy¹⁸⁹ and time-resolved X-ray absorption spectroscopy³¹³. *In situ* spectroscopic studies have also been used to detect the reaction intermediate. Through *in situ* FT-IR spectroscopic studies, our group observed *CHO species during electrocatalytic CO₂RR,¹⁴² while *OCCOH species was detected during electrocatalytic CORR by Koper and co-workers.²³⁵ These insights provide deeper understanding of the intermediate formation and C–C coupling process. However, it is noteworthy that most of the *in situ* characterization techniques are performed under conditions with low reaction rates, which are different from those adopted for achieving high reaction rates. In the future, characterization techniques should be developed to improve the capability of working under real reaction conditions.

Theoretical calculations have largely contributed to the understanding of active sites and reaction mechanisms for the conversion of C₁ molecules to C₂₊ products as well as the insights that guide the selectivity control. Elementary steps including the activation of C₁ molecules, proton/electron transfer, C₁ intermediate formation, C–C coupling of C₁ intermediates and product formation for different systems have been studied on molecular or atomic levels by using DFT calculations. However, most of the theoretical calculations are based on gas-phase reaction models, whereas the effects of coverage, solution, electrolyte and electric field have seldom been considered, although these effects are known to be very important for photocatalytic and electrocatalytic reactions. Theoretical studies have recently also been exploited to accelerate the catalyst discovery. For example, Sargent and co-workers developed a machine-learning-accelerated, high-throughput DFT framework to screen electrocatalysts.¹⁴⁴ After studying 144 different Cu-containing intermetallic materials, they discovered that a Cu-Al alloy had multiple sites and surface orientations with near-optimal CO binding. The experimentally fabricated de-alloyed nanoporous Cu-Al catalyst showed a FE of C₂H₄ as high as 80%.¹⁴⁴ More efforts should be put in this area in the future.

Photocatalysis and electrocatalysis have been enriching the area of C₁ chemistry. More sustainable routes for the utilisation of C₁ molecules including CO, CO₂, CH₄, CH₃OH and HCHO can be developed to produce C₂₊ compounds such as C₂H₄, C₂H₅OH and EG, which play important roles in the current chemical or energy industry. Not only some existing C₁-chemistry reactions such as the hydrogenation of CO to C₂₊ hydrocarbons could be performed under very mild conditions, offering better selectivity toward target products, but photocatalysis and

electrocatalysis also enable new transformations of C₁ molecules involving C–C coupling, [DOI: 10.1039/D0EE0186K](https://doi.org/10.1039/D0EE0186K) in particular the thermodynamically limited reactions. With the assistance of photo or electrical energy, the inert CO₂ and CH₄ molecules can be efficiently activated to reactive intermediates for subsequent C–C coupling, selectively offering C₂₊ compounds under mild conditions. It is noteworthy that the electrocatalytic conversion of CO₂ to C₂H₄ and C₂H₅OH has achieved significant progress in recent years. Further, the inert C–H bond in CH₃OH could be preferentially activated by photocatalysis with the OH group keeping intact, generating •CH₂OH radical for C–C coupling to EG. Photocatalysis and electrocatalysis have brought many opportunities and also challenges in the area of C₁ chemistry. We are expecting the further breakthroughs in this emerging field.

Conflicts of interest

There are no conflicts to declare.

Acknowledgements

Financial support by the National Key Research and Development Program of Ministry of Science and Technology (2017YFB0602201) and the National Natural Science Foundation of China (Nos. 91945301, 21972115 and 21503176) is greatly acknowledged.

Notes and references

1. C. Mesters, *Annu. Rev. Chem. Biomol. Eng.*, 2016, **7**, 223-238.
2. C. B. Roberts and N. O. Elbashir, *Fuel Processing Technol.*, 2003, **83**, 1-9.
3. Energy Information Administration (EIA), Annual Energy Outlook 2018, (Washington, DC, July 2018) (https://www.eia.gov/pressroom/presentations/capuano_07242018.pdf).
4. W. Keim, *Pure Appl. Chem.*, 1986, **58**, 825-832.
5. W. Cui, G. Zhang, T. Hu and X. Bu, *Coord. Chem. Rev.*, 2019, **387**, 79-120.
6. J. Bao, G. Yang, Y. Yoneyama and N. Tsubaki, *ACS Catal.*, 2019, **9**, 3026-3053.
7. K. Cheng, J. Kang, D. L. King, V. Subramanian, C. Zhou, Q. Zhang and Y. Wang, *Adv. Catal.*, 2017, **60**, 125-208.
8. W. Zhou, K. Cheng, J. Kang, C. Zhou, V. Subramanian, Q. Zhang and Y. Wang, *Chem. Soc. Rev.*, 2019, **48**, 3193-3228.
9. T. Sakakura, J. Choi and H. Yasuda, *Chem. Rev.*, 2007, **107**, 2365-2387.
10. R. W. Dorner, D. R. Hardy, F. W. Williams and H. D. Willauer, *Energy Environ. Sci.*, 2010, **3**, 884-890.
11. W. Wang, S. Wang, X. Ma and J. Gong, *Chem. Soc. Rev.*, 2011, **40**, 3703-3727.
12. M. D. Porosoff, B. Yan and J. G. Chen, *Energy Environ. Sci.*, 2016, **9**, 62-73.
13. H. Yang, C. Zhang, P. Gao, H. Wang, X. Li, L. Zhong, W. Wei and Y. Sun, *Catal. Sci. Technol.*, 2017, **7**, 4580-4598.
14. L. Guo, J. Sun, Q. Ge and N. Tsubaki, *J. Mater. Chem. A*, 2018, **6**, 23244-23262.
15. A. Dokania, A. Ramirez, A. Bavykina and J. Gascon, *ACS Energy Lett.*, 2019, **4**, 167-176.

- 16 J. Zhong, X. Yang, Z. Wu, B. Liang, Y. Huang and T. Zhang, *Chem. Soc. Rev.*, 2020, **49**, 1385-1413.
- 17 X. Jiang, X. Nie, X. Guo, C. Song and J. G. Chen, *Chem. Rev.*, 2020, **120**, 7984-8034.
- 18 M. Ravi, M. Ranocchiari and J. A. van Bokhoven, *Angew. Chem. Int. Ed.*, 2017, **56**, 16464-16483.
- 19 A. I. Olivos-Suarez, Á. Szécsényi, E. J. M. Hensen, J. Ruiz-Martinez, E. A. Pidko and J. Gascon, *ACS Catal.*, 2016, **6**, 2965-2981.
- 20 P. Schwach, X. Pan and X. Bao, *Chem. Rev.*, 2017, **117**, 8497-8520.
- 21 N. J. Gunsalus, A. Koppaka, S. H. Park, S. M. Bischof, B. G. Hashiguchi and R. A. Periana, *Chem. Rev.*, 2017, **117**, 8521-8573.
- 22 U. Olsbye, S. Svelle, M. Bjørgen, P. Beato, T. V. W. Janssens, F. Joensen, S. Bordiga and K. P. Lillerud, *Angew. Chem. Int. Ed.*, 2012, **51**, 5810-5831.
- 23 P. Tian, Y. Wei, M. Ye and Z. Liu, *ACS Catal.*, 2015, **5**, 1922-1938.
- 24 S. Xu, Y. Zhi, J. Han, W. Zhang, X. Wu, T. Sun, Y. Wei and Z. Liu, *Adv. Catal.*, 2017, **61**, 37-122.
- 25 I. Yarulina, A. D. Chowdhury, F. Meirer, B. M. Weckhuysen and J. Gascon, *Nat. Catal.*, 2018, **1**, 398-411.
- 26 M. Yang, D. Fan, Y. Wei, P. Tian and Z. Liu, *Adv. Mater.*, 2019, **31**, 1902181.
- 27 F. Jiao, J. Li, X. Pan, J. Xiao, H. Li, H. Ma, M. Wei, Y. Pan, Z. Zhou, M. Li, S. Miao, J. Li, Y. Zhu, D. Xiao, T. He, J. Yang, F. Qi, Q. Fu and X. Bao, *Science*, 2016, **351**, 1065-1068.
- 28 K. Cheng, B. Gu, X. Liu, J. Kang, Q. Zhang and Y. Wang, *Angew. Chem. Int. Ed.*, 2016, **55**, 4725-4728.
- 29 K. Cheng, W. Zhou, J. Kang, S. He, S. Shi, Q. Zhang, Y. Pan, W. Wen and Y. Wang, *Chem.*, 2017, **3**, 334-347.
- 30 S. Kasipandi and J. W. Bae, *Adv. Mater.*, 2019, **31**, 1803390.
- 31 Z. Li, J. Wang, Y. Qu, H. Liu, C. Tang, S. Miao, Z. Feng, H. An and C. Li, *ACS Catal.*, 2017, **7**, 8544-8548.
- 32 X. Liu, M. Wang, C. Zhou, W. Zhou, K. Cheng, J. Kang, Q. Zhang, W. Deng and Y. Wang, *Chem. Commun.*, 2018, **54**, 140-143.
- 33 P. Gao, S. Dang, S. Li, X. Bu, Z. Liu, M. Qiu, C. Yang, H. Wang, L. Zhong, Y. Han, Q. Liu, W. Wei and Y. Sun, *ACS Catal.*, 2018, **8**, 571-578.
- 34 Y. Ni, Z. Chen, Y. Fu, Y. Liu, W. Zhu and Z. Liu, *Nat. Commun.*, 2018, **9**, 3457.
- 35 Z. Li, Y. Qu, J. Wang, H. Liu, M. Li, S. Miao and C. Li, *Joule*, 2019, **3**, 570-583.
- 36 C. Zhou, J. Shi, W. Zhou, K. Cheng, Q. Zhang, J. Kang and Y. Wang, *ACS Catal.*, 2020, **10**, 302-310.
- 37 W. Zhou, J. Kang, K. Cheng, S. He, J. Shi, C. Zhou, Q. Zhang, J. Chen, L. Peng, M. Chen and Y. Wang, *Angew. Chem. Int. Ed.*, 2018, **57**, 12012-12016.
- 38 J. Kang, S. He, W. Zhou, Z. Shen, Y. Li, M. Chen, Q. Zhang and Y. Wang, *Nat. Commun.*, 2020, **11**, 827.
- 39 G. Chen, G. I.N. Waterhouse, R. Shi, J. Zhao, Z. Li, L. Wu, C. Tung and T. Zhang, *Angew. Chem. Int. Ed.*, 2019, **58**, 17528-17551.
- 40 P. D. Luna, C. Hahn, D. Higgins, S. A. Jaffer, T. F. Jaramillo and E. H. Sargent, *Science*, 2019, **364**, eaav3506.
- 41 Y. Jiang, R. Long and Y. Xiong, *Chem. Sci.*, 2019, **10**, 7310-7326.
- 42 Y. Zhao, G. I. N. Waterhouse, G. Chen, X. Xiong, L. Wu, C. Tung and T. Zhang, *Chem. Soc. Rev.*, 2019, **48**, 1972-2010.
- 43 M. Jouny, G. S. Hutchings and F. Jiao, *Nat. Catal.*, 2019, **2**, 1062-1070.
- 44 G. A. Olah, G. K. Prakash and A. Goepert, *J. Am. Chem. Soc.*, 2011, **133**, 12881-12898.
- 45 S. N. Habisreutinger, L. Schmidt-Mende and J. K. Stolarczyk, *Angew. Chem. Int. Ed.*, 2013, **52**, 7372-7408.
- 46 S. Xie, Q. Zhang, G. Liu and Y. Wang, *Chem. Commun.*, 2016, **52**, 35-59.
- 47 X. Chang, T. Wang and J. Gong, *Energy Environ. Sci.*, 2016, **9**, 2177-2196.
View Article Online
DOI: 10.1039/D0EE01860K
- 48 K. Li, B. Peng and T. Peng, *ACS Catal.*, 2016, **6**, 7485-7527.
- 49 X. Li, J. Yu, M. Jaroniec and X. Chen, *Chem. Rev.*, 2019, **119**, 3962-4179.
- 50 C. F. Shih, T. Zhang, J. Li and C. Bai, *Joule*, 2018, **2**, 1925-1949.
- 51 C. Chen, J. F. K. Kotyk and S. W. Sheehan, *Chem.*, 2018, **4**, 2571-2586.
- 52 L. Zhang, Z. Zhao, T. Wang and J. Gong, *Chem. Soc. Rev.*, 2018, **47**, 5423-5443.
- 53 D. Gao, R. M. Arán-Ais, H. S. Jeon and B. R. Cuenya, *Nat. Catal.*, 2019, **2**, 198-210.
- 54 K. Elouarzaki, V. Kannan, V. Jose, H. S. Sabharwal and J. M. Lee, *Adv. Energy Mater.*, 2019, **9**, 1900090.
- 55 S. Xie, S. Lin, Q. Zhang, Z. Tian and Y. Wang, *J. Energy Chem.*, 2018, **27**, 1629-1636.
- 56 X. Meng, X. Cui, N. P. Rajan, L. Yu, D. Deng and X. Bao, *Chem.*, 2019, **5**, 2296-2325.
- 57 T. Inoue, A. Fujishima, S. Konishi and K. Honda, *Nature*, 1979, **277**, 637-638.
- 58 S. C. Roy, O. K. Varghese, M. Paulose and C. A. Grimes, *ACS Nano*, 2010, **4**, 1259-1278.
- 59 M. R. Hoffmann, J. A. Moss and M. M. Baum, *Dalton Trans.*, 2011, **40**, 5151-5158.
- 60 L. Wei, C. Yu, Q. Zhang, H. Liu and Y. Wang, *J. Mater. Chem. A*, 2018, **6**, 22411-22436.
- 61 F. M. Mota and D. H. Kim, *Chem. Soc. Rev.*, 2019, **48**, 205-259.
- 62 T. Mizuno, K. Adachi, K. Ohta and A. Saji, *J. Photochem. Photobiol. A: Chem.*, 1996, **98**, 87-90.
- 63 J. Mao, T. Peng, X. Zhang, K. Li, L. Ye and L. Zan, *Catal. Sci. Technol.*, 2013, **3**, 1253-1260.
- 64 Y. Liu, B. Huang, Y. Dai, X. Zhang, X. Qin, M. Jiang and M.-H. Whangbo, *Catal. Commun.*, 2009, **11**, 210-213.
- 65 W. Dai, J. Yu, Y. Deng, X. Hu, T. Wang and X. Luo, *Appl. Surf. Sci.*, 2017, **403**, 230-239.
- 66 P. Liou, S. Chen, J. Wu, D. Liu, S. Mackintosh, M. Maroto-Valer and R. Linforth, *Energy Environ. Sci.*, 2011, **4**, 1487-1494.
- 67 H. Park, H. Ou, A. Colussi and M. R. Hoffmann, *J. Phys. Chem. A*, 2015, **119**, 4658-4666.
- 68 O. Ola and M. M. Maroto-Valer, *Appl. Catal. A: Gen.*, 2015, **502**, 114-121.
- 69 M. Cheng, S. Yang, R. Chen, X. Zhu, Q. Liao and Y. Huang, *Int. J. Hydrogen Energy.*, 2017, **42**, 9722-9732.
- 70 C. Wang, R. L. Thompson, P. Ohodnicki, J. Baltrus and C. Matranga, *J. Mater. Chem.*, 2011, **21**, 13452-13457.
- 71 M. A. Asi, C. He, M. Su, D. Xia, L. Lin, H. Deng, Y. Xiong, R. Qiu and X. Li, *Catal. Today*, 2011, **175**, 256-263.
- 72 H. Li, S. Gan, H. Wang, D. Han and L. Niu, *Adv. Mater.*, 2015, **27**, 6906-6913.
- 73 X. Xia, Z. Jia, Y. Yu, Y. Liang, Z. Wang and L. Ma, *Carbon*, 2007, **45**, 717-721.
- 74 L. M. Pastrana-Martínez, A. M. T. Silva, N. N. C. Fonseca, J. R. Vaz, J. L. Figueiredo and J. L. Faria, *Top. Catal.*, 2016, **59**, 1279-1291.
- 75 W. Tu, Y. Zhou, Q. Liu, S. Yan, S. Bao, X. Wang, M. Xiao and Z. Zou, *Adv. Funct. Mater.*, 2013, **23**, 1743-1749.
- 76 S. Sorcar, J. Thompson, Y. Hwang, Y. H. Park, T. Majima, C. A. Grimes, J. R. Durrant and S. In, *Energy Environ. Sci.*, 2018, **11**, 3183-3193.
- 77 L. Yu, G. Li, X. Zhang, X. Ba, G. Shi, Y. Li, P. Wong, J. C. Yu and Y. Yu, *ACS Catal.*, 2016, **6**, 6444-6454.
- 78 T. Yui, A. Kan, C. Saitoh, K. Koike, T. Ibusuki and O. Ishitani, *ACS Appl. Mater. Interfaces*, 2011, **3**, 2594-2600.
- 79 W. Kim, T. Seok and W. Choi, *Energy Environ. Sci.*, 2012, **5**, 6066-6070.
- 80 Y. Zhu, Z. Xu, Q. Lang, W. Jiang, Q. Yin, S. Zhong and S. Bai, *Appl. Catal. B: Environ.*, 2017, **206**, 282-292.

REVIEW

Energy & Environmental Science

- 81 V. Jeyalakshmi, R. Mahalakshmy, K. R. Krishnamurthy and B. Viswanathan, *Catal. Today*, 2016, **266**, 160-167.
- 82 K. Adachi, K. Ohta and T. Mizuno, *Sol. Energy*, 1994, **53**, 187-190.
- 83 O. K. Varghese, M. Paulose, T. J. LaTempa and C. A. Grimes, *Nano Lett.*, 2009, **9**, 731-737.
- 84 X. Zhang, F. Han, B. Shi, S. Farsinezhad, G. P. Dechaine and K. Shankar, *Angew. Chem. Int. Ed.*, 2012, **51**, 12732-12735.
- 85 T. Nguyen and J. C. S. Wu, *Appl. Catal. A: Gen.*, 2008, **335**, 112-120.
- 86 W. Hou, W. Hung, P. Pavaskar, A. Goeppert, M. Aykol and S. B. Cronin, *ACS Catal.*, 2011, **1**, 929-936.
- 87 S. Yu and P. K. Jain, *Nat. Commun.*, 2019, **10**, 2022.
- 88 J. Paul and F. M. Hoffmann, *Catal. Lett.*, 1988, **1**, 445-456.
- 89 C. Lee, R. Antoniou Kourounioti, J. C. S. Wu, E. Murchie, M. Maroto-Valer, O. E. Jensen, C. Huang and A. Ruban, *J. CO₂ Util.*, 2014, **5**, 33-40.
- 90 J. Yang, D. Wang, H. Han and C. Li, *Acc. Chem. Res.*, 2013, **46**, 1900-1909.
- 91 Y. Zhang, B. Xia, J. Ran, K. Davey and S.-Z Qiao, *Adv. Energy Mater.*, 2020, **10**, 1903879.
- 92 S. Xie, Y. Wang, Q. Zhang, W. Deng and Y. Wang, *ACS Catal.*, 2014, **4**, 3644-3653.
- 93 M. Subrahmanyam, S. Kaneko and N. Alonso-Vante, *Appl. Catal. B: Environ.*, 1999, **23**, 169-174.
- 94 M. B. Gawande, A. Goswami, F.-X. Felpin, T. Asefa, X. Huang, R. Silva, X. Zou, R. Zboril and R. S. Varma, *Chem. Rev.*, 2016, **116**, 3722-3811.
- 95 Q. Zhai, S. Xie, W. Fan, Q. Zhang, Y. Wang, W. Deng and Y. Wang, *Angew. Chem. Int. Ed.*, 2013, **52**, 5776-5779.
- 96 S. Sorcar, Y. Hwang, J. Lee, H. Kim, K. M. Grimes, C. A. Grimes, J. Jung, C. Cho, T. Majima, M. R. Hoffmann and S. In, *Energy Environ. Sci.*, 2019, **12**, 2685-2696.
- 97 M. Tahir, *Appl. Catal. B: Environ.*, 2017, **219**, 329-343.
- 98 Q. Kang, T. Wang, P. Li, L. Liu, K. Chang, M. Li and J. Ye, *Angew. Chem. Int. Ed.*, 2015, **54**, 841-845.
- 99 Q. Chen, X. Chen, M. Fang, J. Chen, Y. Li, Z. Xie, Q. Kuang and L. Zheng, *J. Mater. Chem. A*, 2019, **7**, 1334-1340.
- 100 S. Yu, A. J. Wilson, J. Heo and P. K. Jain, *Nano Lett.*, 2018, **18**, 2189-2194.
- 101 M. A. Asi, L. Zhu, C. He, V. K. Sharma, D. Shu, S. Li, J. Yang and Y. Xiong, *Catal. Today*, 2013, **216**, 268-275.
- 102 W. H. Koppenol and J. D. Rush, *J. Phys. Chem.*, 1987, **91**, 4429-4430.
- 103 H.-J. Freund and M. W. Roberts, *Surf. Sci. Rep.*, 1996, **25**, 225-273.
- 104 N.-N. Vu, S. Kaliaguine and T.-O. Do, *Adv. Funct. Mater.*, 2019, **29**, 1901825.
- 105 L. Mino, G. Spoto and A. M. Ferrari, *J. Phys. Chem. C*, 2014, **118**, 25016-25026.
- 106 H. He, P. Zapol and L. A. Curtiss, *Energy Environ. Sci.*, 2012, **5**, 6196-6205.
- 107 B. R. Egginis, P. K. J. Robertson, J. H. Stewart and E. Woods, *J. Chem. Soc., Chem. Commun.*, 1993, 349-350.
- 108 B. R. Egginis, P. K.J. Robertson, E. P. Murphy, E. Woods and J. T.S. Irvine, *J. Photoch. Photobio. A*, 1998, **118**, 31-40.
- 109 I. A. Shkrob, T. W. Marin, H. He and P. Zapol, *J. Phys. Chem. C*, 2012, **116**, 9450-9460.
- 110 Z. Li, J. Liu, Y. Zhao, G. I. N. Waterhouse, G. Chen, R. Shi, X. Zhang, X. Liu, Y. Wei, X.-D. Wen, L.-Z. Wu, C.-H. Tung and T. Zhang, *Adv. Mater.*, 2018, **30**, 1800527.
- 111 Y. Zhao, Z. Li, M. Li, J. Liu, X. Liu, G. I. N. Waterhouse, Y. Wang, J. Zhao, W. Gao, Z. Zhang, R. Long, Q. Zhang, L. Gu, X. Liu, X. Wen, D. Ma, L.-Z. Wu, C.-H. Tung and T. Zhang, *Adv. Mater.*, 2018, **30**, 1803127.
- 112 W. Gao, R. Gao, Y. Zhao, M. Peng, C. Song, M. Li, S. Li, J. Liu, W. Li, Y. Deng, M. Zhang, J. Xie, G. Hu, Z. Zhang, R. Long, X.-D. Wen and D. Ma, *Chem.*, 2018, **4**, 2917-2928.
- 113 X. Guo, Z. Jiao, G. Jin and X. Guo, *ACS Catal.*, 2015, **5**, 3836-3840.
View Article Online
DOI: 10.1039/D0EE01860K
- 114 L. Wang, Y. Zhang, X. Gu, Y. Zhang and H. Su, *Catal. Sci. Technol.*, 2018, **8**, 601-610.
- 115 Y. Zhao, B. Zhao, J. Liu, G. Chen, R. Gao, S. Yao, M. Li, Q. Zhang, L. Gu, J. Xie, X. Wen, L.-Z. Wu, C.-H. Tung, D. Ma and T. Zhang, *Angew. Chem. Int. Ed.*, 2016, **55**, 4215-4219.
- 116 L. Zhang, Z.-J. Zhao and J. Gong, *Angew. Chem. Int. Ed.*, 2017, **56**, 11326-11353.
- 117 L. Fan, C. Xia, F. Yang, J. Wang, H. Wang and Y. Lu, *Sci. Adv.*, 2020, **6**, eaay3111.
- 118 D. U. Nielsen, X.-M. Hu, K. Daasbjerg and T. Skrydstrup, *Nat. Catal.*, 2018, **1**, 244-254.
- 119 D. M. Weekes, D. A. Salvatore, A. Reyes, A. Huang and C. P. Berlinguette, *Acc. Chem. Res.*, 2018, **51**, 910-918.
- 120 D. Higgins, C. Hahn, C. Xiang, T. F. Jaramillo and A. Z. Weber, *ACS Energy Lett.*, 2019, **4**, 317-324.
- 121 T. Burdyny and W. A. Smith, *Energy Environ. Sci.*, 2019, **12**, 1442-1453.
- 122 J. He, K. E. Dettelbach, D. A. Salvatore, T. Li and C. P. Berlinguette, *Angew. Chem. Int. Ed.*, 2017, **56**, 6068-6072.
- 123 W. Ma, S. Xie, X.-G. Zhang, F. Sun, J. Kang, Z. Jiang, Q. Zhang, D.-Y. Wu and Y. Wang, *Nat. Commun.*, 2019, **10**, 892.
- 124 W. Ma, M. Xie, S. Xie, L. Wei, Y. Cai, Q. Zhang and Y. Wang, *J. Energy Chem.*, 2021, **54**, 422-428.
- 125 A. Vasileff, X. Zhi, C. Xu, L. Ge, Y. Jiao, Y. Zheng and S.-Z. Qiao, *ACS Catal.*, 2019, **9**, 9411-9417.
- 126 R. P. Janssonius, L. M. Reid, C. N. Virca and C. P. Berlinguette, *ACS Energy Lett.*, 2019, **4**, 980-986.
- 127 Y. Zheng, A. Vasileff, X. Zhou, Y. Jiao, M. Jaroniec and S.-Z. Qiao, *J. Am. Chem. Soc.*, 2019, **141**, 7646-7659.
- 128 X. Liu, J. Xiao, H. Peng, X. Hong, K. Chan and J. K. Nørskov, *Nat. Commun.*, 2017, **8**, 15438.
- 129 H. Zhang, J. Li, M. Cheng and Q. Lu, *ACS Catal.*, 2019, **9**, 49-65.
- 130 N. S. Romero Cuellar, K. Wiesner-Fleischer, M. Fleischer, A. Rucki and O. Hinrichsen, *Electrochimica Acta*, 2019, **307**, 164-175.
- 131 X. Zhou and C. Xiang, *ACS Energy Lett.*, 2018, **3**, 1892-1897.
- 132 X. Liu, M. Wang, H. Yin, J. Hu, K. Cheng, J. Kang, Q. Zhang and Y. Wang, *ACS Catal.*, 2020, **10**, 8303-8314.
- 133 X. Liu, W. Zhou, Y. Yang, K. Cheng, J. Kang, L. Zhang, G. Zhang, X. Min, Q. Zhang and Y. Wang, *Chem. Sci.*, 2018, **9**, 4708-4718.
- 134 K. Jiang, R. B. Sandberg, A. J. Akey, X. Liu, D. C. Bell, J. K. Nørskov, K. Chan and H. Wang, *Nat. Catal.*, 2018, **1**, 111-119.
- 135 A. Loijudice, P. Lobaccaro, E. A. Kamali, T. Thao, B. H. Huang, J. W. Ager and R. Buonsanti, *Angew. Chem. Int. Ed.*, 2016, **55**, 5789-5792.
- 136 H. Mistry, A. S. Varela, C. S. Bonifacio, I. Zegkinoglou, I. Sinev, Y.-W. Choi, K. Kisslinger, E. A. Stach, J. C. Yang, P. Strasser and B. R. Cuenya, *Nat. Commun.*, 2016, **7**, 12123.
- 137 D. Ren, Y. Deng, A. D. Handoko, C. S. Chen, S. Malkhandi and B. S. Yeo, *ACS Catal.*, 2015, **5**, 2814-2821.
- 138 B. Zhang, J. Zhang, M. Hua, Q. Wan, Z. Su, X. Tan, L. Liu, F. Zhang, G. Chen, D. Tan, X. Cheng, B. Han, L. Zheng and G. Mo, *J. Am. Chem. Soc.*, 2020, **142**, 13606-13613.
- 139 Y. Zhou, F. Che, M. Liu, C. Zou, Z. Liang, P. De Luna, H. Yuan, J. Li, Z. Wang, H. Xie, H. Li, P. Chen, E. Bladt, R. Quintero-Bermudez, T.-K. Sham, S. Bals, J. Hofkens, D. Sinton, G. Chen and E. H. Sargent, *Nat. Chem.*, 2018, **10**, 974-980.
- 140 Z.-Q. Liang, T.-T. Zhuang, A. Seifitokaldani, J. Li, C.-W. Huang, C.-S. Tan, Y. Li, P. De Luna, C. T. Dinh, Y. Hu, Q. Xiao, P.-L. Hsieh, Y. Wang, F. Li, R. Quintero-Bermudez, Y. Zhou, P. Chen, Y. Pang, S.-C. Lo, L.-J. Chen, H. Tan, Z. Xu, S. Zhao, D. Sinton and E. H. Sargent, *Nat. Commun.*, 2018, **9**, 3828.
- 141 D. Gao, I. Sinev, F. Scholten, R. M. Arán-Ais, N. J. Divins, K. Kvashnina, J. Timoshenko and B. R. Cuenya, *Angew. Chem. Int. Ed.*, 2019, **58**, 17047-17053.

- 142 W. Ma, S. Xie, T. Liu, Q. Fan, J. Ye, F. Sun, Z. Jiang, Q. Zhang, J. Cheng and Y. Wang, *Nat. Catal.*, 2020, **3**, 478-487.
- 143 C.-T. Dinh, T. Burdyny, M. G. Kibria, A. Seifitokaldani, C. M. Gabardo, F. P. García de Arquer, A. Kiani, J. P. Edwards, P. De Luna, O. S. Bushuyev, C. Zou, R. Quintero-Bermudez, Y. Pang, D. Sinton and E. H. Sargent, *Science*, 2018, **360**, 783-787.
- 144 M. Zhong, K. Tran, Y. Min, C. Wang, Z. Wang, C. T. Dinh, P. De Luna, Z. Yu, A. S. Rasouli, P. Brodersen, S. Sun, O. Voznyy, C. S. Tan, M. Askerka, F. Che, M. Liu, A. Seifitokaldani, Y. Pang, S. C. Lo, A. Ip, Z. Ulissi and E. H. Sargent, *Nature*, 2020, **581**, 178-183.
- 145 F. P. G. de Arquer, C. T. Dinh, A. Ozden, J. Wicks, C. McCallum, A. R. Kirmani, D. H. Nam, C. Gabardo, A. Seifitokaldani, X. Wang, Y. C. Li, F. Li, J. Edwards, L. J. Richter, S. J. Thorpe, D. Sinton and E. H. Sargent, *Science*, 2020, **367**, 661-666.
- 146 F. Li, A. Thevenon, A. Rosas-Hernández, Z. Wang, Y. Li, C. M. Gabardo, A. Ozden, C. T. Dinh, J. Li, Y. Wang, J. P. Edwards, Y. Xu, C. McCallum, L. Tao, Z.-Q. Liang, M. Luo, X. Wang, H. Li, C. P. O'Brien, C.-S. Tan, D.-H. Nam, R. Quintero-Bermudez, T.-T. Zhuang, Y. C. Li, Z. Han, R. D. Britt, D. Sinton, T. Agapie, J. C. Peters and E. H. Sargent, *Nature*, 2020, **577**, 509-513.
- 147 K. D. Yang, W. R. Ko, J. H. Lee, S. J. Kim, H. Lee, M. H. Lee and K. T. Nam, *Angew. Chem. Int. Ed.*, 2017, **56**, 796-800.
- 148 A. Vasileff, Y. Zhu, X. Zhi, Y. Zhao, L. Ge, H. M. Chen, Y. Zheng and S.-Z. Qiao, *Angew. Chem. Int. Ed.*, 2020, DOI: 10.1002/anie.202004846.
- 149 D. Ren, B. S.-H. Ang and B. S. Yeo, *ACS Catal.*, 2016, **6**, 8239-8247.
- 150 S. Lee, G. Park and J. Lee, *ACS Catal.*, 2017, **7**, 8594-8604.
- 151 T. T. H. Hoang, S. Verma, S. Ma, T. T. Fister, J. Timoshenko, A. I. Frenkel, P. J. A. Kenis and A. A. Gewirth, *J. Am. Chem. Soc.*, 2018, **140**, 5791-5797.
- 152 Y. C. Li, Z. Wang, T. Yuan, D.-H. Nam, M. Luo, J. Wicks, B. Chen, J. Li, F. Li, F. P. G. de Arquer, Y. Wang, C.-T. Dinh, O. Voznyy, D. Sinton and E. H. Sargent, *J. Am. Chem. Soc.*, 2019, **141**, 8584-8591.
- 153 T. T. Zhuang, Z. Q. Liang, A. Seifitokaldani, Y. Li, P. De Luna, T. Burdyny, F. Che, F. Min, R. Quintero-Bermudez, C. T. Dinh, Y. Pang, M. Zhong, B. Zhang, J. Li, P. N. Chen, X. L. Zheng, H. Liang, W. N. Ge, B. LJ. Ye, D. Sinton, S. H. Yu and E. H. Sargent, *Nat. Catal.*, 2018, **1**, 421-428.
- 154 F. Li, Y. C. Li, Z. Wang, J. Li, D.-H. Nam, Y. Lum, M. Luo, X. Wang, A. Ozden, S.-F. Hung, B. Chen, Y. Wang, J. Wicks, Y. Xu, Y. Li, C. M. Gabardo, C.-T. Dinh, Y. Wang, T.-T. Zhuang, D. Sinton and E. H. Sargent, *Nat. Catal.*, 2020, **3**, 75-82.
- 155 Y. Song, R. Peng, D. K. Hensley, P. V. Bonnesen, L. Liang, Z. Wu, H. M. Meyer, M. Chi, C. Ma, B. G. Sumpter and A. J. Rondinone, *ChemistrySelect*, 2016, **1**, 6055-6061.
- 156 X. Wang, Z. Wang, F. P. G. de Arquer, C. T. Dinh, A. Ozden, Y. C. Li, D. H. Nam, J. Li, Y. S. Liu, J. Wicks, Z. Chen, M. Chi, B. Chen, Y. Wang, J. Tam, J. Y. Howe, A. Proppe, P. Todorović, F. Li, T. T. Zhuang, C. M. Gabardo, A. R. Kirmani, C. McCallum, S. F. Hung, Y. Lum, M. Luo, Y. Min, A. Xu, C. P. O'Brien, B. Stephen, B. Sun, A. H. Ip, L. J. Richter, S. O. Kelley, D. Sinton and E. H. Sargent, *Nat. Energy*, 2020, **5**, 478-486.
- 157 C. Chen, X. Yan, S. Liu, Y. Wu, Q. Wan, X. Sun, Q. Zhu, H. Liu, J. Ma, L. Zheng, H. Wu and B. Han, *Angew. Chem. Int. Ed.*, 2020, DOI: 10.1002/anie.202006847.
- 158 H. Xu, D. Rebollar, H. He, L. Chong, Y. Liu, C. Liu, C.-J. Sun, T. Li, J. V. Muntean, R. E. Winans, D.-J. Liu and T. Xu, *Nat. Energy*, 2020, **5**, 623-632.
- 159 Y. Liu, S. Chen, X. Quan and H. Yu, *J. Am. Chem. Soc.*, 2015, **137**, 11631-11636.
- 160 Y. Liu, Y. Zhang, K. Cheng, X. Quan, X. Fan, Y. Su, S. Chen, H. Zhao, Y. Zhang, H. Yu and M. R. Hoffmann, *Angew. Chem. Int. Ed.*, 2017, **56**, 15607-15611.
- 161 Y. Song, S. Wang, W. Chen, S. Li, G. Feng, W. Wei and Y. Sun, *ChemSusChem*, 2020, **13**, 293-297.
- 162 J. Wu, S. Ma, J. Sun, J. I. Gold, C. Tiwary, B. Kim, L. Zhu, N. Chopra, I. N. Odeh, R. Vajtai, A. Z. Yu, [DOI: 10.1039/DCEB00206K](#), P. J. A. Kenis and P. M. Ajayan, *Nat. Commun.*, 2016, **7**, 13869.
- 163 M. Jouny, W. Luc and F. Jiao, *Nat. Catal.*, 2018, **1**, 748-755.
- 164 J. Li, Z. Wang, C. McCallum, Y. Xu, F. Li, Y. Wang, C. M. Gabardo, C.-T. Dinh, T.-T. Zhuang, L. Wang, J. Y. Howe, Y. Ren, E. H. Sargent and D. Sinton, *Nat. Catal.*, 2019, **2**, 1124-1131.
- 165 C. W. Li, J. Ciston and M. W. Kanan, *Nature*, 2014, **508**, 504-507.
- 166 X. Feng, K. Jiang, S. Fan and M. W. Kanan, *ACS Cent. Sci.*, 2016, **2**, 169-174.
- 167 D. Raciti, L. Cao, K. J. T. Livi, P. F. Rottmann, X. Tang, C. Li, Z. Hicks, K. H. Bowen, K. J. Hemker, T. Mueller and C. Wang, *ACS Catal.*, 2017, **7**, 4467-4472.
- 168 J. Li, A. Xu, F. Li, Z. Wang, C. Zou, C. M. Gabardo, Y. Wang, A. Ozden, Y. Xu, D.-H. Nam, Y. Lum, J. Wicks, B. Chen, Z. Wang, J. Chen, Y. Wen, T. Zhuang, M. Luo, X. Du, T.-K. Sham, B. Zhang, E. H. Sargent and D. Sinton, *Nat. Commun.*, 2020, **11**, 3685.
- 169 L. Wang, S. Nitopi, A. B. Wong, J. L. Snider, A. C. Nielander, C. G. Morales-Guio, M. Orazov, D. C. Higgins, C. Hahn and T. F. Jaramillo, *Nat. Catal.*, 2019, **2**, 702-708.
- 170 L. Wang, D. C. Higgins, Y. Ji, C. G. Morales-Guio, K. Chan, C. Hahn and T. F. Jaramillo, *Proc. Natl. Acad. Sci. USA*, 2020, **117**, 12572-12575.
- 171 D. S. Ripatti, T. R. Veltman and M. W. Kanan, *Joule*, 2019, **3**, 240-256.
- 172 W. Luc, X. Fu, J. Shi, J.-J. Lv, M. Jouny, B. H. Ko, Y. Xu, Q. Tu, X. Hu, J. Wu, Q. Yue, Y. Liu, F. Jiao and Y. Kang, *Nat. Catal.*, 2019, **2**, 423-430.
- 173 T. T. Zhuang, Y. Pang, Z.-Q. Liang, Z. Wang, Y. Li, C.-S. Tan, J. Li, C. T. Dinh, P. De Luna, P.-L. Hsieh, T. Burdyny, H.-H. Li, M. Liu, Y. Wang, F. Li, A. Proppe, A. Johnston, D.-H. Nam, Z.-Y. Wu, Y.-R. Zheng, A. H. Ip, H. Tan, L.-J. Chen, S.-H. Yu, S. O. Kelley, D. Sinton and E. H. Sargent, *Nat. Catal.*, 2018, **1**, 946-951.
- 174 Y. Pang, J. Li, Z. Wang, C.-S. Tan, P.-L. Hsieh, T.-T. Zhuang, Z.-Q. Liang, C. Zou, X. Wang, P. De Luna, J. P. Edwards, Y. Xu, F. Li, C.-T. Dinh, M. Zhong, Y. Lou, D. Wu, L.-J. Chen, E. H. Sargent and D. Sinton, *Nat. Catal.*, 2019, **2**, 251-258.
- 175 J. Li, F. Che, Y. Pang, C. Zou, J. Y. Howe, T. Burdyny, J. P. Edwards, Y. Wang, F. Li, Z. Wang, P. De Luna, C.-T. Dinh, T.-T. Zhuang, M. I. Saidaminov, S. Cheng, T. Wu, Y. Z. Finfrock, L. Ma, S.-H. Hsieh, Y.-S. Liu, G. A. Botton, W.-F. Pong, X. Du, J. Guo, T.-K. Sham, E. H. Sargent and D. Sinton, *Nat. Commun.*, 2018, **9**, 4614.
- 176 Y. Hori, I. Takahashi, O. Koga and N. Hoshi, *J. Phys. Chem. B*, 2002, **106**, 15-17.
- 177 Y. Hori, I. Takahashi, O. Koga and N. Hoshi, *J. Mol. Catal. A: Chem.*, 2003, **199**, 39-47.
- 178 K. J. P. Schouten, E. Pérez Gallent and M. T. M. Koper, *ACS Catal.*, 2013, **3**, 1292-1295.
- 179 C. Hahn, T. Hatsukade, Y.-G. Kim, A. Vailionis, J. H. Baricuatro, D. C. Higgins, S. A. Nitopi, M. P. Soria and T. F. Jaramillo, *Proc. Natl. Acad. Sci. USA*, 2017, **114**, 5918-5923.
- 180 Y. Huang, A. D. Handoko, P. Hirunsit and B. S. Yeo, *ACS Catal.*, 2017, **7**, 1749-1756.
- 181 F. S. Roberts, K. P. Kuhl and A. Nilsson, *Angew. Chem. Int. Ed.*, 2015, **54**, 5179-5182.
- 182 H. Xiao, W. A. Goddard III, T. Cheng and Y. Liu, *Proc. Natl. Acad. Sci. USA*, 2017, **114**, 6685-6688.
- 183 M. Favaro, H. Xiao, T. Cheng, W. A. Goddard III, J. Yano and E. J. Crumlin, *Proc. Natl. Acad. Sci. USA*, 2017, **114**, 6706-6711.
- 184 A. Eilert, F. Cavalca, F. S. Roberts, J. Osterwalder, C. Liu, M. Favaro, E. J. Crumlin, H. Ogasawara, D. Friebel, L. G. M. Pettersson and A. Nilsson, *J. Phys. Chem. Lett.*, 2017, **8**, 285-290.

REVIEW

Energy & Environmental Science

- 185 Y. Lum and J. W. Ager, *Angew. Chem. Int. Ed.*, 2018, **57**, 551-554.
- 186 L. Mandal, K. R. Yang, M. R. Motapothula, D. Ren, P. Lobaccaro, A. Patra, M. Sherburne, V. S. Batista, B. S. Yeo, J. W. Ager, J. Martin and T. Venkatesan, *ACS Appl. Mater. Interfaces*, 2018, **10**, 8574-8584.
- 187 C. W. Li and M. W. Kanan, *J. Am. Chem. Soc.*, 2012, **134**, 7231-7234.
- 188 J.-J. Velasco-Vélez, T. Jones, D. Gao, E. Carbonio, R. Arrigo, C.-J. Hsu, Y.-C. Huang, C.-L. Dong, J.-M. Chen, J.-F. Lee, P. Strasser, B. Roldan Cuenya, R. Schlögl, A. Knop-Gericke and C.-H. Chuang, *ACS Sustainable Chem. Eng.*, 2019, **7**, 1485-1492.
- 189 Y. Zhao, X. Chang, A. S. Malkani, X. Yang, L. Thompson, F. Jiao and B. Xu, *J. Am. Chem. Soc.*, 2020, **142**, 9735-9743.
- 190 C. Chen, X. Sun, L. Lu, D. Yang, J. Ma, Q. Zhu, Q. Qian and B. Han, *Green Chem.*, 2018, **20**, 4579-4583.
- 191 T. Shinagawa, G. O. Larrazábal, A. J. Martín, F. Krumeich and J. Pérez-Ramírez, *ACS Catal.*, 2018, **8**, 837-844.
- 192 Y. Huang, Y. Deng, A. D. Handoko, G. K. L. Goh and B. S. Yeo, *ChemSusChem*, 2018, **10**, 1-8.
- 193 R. García-Muelas, F. Dattila, T. Shinagawa, A. J. Martín, J. Pérez-Ramírez and N. López, *J. Phys. Chem. Lett.*, 2018, **9**, 7153-7159.
- 194 D. Gao, F. Scholten and B. R. Cuenya, *ACS Catal.*, 2017, **8**, 5112-5120.
- 195 Y. Huang, C. W. Ong and B. S. Yeo, *ChemSusChem*, 2018, **11**, 3299-3306.
- 196 D. Gao, I. T. McCrum, S. Deo, Y. W. Choi, F. Scholten, W. Wan, J. G. Chen, M. J. Janik and B. R. Cuenya, *ACS Catal.*, 2018, **8**, 10012-10020.
- 197 J. Li, K. Chang, H. Zhang, M. He, W. A. Goddard, J. G. Chen, M.-J. Cheng and Q. Lu, *ACS Catal.*, 2019, **9**, 4709-4718.
- 198 R. Chen, H.-Y. Su, D. Liu, R. Huang, X. Meng, X. Cui, Z.-Q. Tian, D. H. Zhang and D. Deng, *Angew. Chem. Int. Ed.*, 2020, **59**, 154-160.
- 199 S. Ma, M. Sadakiyo, R. Luo, M. Heima, M. Yamauchi and P. J. A. Kenis, *J. Power Sources*, 2016, **301**, 219-228.
- 200 C. M. Gabardo, C. P. O'Brien, J. P. Edwards, C. McCallum, Y. Xu, C.-T. Dinh, J. Li, E. H. Sargent and D. Sinton, *Joule*, 2019, **3**, 2777-2791.
- 201 M. Ma, K. Djanashvili and W. A. Smith, *Angew. Chem. Int. Ed.*, 2016, **55**, 6680-6684.
- 202 L. Wang, S. A. Nitopi, E. Bertheussen, M. Orazov, C. G. Morales-Guio, X. Liu, D. C. Higgins, K. Chan, J. K. Nørskov, C. Hahn and T. F. Jaramillo, *ACS Catal.*, 2018, **8**, 7445-7454.
- 203 J. Li, D. Wu, A. S. Malkani, X. Chang, M. J. Cheng, B. Xu and Q. Lu, *Angew. Chem. Int. Ed.*, 2020, **59**, 4464-4469.
- 204 X. Wang, J. F. de Araújo, W. Ju, A. Bagger, H. Schmies, S. Kühl, J. Rossmeisl and P. Strasser, *Nat. Nanotechnol.*, 2019, **14**, 1063-1070.
- 205 V. Subramani and S. K. Gangwal, *Energy Fuels*, 2008, **22**, 814-839.
- 206 J. Pang, M. Zheng and T. Zhang, *Adv. Catal.*, 2019, **64**, 89-191.
- 207 A. Hira, *Energy Policy*, 2011, **39**, 6925-6935.
- 208 Q. Liu, H. Wang, H. Xin, C. Wang, L. Yan, Y. Wang, Q. Zhang, X. Zhang, Y. Xu, G. W. Huber and L. Ma, *ChemSusChem*, 2019, **12**, 3977-3987.
- 209 H. T. Luk, C. Mondelli, D. C. Ferré, J. A. Stewart and J. Pérez-Ramírez, *Chem. Soc. Rev.*, 2017, **46**, 1358-1426.
- 210 H. Song, P. Wang, S. Li, W. Deng, Y. Li, Q. Zhang and Y. Wang, *Chem. Commun.*, 2019, **55**, 4303-4306.
- 211 M. Yang, H. Qi, F. Liu, Y. Ren, X. Pan, L. Zhang, X. Liu, H. Wang, J. Pang, M. Zheng, A. Wang and T. Zhang, *Joule*, 2019, **3**, 1937-1948.
- 212 C. Li, G. Xu, C. Wang, L. Ma, Y. Qiao, Y. Zhang and Y. Fu, *Green Chem.*, 2019, **21**, 2234-2239.
- 213 F. Calle-Vallejo and M. T. M. Koper, *Angew. Chem. Int. Ed.*, 2013, **52**, 7282-7285. [View Article Online](#) DOI: 10.1039/D0EE01860K
- 214 C. G. Morales-Guio, E. R. Cave, S. A. Nitopi, J. T. Feaster, L. Wang, K. P. Kuhl, A. Jackson, N. C. Johnson, D. N. Abram, T. Hatsukade, C. Hahn and T. F. Jaramillo, *Nat. Catal.*, 2018, **1**, 764-771.
- 215 E. L. Clark, C. Hahn, T. F. Jaramillo and A. T. Bell, *J. Am. Chem. Soc.*, 2017, **139**, 15848-15857.
- 216 R. M. Arán-Ais, F. Scholten, S. Kunze, R. Rizo and B. R. Cuenya, *Nat. Energy*, 2020, **5**, 317-325.
- 217 Gurudayal, D. Perone, S. Malani, Y. Lum, S. Haussener and J. W. Ager, *ACS Appl. Energy Mater.*, 2019, **2**, 4551-4559.
- 218 Y. Jiao, Y. Zheng, P. Chen, M. Jaroniec and S.-Z. Qiao, *J. Am. Chem. Soc.*, 2017, **139**, 18093-18100.
- 219 A. Verdaguer-Casadevall, C. W. Li, T. P. Johansson, S. B. Scott, J. T. McKeown, M. Kumar, I. E. L. Stephen, M. W. Kanan and I. Chorkendorff, *J. Am. Chem. Soc.*, 2015, **137**, 9808-9811.
- 220 D. Kim, C. S. Kley and P. Yang, *Proc. Natl. Acad. Sci. USA*, 2017, **114**, 10560-10565.
- 221 M. Rahaman, A. Dutta, A. Zanetti and P. Broekmann, *ACS Catal.*, 2017, **7**, 7946-7956.
- 222 R. Kortlever, I. Peters, C. Balemans, R. Kas, Y. Kwon, G. Mul and M. T. M. Koper, *Chem. Commun.*, 2016, **52**, 10229-10232.
- 223 F. Studt, I. Sharafutdinov, F. Abild-Pedersen, C. F. Elkjær, J. S. Hummelshøj, S. Dahl, I. Chorkendorff and J. K. Nørskov, *Nat. Chem.*, 2014, **6**, 320-324.
- 224 D. A. Torelli, S. A. Francis, J. C. Crompton, A. Javier, J. R. Thompson, B. S. Brunschwig, M. P. Soriaga and N. S. Lewis, *ACS Catal.*, 2016, **6**, 2100-2104.
- 225 A. R. Paris and A. B. Bocarsly, *ACS Catal.*, 2017, **7**, 6815-6820.
- 226 Y. Song, W. Chen, C. Zhao, S. Li, W. Wei and Y. Sun, *Angew. Chem. Int. Ed.*, 2017, **56**, 10840-10844.
- 227 X. Zhi, Y. Jiao, Y. Zheng and S.-Z. Qiao, *Small*, 2019, **15**, 1804224.
- 228 J. Liu, C. Guo, A. Vasileff and S.-Z. Qiao, *Small Methods*, 2017, **1**, 1600006.
- 229 Y. Liu, X. Fan, A. Nayak, Y. Wang, B. Shan, X. Quan and T. J. Meyer, *Proc. Natl. Acad. Sci. USA*, 2019, **116**, 26353-26358.
- 230 K. Lv, Y. Fan, Y. Zhu, Y. Yuan, J. Wang, Y. Zhu and Q. Zhang, *J. Mater. Chem. A*, 2018, **6**, 5025-5031.
- 231 J. Du, S. Li, S. Liu, Y. Xin, B. Chen, H. Liu and B. Han, *Chem. Sci.*, 2020, **11**, 5098-5104.
- 232 K. J. P. Schouten, Y. Kwon, C. J. M. van der Ham, Z. Qin and M. T. M. Koper, *Chem. Sci.*, 2011, **2**, 1902-1909.
- 233 J. H. Montoya, C. Shi, K. Chan and J. K. Nørskov, *J. Phys. Chem. Lett.*, 2015, **6**, 2032-2037.
- 234 X. Liu, P. Schlexer, J. Xiao, Y. Ji, L. Wang, R. B. Sandberg, M. Tang, K. S. Brown, H. Peng, S. Ringe, C. Hahn, T. F. Jaramillo, J. K. Nørskov and K. Chan, *Nat. Commun.*, 2019, **10**, 32.
- 235 E. Pérez-Gallent, M. C. Figueiredo, F. Calle-Vallejo and M. T. M. Koper, *Angew. Chem. Int. Ed.*, 2017, **56**, 3621-3624.
- 236 J. H. Montoya, A. A. Peterson and J. K. Nørskov, *ChemCatChem*, 2013, **5**, 737-742.
- 237 T. Cheng, H. Xiao and W. A. Goddard III, *Proc. Natl. Acad. Sci. USA*, 2017, **114**, 1795-1800.
- 238 X. Zhi, Y. Jiao, Y. Zheng, A. Vasileff and S.-Z. Qiao, *Nano Energy*, 2020, **71**, 104601.
- 239 A. J. Darza, A. T. Bell and M. Head-Gordon, *ACS Catal.*, 2018, **8**, 1490-1499.
- 240 Y. Y. Birdja, E. Pérez-Gallent, M. C. Figueiredo, A. J. Göttle, F. Calle-Vallejo and M. T. M. Koper, *Nat. Energy*, 2019, **4**, 732-745.
- 241 I. Ledezma-Yanez, E. P. Gallent, M. T. M. Koper and F. Calle-Vallejo, *Catal. Today*, 2016, **262**, 90-94.
- 242 Z. Guo, B. Liu, Q. Zhang, W. Deng, Y. Wang and Y. Yang, *Chem. Soc. Rev.*, 2014, **43**, 3480-3524.
- 243 P. Tang, Q. Zhu, Z. Wu and D. Ma, *Energy Environ. Sci.*, 2014, **7**, 2580-2591.

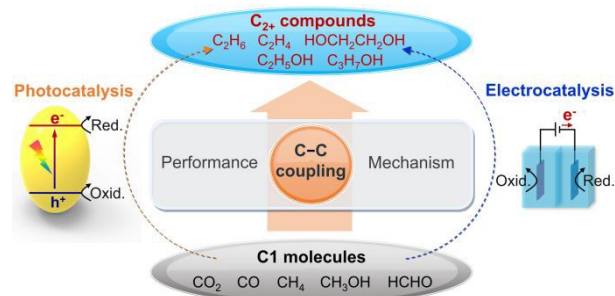
- 244 B. A. Arndtsen, R. G. Bergman, T. A. Mobley and T. H. Peterson, *Acc. Chem. Res.*, 1995, **28**, 154-162.
- 245 H. Song, X. Meng, Z. Wang, H. Liu and J. Ye, *Joule*, 2019, **3**, 1606-1636.
- 246 J. Baltrusaitis, I. Jansen and J. D. Schuttlefield Christus, *Catal. Sci. Technol.*, 2014, **4**, 2397-2411.
- 247 L. Yuliati and H. Yoshida, *Chem. Soc. Rev.*, 2008, **37**, 1592-1602.
- 248 K. Shimura and H. Yoshida, *Catal. Surv. Asia*, 2014, **18**, 24-33.
- 249 Y. Kato, H. Yoshida and T. Hattori, *Chem. Commun.*, 1998, 2389-2390.
- 250 H. Yoshida, N. Matsushita, Y. Kato and T. Hattori, *J. Phys. Chem. B*, 2003, **107**, 8355-8362.
- 251 L. Yuliati, M. Tsubota, A. Satsuma, H. Itoh and H. Yoshida, *J. Catal.*, 2006, **238**, 214-220.
- 252 L. Yuliati, T. Hattori and H. Yoshida, *Phys. Chem. Chem. Phys.*, 2005, **7**, 195-201.
- 253 L. Yuliati, T. Hattori, H. Itoh and H. Yoshida, *J. Catal.*, 2008, **257**, 396-402.
- 254 L. Yuliati, T. Hamajima, T. Hattori and H. Yoshida, *J. Phys. Chem. C*, 2008, **112**, 7223-7232.
- 255 L. Li, G. Li, C. Yan, X. Mu, X. Pan, X. Zou, K. Wang and J. Chen, *Angew. Chem. Int. Ed.*, 2011, **50**, 8299-8303.
- 256 L. Li, Y. Cai, G. Li, X. Mu, K. Wang and J. Chen, *Angew. Chem. Int. Ed.*, 2012, **51**, 4702-4706.
- 257 L. Meng, Z. Chen, Z. Ma, S. He, Y. Hou, H. Li, R. Yuan, X. Huang, X. Wang, X. Wang and J. Long, *Energy Environ. Sci.*, 2018, **11**, 294-298.
- 258 L. Li, S. Fan, X. Mu, Z. Mi and C. Li, *J. Am. Chem. Soc.*, 2014, **136**, 7793-7796.
- 259 X. Yu, V. L. Zholobenko, S. Moldovan, D. Hu, D. Wu, V. V. Ordovsky and A. Y. Khodakov, *Nat. Energy*, 2020, **5**, 511-519.
- 260 S. Murcia-López, K. Villa, T. Andreu and J. R. Morante, *ACS Catal.*, 2014, **4**, 3013-3019.
- 261 F. Sastre, V. Fornés, A. Corma and H. García, *J. Am. Chem. Soc.*, 2011, **133**, 17257-17261.
- 262 S. Murcia-López, M. C. Bacariza, K. Villa, J. M. Lopes, C. Henriques, J. R. Morante and T. Andreu, *ACS Catal.*, 2017, **7**, 2878-2885.
- 263 L. Yu, Y. Shao and D. Li, *Appl. Catal. B: Environ.*, 2017, **204**, 216-223.
- 264 L. Yu and D. Li, *Catal. Sci. Technol.*, 2017, **7**, 635-640.
- 265 Y. Zhou, L. Zhang and W. Wang, *Nat. Commun.*, 2019, **10**, 506.
- 266 F. Amano, C. Akamoto, M. Ishimaru, S. Inagaki and H. Yoshida, *Chem. Commun.*, 2020, **56**, 6348-6351.
- 267 C. E. Taylor and R. P. Noceti, *Catal. Today*, 2000, **55**, 259-267.
- 268 C. E. Taylor, *Catal. Today*, 2003, **84**, 9-15.
- 269 M. A. Gondal, A. Hameed and A. Suwaiyan, *Appl. Catal. A*, 2003, **243**, 165-174.
- 270 M. Stoukides, *J. Appl. Electrochem.*, 1995, **25**, 899-912.
- 271 M. Stoukides, *Res. Chem. Intermed.*, 2006, **32**, 187-204.
- 272 K. Otsuka, S. Yokoyama and A. Morikawa, *Chem. Lett.*, 1985, **14**, 319-322.
- 273 Y. Jiang, I. V. Yentekakis and C. G. Vayenas, *Science*, 1994, **264**, 1563-1566.
- 274 K. Liu, J. Zhao, D. Zhu, F. Meng, F. Kong and Y. Tang, *Catal. Commun.*, 2017, **96**, 23-27.
- 275 A. Caravaca, A. de Lucas-Consuegra, J. González-Cobos, J. L. Valverde and F. Dorado, *Appl. Catal. B: Environ.*, 2012, **113-114**, 192-200.
- 276 A. Caravaca, V. J. Ferreira, A. de Lucas-Consuegra, J. L. Figueiredo, J. L. Faria, J. L. Valverde and F. Dorado, *Int. J. Hydrogen Energy*, 2013, **38**, 3111-3122.
- 277 V. Kyriakou, I. Garagounis and M. Stoukides, *Int. J. Hydrogen Energy*, 2014, **39**, 675-683.
- 278 A. Caravaca, A. de Lucas-Consuegra, V. J. Ferreira, J. L. Figueiredo, J. L. Faria, J. L. Valverde and F. Dorado, *Appl. Catal. B: Environ.*, 2013, **142-143**, 298-306.
- 279 C. Zhu, S. Hou, X. Hu, J. Lu, F. Chen and K. Xie, *Nat. Commun.*, 2019, **10**, 1173. DOI: 10.1039/D0EE01860K
- 280 M. Ma, B. Jin, P. Li, M. Jung, J. Kim, Y. Cho, S. Kim, J. Moon and J. Park, *Adv. Sci.*, 2017, **4**, 1700379.
- 281 M. Ma, C. Oh, J. Kim, J. Moon and J. Park, *Appl. Catal. B: Environ.*, 2019, **259**, 118095.
- 282 Z. Guo, W. Chen, Y. Song, X. Dong, G. Li, W. Wei and Y. Sun, *Chin. J. Catal.*, 2020, **41**, 1067-1072.
- 283 Y. Song, Y. Zhao, G. Nan, W. Chen, Z. Guo, S. Li, Z. Tang, W. Wei and Y. Sun, *Appl. Catal. B: Environ.*, 2020, **270**, 118888.
- 284 N. Lapeña-Rey and P. H. Middleton, *Appl. Catal. A: Gen.*, 2003, **240**, 207-222.
- 285 S. Kodama, R. Kikuchi, N. Fujiwara, S. Tada, Y. Kobayashi and S. T. Oyama, *ECS Trans.*, 2019, **91**, 2697-2705.
- 286 V. Kyriakou, C. Athanasiou, I. Garagounis, A. Skodra and M. Stoukides, *Int. J. Hydrogen Energy*, 2012, **37**, 16636-16641.
- 287 A. de Lucas-Consuegra, N. Gutiérrez-Guerra, A. Caravaca, J. C. Serrano-Ruiz and J. L. Valverde, *Appl. Catal. A: Gen.*, 2014, **483**, 25-30.
- 288 J. Lu, C. Zhu, C. Pan, W. Lin, J. P. Lemmon, F. Chen, C. Li and K. Xie, *Sci. Adv.*, 2018, **4**, eaar5100.
- 289 L. Luo, X. Tang, W. Wang, Y. Wang, S. Sun, F. Qi, W. Huang, *Sci. Rep.*, 2013, **3**, 1625.
- 290 G. A. Olah, *Angew. Chem. Int. Ed.*, 2013, **52**, 104-107.
- 291 S. Yanagida, T. Azuma, H. Kawakami, H. Kizumoto and H. Sakurai, *J. Chem. Soc. Chem. Commun.*, 1984, **1**, 21-22.
- 292 S. Xie, Z. Shen, J. Deng, P. Guo, Q. Zhang, H. Zhang, C. Ma, Z. Jiang, J. Cheng, D. Deng and Y. Wang, *Nat. Commun.*, 2018, **9**, 1181.
- 293 H. Zhang, S. Xie, J. Hu, X. Wu, Q. Zhang, J. Cheng and Y. Wang, *Chem. Commun.*, 2020, **56**, 1776-1779.
- 294 M. Liu, Y. Wang, X. Kong, R. T. Rashid, S. Chu, C. Li, Z. Hearne, H. Guo, Z. Mi and C. Li, *Chem.*, 2019, **5**, 858-867.
- 295 Y. Chao, J. Lai, Y. Yang, P. Zhou, Y. Zhang, Z. Mu, S. Li, J. Zheng, Z. Zhu and Y. Tan, *Catal. Sci. Technol.*, 2018, **8**, 3372-3378.
- 296 Y. Fan, J. Bao, L. Shi, S. Li, Y. Lu, H. Liu, H. Wang, L. Zhong and Y. Sun, *Catal. Lett.*, 2018, **148**, 2274-2282.
- 297 Y. Fan, S. Li, J. Bao, L. Shi, Y. Yang, F. Yu, P. Gao, H. Wang, L. Zhong and Y. Sun, *Green Chem.*, 2018, **20**, 3450-3456.
- 298 J. Bao, Y. Fan, S. Zhang, L. Zhong, M. Wu and Y. Sun, *Catal. Lett.*, 2019, **149**, 1651-1659.
- 299 Y. Li, J. Lu, X. Wang, H. Zhang, X. Wu, K. Zhang, J. Ye and D. Zhan, *ChemCatChem*, 2019, **11**, 2277-2282.
- 300 J. Zhang, Q. Yuan, J. Zhang, T. Li and H. Guo, *Chem. Commun.*, 2013, **49**, 10106-10108.
- 301 J. Zhang, T. Li, D. Wang, J. Zhang and H. Guo, *Chin. J. Catal.*, 2015, **36**, 274-282.
- 302 L. Wang, S. Liu, C. Xu and X. Tu, *Green Chem.*, 2016, **18**, 5658-5666.
- 303 Z. Shen, S. Xie, W. Fan, Q. Zhang, Z. Xie, W. Yang, Y. Wang, J. Lin, X. Wu, H. Wan and Y. Wang, *Catal. Sci. Technol.*, 2016, **6**, 6485-6489.
- 304 S. Xie, Z. Shen, H. Zhang, J. Cheng, Q. Zhang and Y. Wang, *Catal. Sci. Technol.*, 2017, **7**, 923-933.
- 305 M. I. Montenegro, D. Pletcher, E. A. Liolios, D. J. Mazur and C. Zawodzinski, *J. Appl. Electrochem.*, 1990, **20**, 54-59.
- 306 N.L. Weinberg and D.J. Mazur, *J. Appl. Electrochem.*, 1991, **21**, 895-901.
- 307 Y. Ma, X. Wang, Y. Jia, X. Chen, H. Han and C. Li, *Chem. Rev.*, 2014, **114**, 9987-10043.
- 308 H. Lu, J. Zhao, L. Li, L. Gong, J. Zheng, L. Zhang, Z. Wang, J. Zhang and Z. Zhu, *Energy Environ. Sci.*, 2011, **4**, 3384-3388.
- 309 H. Liu, C. Song, L. Zhang, J. Zhang, H. Wang and D. P. Wilkinson, *J. Power Sour.*, 2006, **155**, 95-110.
- 310 J. T. Franclemont, X. Fan, R. Li, R. K. Singh, T. M. Holsen and S. Mededovic Thagard, *Plasma Process Polym.*, 2018, **15**, e1180019.

REVIEW

Energy & Environmental Science

- 311 A. Nawaz, A. Kuila, A. Rani, N. S. Mishra, L. C. Sim, K. H. Leong and P. Saravanan, in *Industrial Applications of Nanomaterials*, eds. S. Thomas, Y. Grohens and Y. B. Pottathara, Elsevier, 2019.
- 312 A. J. Martin, G. O. Larrazabal and J. Perez-Ramirez, *Green Chem.*, 2015, **17**, 5114-5130.
- 313 S.-C. Lin, C.-C. Chang, S.-Y. Chiu, H.-T. Pai, T.-Y. Liao, C.-S. Hsu, W.-H. Chiang, M.-K. Tsai and H. M. Chen, *Nat. Commun.*, 2020, **11**, 3525.

[View Article Online](#)
DOI: 10.1039/D0EE01860K

Table of Contents

Photocatalysis and electrocatalysis have been emerging as important methods for the transformation of abundant C1 molecules into high-value C₂₊ compounds.